Stony Brook University

Thermal Design and Microstructure-Based Property Assessment for Thermal Spray Coating Systems

A Dissertation Presented

by

Yang Tan

to

The Graduate School

in Partial Fulfillment of the

Requirements

for the Degree of

Doctor of Philosophy

in

Mechanical Engineering

(Thermal Sciences and Fluid Mechanics)

Stony Brook University

August 2007

Stony Brook University

The Graduate School

Yang Tan

We, the dissertation committee for the above candidate for the
Doctor of Philosophy degree, hereby recommend acceptance of this dissertation.

Prof. Jon P. Longtin – Dissertation Advisor
Mechanical Engineering

Prof. Hui Zhang – Chairperson of Defense
Mechanical Engineering

Prof. Lili Zheng – Committee Member
Mechanical Engineering

Prof. Andrew Gouldstone – Outside Member
Materials Science and Engineering

This Dissertation is accepted by the Graduate School.

Lawrence Martin
Dean of the Graduate School

Abstract of the Dissertation

Thermal Design and Microstructure-Based Property Assessment for Thermal Spray Coating Systems

by

Yang Tan

Doctor of Philosophy

in

Mechanical Engineering

(Thermal Sciences and Fluid Mechanics)

Stony Brook University

2007

Thermal design and management play critical roles in thermal spray coating systems, and it is important to assess the properties directly from the coating microstructure. In this dissertation, a combined image analysis and finite element method approach is developed to assess thermal conductivity from high-resolution scanning electron microscopy images of the coating microstructure. Images are analyzed with a collection of image processing algorithms to reveal the microscopic coating morphology. The effective thermal conductivity is then simulated using finite element codes in two methods: steady-state and transient. Results are found to be in good agreement with experimental values, obtained using the flash method.

Moreover, experimental issues are addressed for measurement of thermal property of thermal spray coatings. The flash method for thermal diffusivity determination is evaluated for heterogeneous materials. Result shows that for highly heterogeneous materials, there are significant errors for standard flash methods on effective thermal conductivity; however, the errors for thermal spray coatings are negligible. The results are used for validation and correction to the standard flash method.

Finally, based-on the above thermal property assessment techniques, the overall thermal management of thermal spray coating system is investigated, by analyzing the thermal spray coatings annealed in various conditions, and then the long-term thermal performance can be predicted.

Keywords: **thermal conductivity, thermal diffusivity, thermal spray coatings, thermal barrier coatings, image analysis, finite element analysis.**

To my family

Table of Contents

List of Figures

List of Tables

Acknowledgements

I would like to express my deep gratitude to my advisor, Professor Jon P. Longtin, for his continuous support and unending guidance. His knowledge in sciences, expertise in experiments, creativity and innovation, strong writing and communication skills, perseverance and intelligence are always my goal to pursue in my entire research career. It is my great honor to complete this research work under his supervision. It is my pleasure being his student and I wish I would keep learning from him.

I am grateful to Professor Sanjay Sampath, for his continuous support, his understanding, and providing me with the unique opportunity to work in the Center for Thermal Spray Research. His expertise in material science, especially in thermal spray technology, helps me overcome the difficulties during my Ph.D study.

I would like to thank Professor Hui Zhang, Professor Lili Zheng and Professor Andrew Gouldstone for their help. They are nice and knowledgeable people with great research experience which helped me dramatically enhance my dissertation. I appreciate the valuable and insightful discussions with Professor Hui Zhang and Professor Lili Zheng. I appreciate Professor Andrew Gouldstone for his marvelous comments on my research and continuous effort to improve my presentation skills.

I would like to thank Dr. Hsin Wang, Dr. Edgar Lara-Curzio, Dr. Amit Shyam at Oak Ridge National Laboratory, for providing me great opportunities to perform property

measurements by using their facilities, where I got trained through their user programs. The data I obtained from Oak Ridge is extremely important to this dissertation.

I would like to express my gratitude to all my friends and colleagues, for their support in my academic study. They are, but not limited to, Dr. Yuhong Wu, Dr. Jinggao Li, Dr. Martin Friis, Weiguang Chi, Dr, Szymon Tankiewicz, Dr. Xiaolin Wang, Theophilos Theophilou, Dr. Atin Sharma, Dr. Vasudevan Srinivasan, Shan-Shan Liang, Brian Choi, Jae-Hun Kim, Jose Colemenares, Meng Qu, Wei Zhang, Lorena Bejarano, Alfredo Valarezo, Eduardo Mari, Arash Ghabchi, Maricris Silva, Eileen Zappia, Lysa Russo, Rodney Yeung-Vee-Kao, Wenhai Li...

Finally, I would like to thank my family for their forever love. I cannot find any word to express my feeling, but I do appreciate the continuous support from my parents and my wife. I love you all.

Again, thanks to everybody who helped me and who cares me.

Chapter One

Introduction

Thermal spray can produce many different coatings and surfaces with various materials to protect engineering structures from wear, corrosion, erosion, and excessive temperature. Thermal spray coating is produced by a group of continuous melt-spray-solidify process, in which finely divided metallic and nonmetallic particles are molten and accelerated and then are applied by impact onto a prepared substrate to form thin splats and to build up a well-bonded deposit. The heat source can be a combustion flame, a plasma jet, or an arc struck between two consumable wires. The resulting property is microstructure dependent, involving feedstock material and various defects, such as pores, cracks, oxidation, interfaces, grain boundaries, etc. These complex microstructure features are schematically shown in Figure 1-1.

Thermal properties of thermal spray coatings are critical for material selection and parameter determination in processing. In many cases, because of the defected microstructure, the coating thermal properties may be considerably different than the corresponding bulk material. Moreover, the dynamic variation in the complex microstructure during service may result in significant changes in thermal transport

properties, and thus alter the overall thermal behavior of the engineering structures. Therefore, it is important to investigate the thermal transport properties based on the microstructural characterization and to establish the relationship between these two. Ultimately, such studies will provide not only scientific analysis in thermal spray coatings, but enabled new opportunities in design and management of the engineering systems, and process control in coating manufacturing as well.

In this dissertation, first, microstructure-based image analysis technique is developed to investigate the microstructure characteristics of general thermal sprayed coatings, such as porosity, pores and cracks orientation and distribution, oxidation, etc. Second, a combined image analysis and finite element analysis modeling approach is developed to assess thermal conductivity from high-resolution scanning electron microscopy (SEM) images of the coating microstructure. Third, to compare with the modeling data, experimental techniques are introduced to measure the thermal properties of thermal spray coatings at ambient and high temperatures. Then the research work will focus on the thermal barrier coatings (TBCs) to reveal the dynamic changes in thermal conductivity as a function of annealing time and temperature at both ambient and high temperatures. Finally, Based on thermal conductivity data at near-realistic high temperature and thermal gradients that may be encountered in advanced engine systems, the overall thermal behavior of the TBC system can be simulated and predicted.

Image analysis is a powerful tool on microstructure studies for complex engineering components. In this work, coating images are analyzed with a collection of image

processing algorithms to reveal the microscopic coating morphology. The processed digital image is used to generate a two-dimensional finite element meshing in which pores, cracks and the bulk coating material are identified. The thermal transport is then simulated and the effective thermal conductivity is calculated using finite element analysis, in which the digitized image forms the basis for the computational domain.

There has been extensive analytical and numerical work on properties, microstructures and their correlation for two- or three-phase composite porous media to try to understand and predict coating thermal properties. For analytical modeling, a traditional binary mixture thermal conductivity theory called the effective medium theory is firstly introduced by Maxwell. All the current models generally consider two issues namely the volume fraction, i.e. the porosity and the orientation, of pores and cracks. McPherson and Cernuschia developed geometric models to estimate the ratio of the coating and the bulk material thermal conductivity. Sevostianov and Kachanov calculated thermal conductivities of coatings in terms of the relevant microstructural parameters. In this theis, analytical modeling will be developed based on the study of coating micro-structural characteristic and comprehensive coating property measurements. In terms of numerical simulation, the Center of Thermal Spray Research (CTSR) group has previously developed property estimation methods based on both the image-based finite element method for coating images and the use of statistically similar coating models based on small-angle-neutron scattering (SANS). Deshpande and Kulkarni developed image analysis for characterization of porosity and thermal conductivity in thermal spray coatings. Other researchers have also addressed this as

well. Lavigne et al. used image analysis techniques to estimate the porosity of coatings, and subsequently Poulain et al. used an image-based technique and finite-difference approach to estimate thermal conductivity from coating cross-sectional images.

Making accurate model prediction is complicated by the fact that reported experimental values can vary from coating to coating, depending on the deposit technique, heat treatment, and thermal cycling. Even for bulk materials of the same composition, the variance of the property measurement data can be large. In the modeling aspect, this work complements other efforts made by finite element analysis (FEA), small angle neutron scattering (SANS), and image-analysis (IA) approaches. By using several approaches, it is anticipated that the resulting predictions will both improve in accuracy and provide insight into the mechanisms governing transport in thermal spray coatings.

The coating systems studied in this work includes molybdenum, alumina, Ni-5wt%Al, yttria stabilized zirconia (YSZ, ZrO_2-8wt%Y_2O_3), etc. Thermal conductivity modeling and experiments are performed for the above coating systems. Molybdenum coatings fabricated by atmospheric plasma spraying have enhanced resistance to wear and heat. Ni-5wt.%Al coating are use as bond coats because of their superior adhesion. 6-8wt.% yttria content YSZ coatings is still dominant in the application of thermal barrier coatings (TBCs). A 1mm thick YSZ coating can drop the temperature of the superalloy substrate in a gas turbine engine by 100-300^{o}C and greatly increase the thermodynamic efficiency.

YSZ ceramic coatings can be considered as two-phase composite materials, with the two phases being ceramic and air. Bulk YSZ already has a low thermal conductivity ranging from 2-6 $W.m^{-1}.K^{-1}$ depending on grain size and yttria content. It is widely appreciated that the defected microstructure comprising of pores and cracks network contribute substantially to the reduced thermal conductivity of YSZ TBC coatings, which can reach 25% of that of the bulk material. However, after aging at high temperatures, microstructure changes inside the coating cause significant increase in thermal conductivity. The actual thermal conductivity of a coating during service will be a function of starting microstructure, annealing history (time and temperature) and current temperature status. In this work, the annealing effect is studied and the overall thermal behavior of the TBC systems is simulated and predicted.

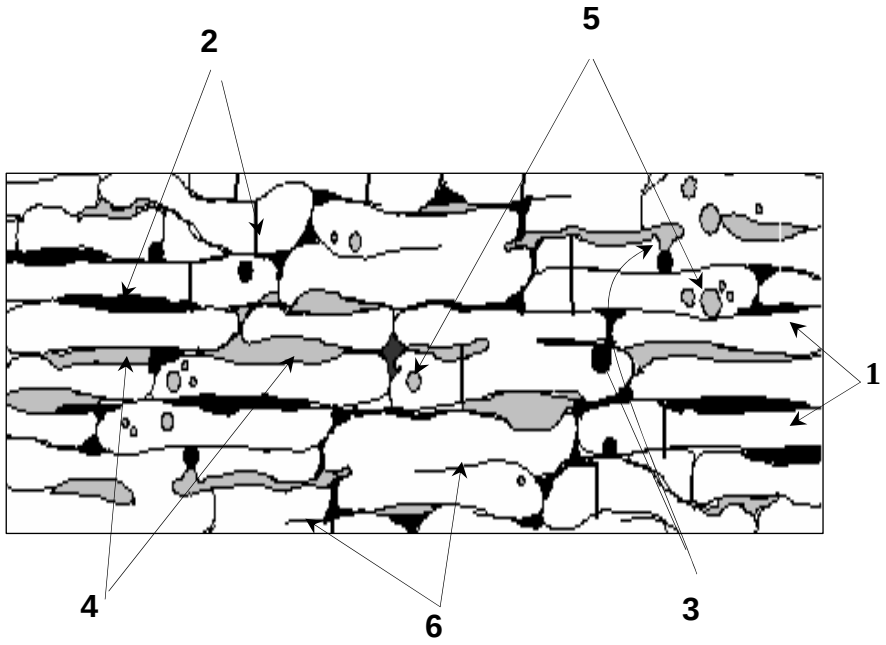

Figure 1-1: Schematic representation of typical microstructure in thermal spray coatings: (1) Splats, (2) cracks, (3) globular pores, (4) Interlayer oxide precipitates, (5) intra-layer oxide precipitates, (6) Interfaces.

Chapter Two

Microstructure Characterization with Image Analysis

The microstructures of thermal spray coatings are very complex due to the complicated thermal spray process. The resulting properties rely critically on the coating microstructure and defects for all constituents, including feedstock material, pores, cracks, oxide, impurities and contaminations. Understanding coating microstructure features allows further investigation on coating properties such as mechanical properties, thermal transport properties and electrical/dielectric behavior. It's important to establish a microstructure -property relationship and to assess coating properties directly from coating microstructure, which strongly depends on the processing parameters.

Various approaches have been employed for qualitative and/or quantitative analysis for microstructure characterization of thermal spray coatings. Small angle neutron scattering (SANS) can obtain statistical results for micro- and nano- size defects less than two microns. Mercury intrusion porosimetry (MIP) evaluates only open porosity due to

its inability to penetrate closed porosity. Direct dimension and weight measurement gives an estimate of total coating porosity but its accuracy strongly depends on the regularity of the machined samples. Image analysis is a straightforward, reliable and inexpensive method, which offers not only porosity, pores and cracks distribution and orientation, but also the interface information and multi-scale investigation.

2.1. Image Analysis Fundamental

Image analysis is the extraction of meaningful information about the structure of an image; mainly from digital images by means of digital image processing techniques. Image analysis tasks can be as simple as reading bar codes or as sophisticated as identifying a person from human face images.

A digital image is composed of pixels which can be thought of as small dots on the screen. Most digital images are usually stored as two-dimensional matrices, in which each element of the matrix represents a single pixel in the corresponding image, where pixel is considered as the element of images. For example, an image with 100 rows and 200 columns of pixels can be stored as a 100 by 200 matrix. Therefore, digital image processing is similar to working with matrix data in many other applications.

2.1.1. Image Types

In the application of this work, two types of images are analyzed, gray-scale images and binary images. A gray-scale image is stored as a single matrix, with each element of the matrix corresponding to one image pixel. Each element in the matrix is an integer in data range [0,255], where 0 is black and 255 represents white, and any other value in between means a gray-scale color. In a binary image, each pixel assumes one of only two discrete values, 0 or 1, which represents black or white, respectively.

2.1.2. Image Histogram

An image histogram is a chart that shows the distribution of intensities in a gray-scale image. An example is made for histogram equalization in figure 2-1. Figure 2-1a is an original gray-scale image, which has low contrast, with most values in the middle of the histogram range (figure 2-1b). Operation is performed on figure 2-1a to produce an improved output image having values evenly distributed throughout the whole range, which is shown in figure 2-1c and the corresponding histogram in figure 2-1d.

2.1.3. Thresholding

Otsu et al. proposed algorithms in 1979 for threshold selection based on image histograms. Let the pixels of a image be in L gray levels $[1,2,\ldots.L]$. The number of pixels at level i is denoted by n_i, and the total number of pixels N will be $N = n_1 + \ldots. + n_i + \ldots. + n_L$ Then suppose that the pixels are separated into two classes C_0 and C_1, which includes pixels with levels $[1,\ldots k]$ and $[k+1,\ldots, L]$, respectively.

This method is based on a discriminant criterion, which is the ratio of between-class variance and total variance of gray levels.

Between-class variance: $$\sigma_B^2 = \omega_0 \omega_1 (\mu_1 - \mu_0)^2 \quad (2\text{-}1)$$

Total variance: $$\sigma_T^2 = \sum_{i=1}^{l} (1 - \mu_1)^2 \, p_i \quad (2\text{-}2)$$

Discriminant criterion: $$\eta = \frac{\sigma_B^2}{\sigma_T^2} \quad (2\text{-}3)$$

where p_i is the probability distribution, $p_i = \frac{n_i}{N}$ (2-4)

ϖ_0 is the probability of class occurrence, $\varpi_0 = \sum_{i=1}^{k} p_i$ (2-5)

ϖ_1 is the probability of class mean levels, $\varpi_1 = 1 - \varpi_0$ (2-6)

μ_0 is the 0th order cumulative moments of the histogram up to the k^{th} level,

$$\mu_0 = \frac{\sum_{i=1}^{k} i p_i}{\varpi_0} \quad (2\text{-}7)$$

μ_1 is the 1st order cumulative moments of the histogram up to the k^{th} level,

$$\mu_1 = \frac{\sum_{i=k+1}^{N} i p_i}{\varpi_0} \quad (2\text{-}8)$$

μ_l is the total mean level of the original image, $\mu_l = \sum_{i=1}^{l} i p_i$ (2-9)

The optimal threshold of an image maximizes the between-class variance, σ_B^2, and leads to the best separation of the resultant classes in gray levels.

Public domain image analysis software from National Institutes of Health (NIH), NIH Image version 1.62, can be used to transform gray scale images to binary (black and white) images, by setting a thresholding criterion based on the grey level mismatch between the YSZ matrix and the void matrix. The thresholding is determined automatically by the software based on the above criterion.

2.1.4. Dilation and Erosion

Dilation and erosion are two fundamental morphological operations. Dilation adds pixels to the boundaries of objects in an image, while erosion removes pixels on object boundaries. The number of pixels added or removed from the objects in an image depends on the size and shape of the structuring element used to process the image.

2.1.5. Binary Image Processing Operators

Binary images can be converted from gray-scale images by various methods including thresholding discussed in the above section. Performing analysis on binary images for coating microstructure allows gathering useful information of detail features. Figure 2-3 shows a few binary image processing operators, (a) removes isolated pixels (individual 1's that are surrounded by 0's), such as the center pixel in this pattern, (b) removes H-connected pixels, (c) bridges previously unconnected pixels, (d) fills isolated interior pixels (individual 0's that are surrounded by 1's), such as the center pixel in this pattern. The operators above are essential for image analysis but only cover a small portion of the morphological operations on binary images

2.1.6. Two-Dimensional Connectivities

The connectivities of the objects are used to separate morphological features, i.e., individual pore or crack and to obtain dimensional information for every single object in the images. Only two-dimensional connectivities are discussed in this chapter, while the three-dimensional connectivities have similar definitions.

4-connected objects (figure 2-4a): Pixels are connected if their edges touch. This means that two adjoining pixels are part of the same object only if they are both on and are connected along the horizontal or vertical direction. 8-connected Object (figure 2-4b): Pixels are connected if their edges or corners touch. This means that if two adjoining pixels are connected and are part of the same object, once they are connected along either the horizontal, vertical, or diagonal direction.

2.1.7. Image Features

Every single image object can be evaluated based on the measurements for image regions. The information includes: (1) Area (Volume), the actual number of pixels in the region, (2) Major Axis Length, (3) Minor Axis Length, (4) Orientation, (5) The enter of mass of the region, (6) Smallest rectangle that can contain the region, etc.

2.2 Collection of Coating Images

Thermal spray coatings are cut and polished on the cross-section or in-plane surface, according to the standard polishing procedures by Buehler, a leading company provides grinders and polishers. Scanning Electron Microscopy (SEM) is used in this work since it provides high-resolution microstructure images compared with optical microscopy

2.2.1. Scanning Electron Microscopy (SEM)

An LEO 1550 SFEG SEM instrument is used for imaging at magnifications between 1000× and 10000× in this work. The raw and uncompressed images from the SEM are collected using the backscattering detector (RBSD) are 8-bit gray-scaled in TIFF format. The resolution of the SEM image is either 1024×768 or 3072×2304 pixels, which is the same to the resolution of one of the two detectors in the SEM instrument.

2.2.2. SEM Hot Stage

High-temperature image processing is also performed in this work. The SEM has a hot stage integrated into the viewing chamber that allows the sample temperature to be adjusted from room temperature to 1200^{o}C. The same location on a sample can thus be imaged at a variety of temperatures to assess how the coating microstructure changes with temperature. Moreover, the distinction between reversible vs. irreversible, i.e., permanent, change in the coating structure when the coating exposed to high temperature can be ascertained with this approach.

2.3. Image Analysis for Thermal Spray Coatings

As an example, figure 2-1a shows an SEM image of a YSZ coating that is 170×108 microns in actual size. The top and bottom of the image correspond to the top (exposed) and bottom (substrate) region of the coating, respectively. The coating microstructure images were converted from 0-255 gray scale to a 0-1 binary scaling by image analysis program, through which, the detailed topology information was recorded for every pore and interlaminar crack inside the coating. The binary image of figure 2-1a is shown in figure 2-1b. The black pixels in figure 2-1b represent voids and white pixels ceramic. In figure 2-1c and figure 2-1d, individual pores and cracks are identified based on their aspect ratio. Each shape is considered to be a spherical element with aspect ratios of h/w, where w and h are the major and minor axes, respectively. The object is taken to be a globular pore if its aspect ratio is greater than or equal to a constant (in figure 2-1, the constant is 1/6), and is taken as a crack if its aspect ratio is less than this constant. Change to the constant can vary the separated images shown in figure 2-2c and figure 2-2d. This separation technique, which was originally developed by Friis, is not required for thermal conductivity modeling in this work. However, it allows insights into the coating microstructure. Moreover, each single crack is analyzed and classified as horizontal or vertical with respect to the angle between the cracks and the horizontal boundary of the image, with a thresholding angle 45^{o}. Images of the horizontal and vertical cracks are shown in figure 2-1e and figure 2-1f, respectively.

2.4. Threshold Variability

In order to investigate the threshold variability, a group of 60 gray-scale SEM images of YSZ coatings are analyzed by the NIH software. These images are taken by the same SEM instrument but are at varying magnifications from 1000× to 10000×. The standard deviation of the threshold values of the 60 images is 5%.

2.5. Concluding Remarks

In image analysis and microstructure modeling, images large enough in size must be used to provide detailed microstructure characterization, as well as global information. Images that are too detailed will result in loss of global coating information. It is important to strike a balance between local and global information, and use the appropriate image size and computational capability.

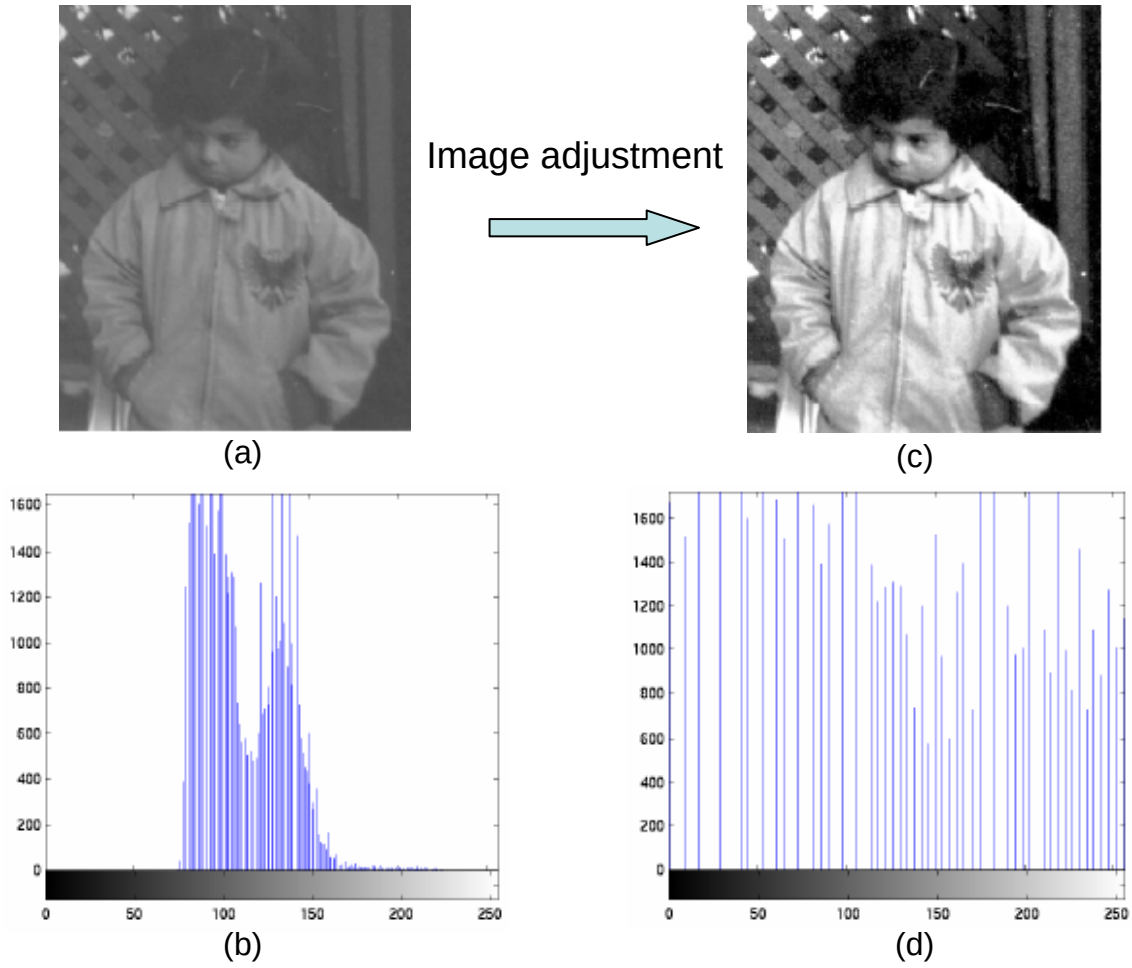

Figure 2-1. Histogram equalization: (a) Original gray-scale image, (b) Histogram of the original image, (c) Adjusted image, (d) Histogram of the adjusted image.

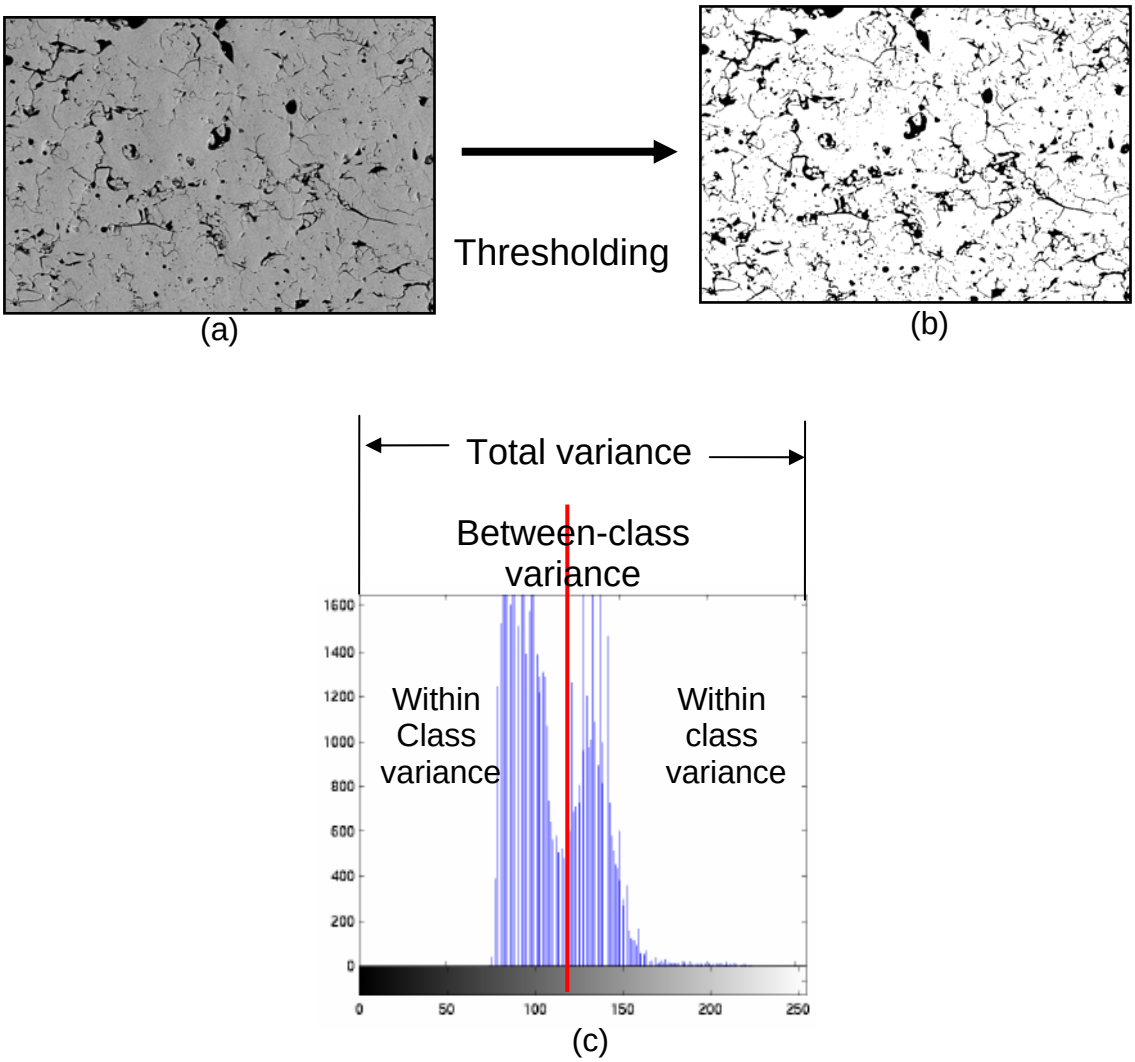

Figure 2-2. Thresholding: (a) Original gray-scale image, (b) Binary image (c) Histogram of the gray-scale image.

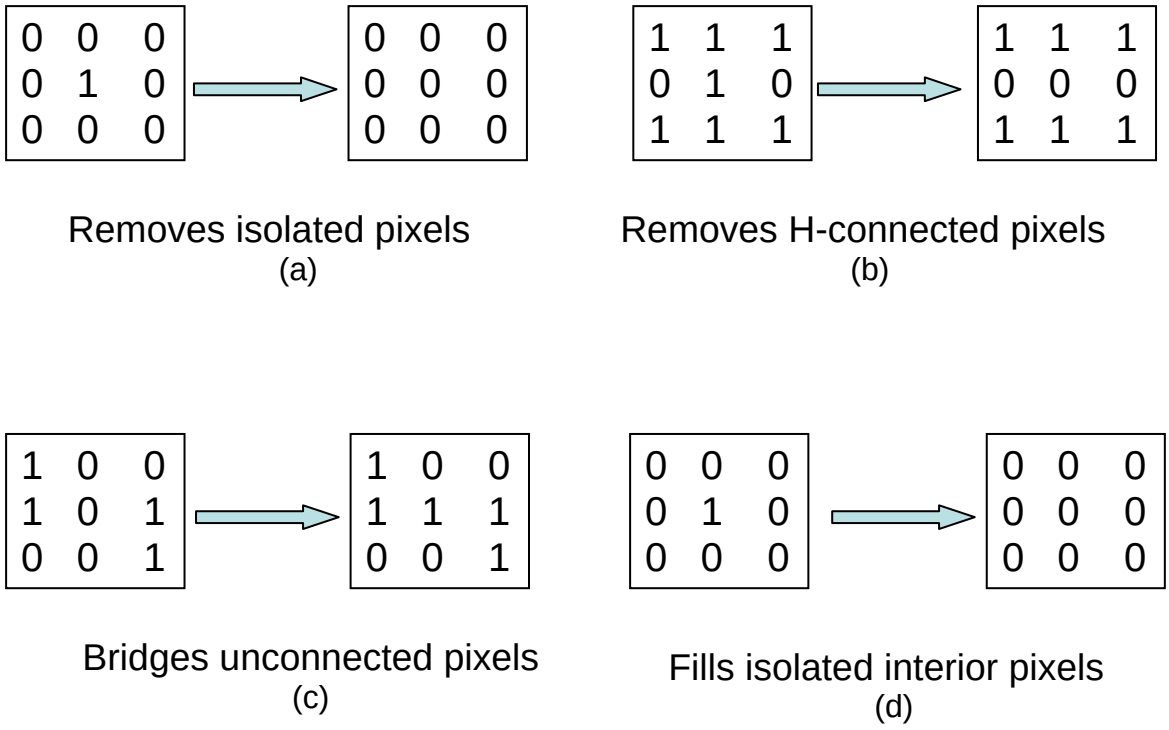

Figure 2-3. Fundamental image processing operators (a) Removes isolated pixels, (b) Removes H-connected pixels, (c) Bridges unconnected pixels, (d) Fills isolated interior pixels.

0	0	0	0	0	0	0	0
0	1	1	0	0	3	3	3
0	1	1	0	0	0	3	3
0	1	1	0	0	0	0	0
0	0	0	2	2	0	0	0
0	0	0	2	2	0	0	0
0	0	0	2	2	0	0	0
0	0	0	0	0	0	0	0

4-connected Objects
(a)

0	0	0	0	0	0	0	0
0	1	1	0	0	1	1	1
0	1	1	0	0	0	1	1
0	1	1	0	0	0	0	0
0	0	0	1	1	0	0	0
0	0	0	1	1	0	0	0
0	0	0	1	1	0	0	0
0	0	0	0	0	0	0	0

8-connected Objects
(b)

Figure 2-4. Two-dimensional pixel connectivities (a) 4-connected Objects, (b) 8-connected Objects.

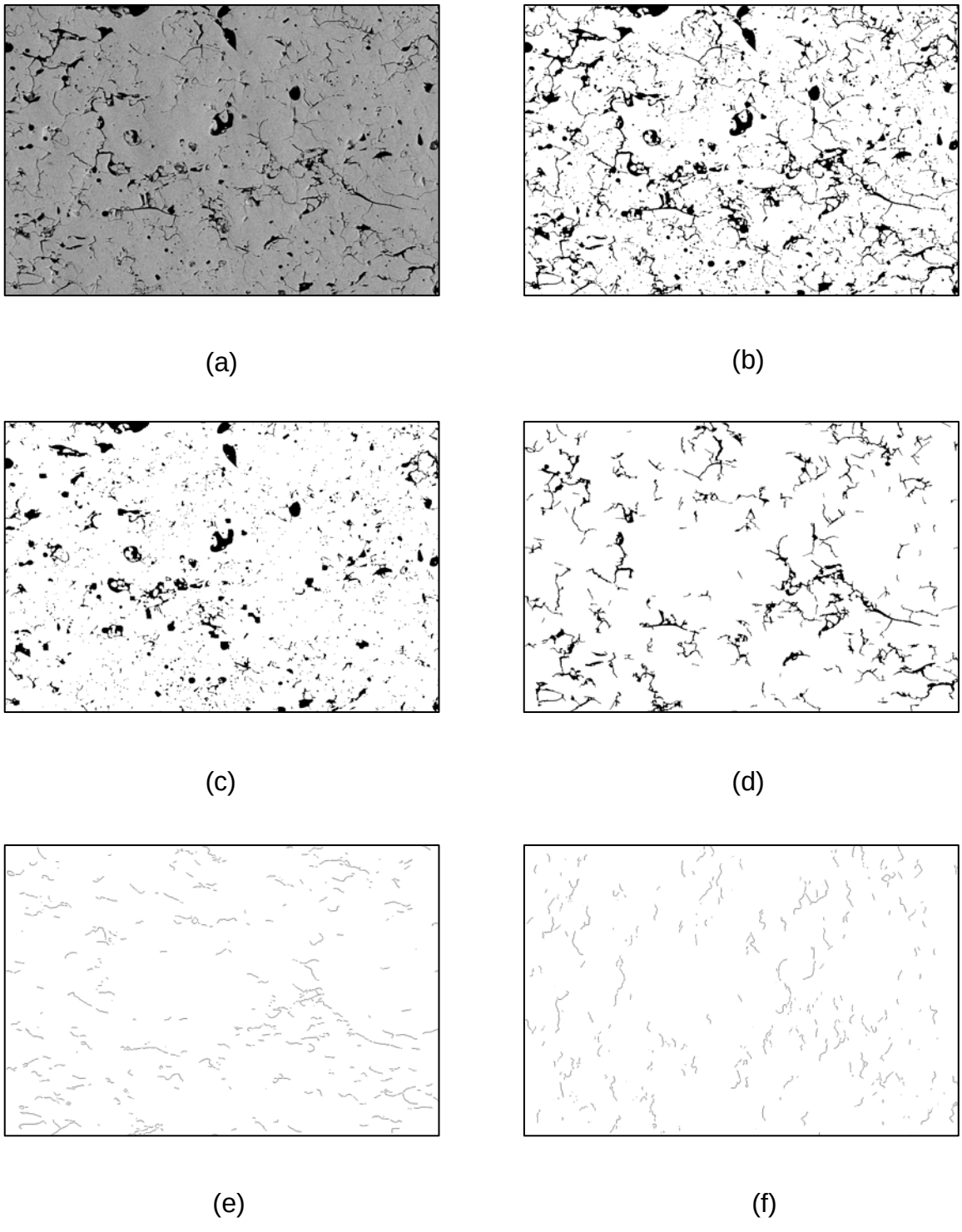

Figure 2-5. Image analysis for thermal spray coatings: (a) An original gray-scale SEM image for Zirconia-based ceramic Coating, (b) Binary or B/W image, (c) Globular pore image, (d) crack image, (e) horizontal crack image (f) vertical crack image.

Chapter Three

Microstructure-Based Thermal Property Modeling

Thermal transport property, which plays a critical role in thermal transport, is a key parameter for thermal spray coatings. The above attributes depend strongly upon geometrical features in the coating microstructure, and are thus sensitive to process parameters. A quantitative understanding of properties and the contribution from different defects has become critical in the development of coating models for design and optimization of the process, performance estimation of thermal spray coatings.

Obtaining experimental data, especially thermal conductivity, is time consuming, and requires specific specimen geometries and expensive equipment. In this dissertation, the applicability of microstructure-based modeling is examined to extract thermal conductivity from cross-sectional micrographs of the coating microstructure. This allows investigation of how microstructure and defect morphologies affect coating thermal transport. Similar approaches have been conducted in the past for select coating systems.

However, for this technique to be widely acceptable it needs to be demonstrated on large number of material systems and process conditions, and to be validated with respect to experimental data. Towards this end is the objective of this study.

In this work, high-resolution Scanning Electron Microscopy (SEM) images are used as the basis for a finite-element model (FEM) to predict thermal conductivity. Each pixel in the image becomes a single volume element in the FEM mesh. The basic concepts of thermal conductivity modeling using this approach will be described afterwards, which complemented other modeling efforts made by Wang et al., Deshpande et al., Kulkarni et al., Lavigne et al. and Poulain et al. By changing the boundary conditions in the model, thermal conductivity can be simulated in both the direction perpendicular to the film (though-thickness direction) and in the plane of the film (in-plane direction).

High-temperature (up to 1200^{o}C) in-situ image processing is also performed in this work, with the hot stage SEM components. The same location on a sample can thus be imaged at a variety of temperatures to assess how the coating microstructure changes with temperature. It is anticipated that the changes in the same location of microstructure during heat treatment will both improve accuracy and provide further insight into the mechanisms governing thermal transport in thermal spray coatings.

3.1. Microstructure-Based Finite Element Property Modeling

In microstructure-based property modeling, images large enough in size must be used to provide detailed microstructure characterization, as well as global information. Images that are too detailed will result in loss of global coating information. It is important to strike a balance between local and global information, and use the appropriate image size and computational capability.

In Chapter two, the detail process was previously described to generate binary images from original gray-scale images. The image analysis results are used here directly to generate the material property matrices in a finite element simulation. Thermal conductivity modeling results are provided for both through-thickness and in-plane directions for a single image.

The image in figure 2-5b is a binary image for a YSZ coating with $m \times n$ pixels (m rows and n columns), where black represents void and white represents the coating, e.g., YSZ in this image. This image, which is stored as a matrix shown in figure 3-1a, can be used directly as the calculation mesh for a Finite Element Analysis (FEA). The resulting image produces a mesh with m rows and n columns, with 0 representing a void and a 1 representing the coating material, e.g., YSZ. Engineering software *Ansys* (version 10.0) is used for all finite element analysis.

The FEA is performed according to the following algorithm:

1. Create a rectangular area with length and width ratio *m:n*.

2. Define two materials: ceramic and air (inside voids), with appropriate thermal conductivities (2.5 $W.m^{-1}.k^{-1}$ and 0.026 $W.m^{-1}.k^{-1}$, respectively, for the YSZ case).

3. Mesh the area with m×n elements, where $m \times n$ is the original height and width of the image.

4. Assign material properties to each element, according to the image-based material matrix.

5. Apply boundary conditions: for through-thickness thermal conductivity these are isothermal upper and lower boundaries and adiabatic left and right boundaries; for the in-plane direction the boundary conditions are rotated 90^o. The difference between the two isotherms will influence the heat flux but not influence the thermal conductivity result. Hence the isotherms can be set to be any two distinct values around interested temperature, for example, 25^oC and 15^oC for modeling at ambient temperature.

6. Calculate the vertical heat flux of each element for through-thickness thermal conductivity modeling, or horizontal heat flux for the in-plane direction. The heat flux of each element is proportional to the isotherm difference.

7. Calculate the effective through-thickness thermal conductivity calculated by averaging the heat flux of each element.

Figure 3-2a is an original gray-scale image (1024×768 total pixels) of a YSZ coating cross-section. To simulate through-thickness thermal conductivity, the boundary conditions are taken as isothermal for the upper and lower boundaries and insulated

(adiabatic) for the left and right side boundaries. For steady-state conditions, the heat flow through any horizontal plane (actually a horizontal line in the 2-D image) will be the same and equal to the total heat flow due to energy conservation. As a consequence the heat flux through the pores and cracks is low because of the low air thermal conductivity (0.026 W/m.K), while the heat flux in the YSZ adjacent to the pores and cracks increases. This can be observed by comparing the topology image in figure 3-2a and the vertical heat flux contour plot in figure 3-2b.

By changing the isotherms for the upper and lower boundaries, the heat flow, heat flux and spatially resolved thermal conductivity can be determined. In figure 3-2b, blue and red represent the lowest and highest heat fluxes, respectively. From the figure, it is seen that the pores and cracks are important for thermal resistance: the heat flux is reduced where the pores and cracks appear. In addition, in the regions immediately above and below a pore or crack the heat flux is reduced; however, along the side areas of the same pore or crack, the heat flux is enhanced.

3.2. Transient Microstructure-Based Finite Element Property Modeling

In the transient microstructure-based finite element property modeling, the analysis domain is the same with the steady-state case, which is based on the microstructure images and direct meshing.

According to the work of Carslaw and Jaeger, the temperature distribution in a thermally insulated specimen with thickness *l* is:

$$T(x,t)=\frac{1}{l}\int_0^l T(x,0)dx+\frac{2}{l}\sum_{n=1}^{\infty}\exp\left(\frac{-n^2\pi^2\alpha t}{l^2}\right)\cos\left(\frac{n\pi x}{l}\right)\int_0^l T(x,0)\cos\frac{n\pi x}{l}dx \qquad (3\text{-}1)$$

where α is thermal diffusivity. Based-on Park et al., when the heat pulse Q is instantaneously and homogeneously absorbed at a small depth h, from the front specimen surface (x = 0), the temperature distribution in any specific time

$$T(x,0)=Q/\rho C_p, \qquad 0<x<h \qquad (3\text{-}2)$$

$$T(x,0)=0, \qquad 0<x<h \qquad (3\text{-}3)$$

Where ρ and C_p are the density and the specific heat of the material, respectively. So Eq. (3-1) can be rewitten as

$$T(x,t)=\frac{Q}{\rho C_p l}\cdot\left[1+2\sum_{n=1}^{\infty}(-1)^n\cos\left(\frac{n\pi x}{l}\right)\frac{\sin\left(n\pi g/l\right)}{n\pi g/l}\exp\left(\frac{-n^2\pi^2\alpha t}{l^2}\right)\right] \qquad (3\text{-}4)$$

the specimen rear surface temperature distribution can be expressed as:

$$T(l,t)=\frac{Q}{\rho c_p l}\left[1+2\sum_{n=1}^{\infty}(-1)^n\exp(\frac{-n^2\pi^2\alpha t}{l^2})\right] \qquad (3\text{-}5)$$

Therefore, the thermal diffusivity of a specific region can be simulated according to the above rear surface temperature distribution, given the initial heat pulse absorbed by the front surface.

The difference between steady-state and transient-state simulation is: (a) the boundary condition, a short time uniform thermal pulse (typically the pulse duration time is less than 1 milisecond) is applied to one of the two horizontal surfaces of a microimage. The energy of the pulse is absorbed on the front surface of a specimen and the resulting rear face temperature rise is calculated. (b) the analysis type is transient instead of steady-state and requires time-step much less than the heat flux duration. Thermal diffusivity values are then calculated given the specimen thickness. This transient method is used to compare with the steady-state method, and is has important application for measurement of thermal diffusivity. This method will be discussed later to validate and correct the flash method.

3.3. Modeling Result Variation

3.3.1. Effect of Threshold Level

In image analysis, different thresholding selection for images will cause different thermal conductivity modeling result. The sensitivity of thermal conductivity on thresholding is investigated by artificially changing the threshold level for binary image conversion. The change of 20 units in the threshold level, which makes a significant difference in a 0-255 scale, gives 5% difference in the FEA thermal conductivity results. This means that the image-based FEA modeling technique is not sensitive to slight change on the threshold level.

3.3.2. Dependence on Coating Location

It is also interesting to note that images taken from different regions of the same coating yield similar porosity and thermal conductivity predictions. This makes it possible to model and predict coating thermal conductivity by averaging results from only a few images taken from distinct locations in the coating. To illustrate this, ten distinct images were taken from different locations in the same YSZ coating. Calculation of porosity and thermal conductivity results in an average porosity of 7.6 percent with a standard deviation of 10% and an average thermal conductivity of 1.9 W/m.K with a standard deviation of 5%. The results are shown in figure 3-3.

3.3.3. Dependence on Image Magnification and Image Size

In image analysis and microstructure modeling, the magnification (or equivalently the size of the coating that is imaged) used can have a significant impact on the resulting analysis. Images that are highly magnified result in a loss of global coating information, while images with too low of a magnification cannot accurately capture the detailed microstructure at small scales. It is thus important to strike a balance between local and global information, and use the appropriate magnification, while also considering computational requirements.

In this work, the effects of magnification and size are investigated in two ways. First, images are taken at the same site of a coating, but at different magnification levels. It is found that higher magnifications result in larger predicted thermal conductivity values. For example, average thermal conductivity results for 10000× images were 5% larger

than those of 1000× images of the same coating location. This indicates that images taken in high magnifications lose global information, for example, large pores, and thus tend to increase the thermal conductivity results. In the second approach, a single image at a given magnification is divided into nine smaller equal-sized images and the finite element model is applied to each sub-image independently. Using this approach, a standard deviation of 5% of the average values was found across the subimages. Interestingly, the average value of the nine thermal conductivity results is very close to the thermal conductivity modeling result for the large image. This suggests that the largest images possible (highest number of pixels), within the limits of the imaging system should be used. In this work, the uncertainty of the predicted values is estimated to be the combination of the image and location uncertainties, i.e., 10% for all measurements.

3.4. Result and Discussion at Ambient Temperature

Various thermal spray coatings, including yttria stabilized zirconia (YSZ), molybdenum, Ni-5wt.%Al are explored in this work. For each material, thermal conductivity is simulated by using the microstructure image-based finite element analysis model. The coating thermal conductivity is also experimentally measured by using a high-temperature laser flash technique, and is compared with modeling results. The detail of the experimental issues will be address in the following Chapter.

3.4.1. YSZ Coatings

YSZ coatings are often exposed to very high temperature and/or multiple thermal cycles for long periods (1000s of hours) when used as thermal barrier coatings for engineering systems, e.g., in turbine engines. The thermal behavior after heat treatment or annealing is thus important and must be considered for its effect on long-term coating properties. Thermal conductivity modeling and measurement are performed for three types of YSZ coatings both before and after annealing made from *fused and crushed* (F&C), *agglomerated and Sintered* (A&S) and *plasma densified hollow spheres* (HOSP) powders. The annealing heat treatment is the same for all coatings: 225 hours at 1200^{o}C, after which the coating is slowly cooled to room temperature to avoid additional fracture. Figure 3-4 shows microstructure images of the three types of YSZ coatings before and after annealing (Note that the before and after images represent different locations on the coating). For the as-deposited coatings, the pore and crack network in the cross-section images is clear and continuous, while the pores and cracks in the annealed coating images are discontinuous and appear to be closing. This geometry change can alter the thermal conductivity of the coatings. The model and measurement data for YSZ coating thermal conductivity before and after annealing are shown in Table 3-1 and figure 3-5.

It can be seen that after long-term annealing the thermal conductivity data increased for both finite element and measurement results. As mentioned before, this is because of the microstructure changes, boundary vanishing, etc. Previous work has indicated that the porosity will also decrease after long-term annealing.

As can be seen in the preceding results, a deviation can be found between the modeling and the experimental data. This may be due to a variety of factors including: (a) Inadequate resolution in the SEM images, which is unable to accurately capture all of the fine cracks and interfaces, especially in the nano-scale, which are thermal barrier to the heat flow and will lower the computed thermal conductivity. (b) 2-Dimensional effect since strictly speaking, thermal conductivity is a three-dimensional property and relies on three-dimensional microstructure network. The two-dimensional microstructure image, which is an approximation of the actual three-dimension structure of a thermal sprayed coating, may lead to significant errors. (c) Other thermal mechanisms, such as radiation and phonon and photon scattering, which are not included in the simple model. (d) For the bulk thermal conductivity determination, the bulk value in this work is chosen as 2.5W/m.K, which is the same as in literature. However, this result may have a deviation from the true value. A more accurate bulk value, which can be obtained by long-term annealing, will help to decrease the deviation between the simulation and experiment.

3.4.2. Molybdenum Coatings

Figure 3-6 shows the original gray-scaled and the black and white images where the white area is molybdenum and black is air (only a small amount of oxidation). The thermal conductivity of pure molybdenum is very high (142 $W.m^{-1}.k^{-1}$), compared to the thermal conductivity of air. The results of the model and experimental values of thermal conductivity are listed in Table 3-2. It can be seen that the modeling results capture the same trend in the experiments for the thermal conductivities in two perpendicular directions (through-thickness and in-plane).

3.4.3. NiAl Coatings

Figure 3-7 shows the original SEM images for Ni-5wt.%Al coating for three processing techniques: air plasma spraying (APS), twin wire-arc spraying (TWA) and high velocity oxy-fuel spraying (HVOF). Similar to the previous studies, the modeling procedure takes the light regions to be bulk Ni-Al. However, Ni-5wt.%Al is easily oxidized, hence the black areas can actually be the combination of the oxides and pores/cracks. The oxidation part mainly comes from the Al element. Therefore, the black area will mainly be the combination of alumina and porosity. Over estimation of the pores/cracks in the microstructure will cause potential problem and need to be improved.

Another important contribution is from the intrinsic thermal property of NiAl alloy. For the APS and TWA cases, there are more oxides than that in HVOF spraying. An elemental distribution of nickel, aluminum and oxygen in an APS coating shows that the core of the splats (grey region in figure 3-7) is pre-dominantly nickel. The aluminum, because of its tendency to oxidize, is concentrated towards the outer surface of the splats (black region in figure 3-7) along with the oxygen. While the oxides will be concentrated in the black area as stated before, the bulk material in the coating will not be 5% alloy any more, and the percentage of aluminum will be dramatically reduced. As a fact, the thermal conductivity of the bulk Ni-Al alloy with less Al percentage, for example, thermal conductivity of Ni-0.5wt.%Al, is much higher than that of the bulk Ni-5wt.%Al material. This causes the opposite trend comparing modeling to experiments in the thermal conductivity results in figure 3-8 for NiAl coatings. In this work, different

thermal conductivity for bulk Ni-Al materials is selected for HOVF (40 W/m•k) and APS or TWA cases (80 W/m•k).

3.4.4. Alumina Coatings

Figure 3-9 shows the original gray-scaled and the processed black and white images for alumina coatings made by air plasma spraying (APS) and high velocity oxy-fuel spraying (HVOF), respectively. The modeling results for porosity and thermal conductivity are shown in figure 3-10 and figure 3-11.

3.5. Result and Discussion at High Temperature

The model is then applied to high temperature conditions (up to 1200^{o}C) with a hot stage equipped scanning electron microscope imaging technique to assess thermal conductivity at high temperatures.

The coating microstructure images can be taken under high temperature up to 1200^{o}C by using a Fullam 18020 hot stage accessory for the SEM. This provides the ability to take images from the same location in a coating cross-section as the temperature is changed from room temperature to high temperature (Figure 3-12). The thermal conductivity of the YSZ coatings, made from HOSP powders, at elevated temperature using the laser flash technique at Oak Ridge National Laboratory, as shown in Fig. 3-13.

Then microstructure images for the same coating are taken at high temperature. The heating or cooling segments and rates are between the SEM and laser flash test are maintained as close as possible. Since the high temperature laser flash measurement is performed in an argon atmosphere, the finite element modeling assigns the temperature-dependent thermal conductivity of argon to the pores and cracks, and assign the high temperature bulk YSZ thermal conductivity values from reference to the coating material. The model and experimental results are shown in Fig. 3-13.

3.6. Limitation of the Current Model

For room-temperature thermal conductivity modeling, only conduction heat transfer is considered in the model, since the convection and radiation are not signification due to the small void space and low temperature in the coating. At high temperature, radiation must be considered to validate and enhance the model, and it is expected that the current conduction-only model under predicts the thermal conductivity for temperature that begin to approach 900–1000^{o}C

Also, as mentioned, the proposed model can be extended to general materials in coating-based heat transfer problems, given the detail and composition of the coating. For structures that contain more than two components, e.g., metallic coatings that have significant oxides, a single threshold level for the microstructure image is not adequate to

differentiate each component. In this case, other methods are needed to determine the distribution of each component, for example, the Energy Dispersive Spectroscopy (EDS).

3.7. Concluding Remarks

An microstructure-based finite element model is presented to estimate thermal transport properties for thermal spray coatings. A high-resolution scanning electron microscope image of a coating cross section is used to generate a grayscale image that is subsequently processed to identify distinct materials in the coating cross section. The image is then used directly as the mesh for a finite element model, with bulk transport properties assigned to each material. Results are presented for YSZ, molybdenum, alumina, and Ni-5wt.%Al coatings. The approach shows promise for assessing the contributions of different defects in thermal spray coatings as well as the possibility of assessing the importance of features such as the interface, pores, cracks, and foreign material on the overall transport in a film, which, to date, has remained a challenging task. With the above techniques, thermal conductivity of thermal spray coatings is modeled at ambient and high temperatures and compared with experimental results by laser flash techniques. As a result, the image-based model allows assessment of local variability, role of imperfection and interfacial phenomena, and will help to guide in coating development and optimization.

The modeling approach developed in this work, which is not sensitive to slight change on the threshold level, is to predict thermal conductivity of thermal spray coatings from SEM images of the coating microstructure. Comparisons are made between modeling and experimental values, which were obtained using the flash method.

For YSZ coatings, the FEA model captures the trends for through-thickness and in-plane thermal conductivities both before and after annealing. The modeling results are generally higher than the experimental results, which may be due to enhanced phonon and photon scattering at the micro- and nano-scale interfaces. A recent study on multi-layered YSZ films shows that the thermal conductivity of films decreased with increasing number of layers, which will increase of the phonon and photon scattering. A model with splat-splat contact thermal resistance is desired to reveal the interface effect. In addition, using 2-D images to simulate a 3-D system can also cause potential problem and a model based on 3-D is desired.

For Mo coatings, comparing with the experimental results, the finite element modeling results are lower. It can be seen that in Fig. 3-3, some of the black regions, which looks like vertical cracks, are actually grain boundaries. However, image analysis converts grain boundaries into the pores and cracks network. By assigning air thermal conductivity to the grain boundaries, the modeling results are lower than expected.

In Fig. 3-5a, for TWA and APS coatings, which contain more oxidation, the modeling thermal conductivity is lower than experimental results. The reason is that the model

does not recognize the oxide distribution in the black areas. However, in Fig. 3-5b, for HVOF coatings, which have less oxidation, the modeling thermal conductivity is higher than the measurement data. This is possibly because the model does not recognize the large number of fine interfaces in HOVF coatings, which will increase the phonon and photon scattering effect.

For high temperature modeling, it can be seen that the difference between the modeling and the experiment results, measured by flash method, increases when the temperature increases. This is likely due to the additional contribution from other mechanisms, which are not yet included in the model.

In summary, this work shows that the image-based technique is an effective tool to assess the thermal conductivity of thermal spray coatings. However, the discrepancy in the comparison of predictions and experiments shows this technique will be improved with further investigation.

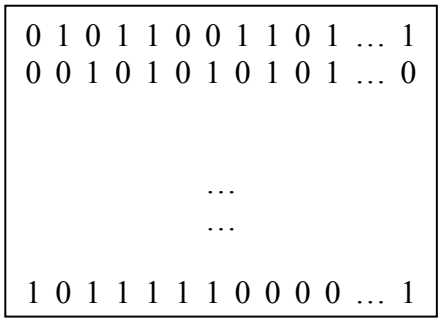

(a)

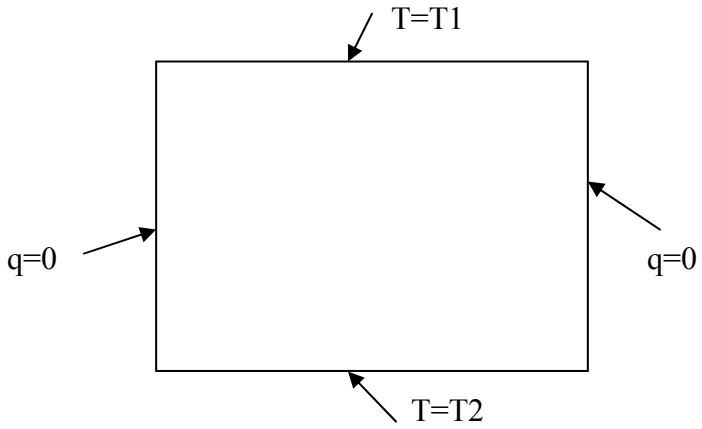

(b)

Figure 3-1. Steady-state thermal conductivity modeling: (a) A matrix that presents a binary image, for example, the image in figure 2-5b, (b) Boundary conditions for finite element thermal conductivity model.

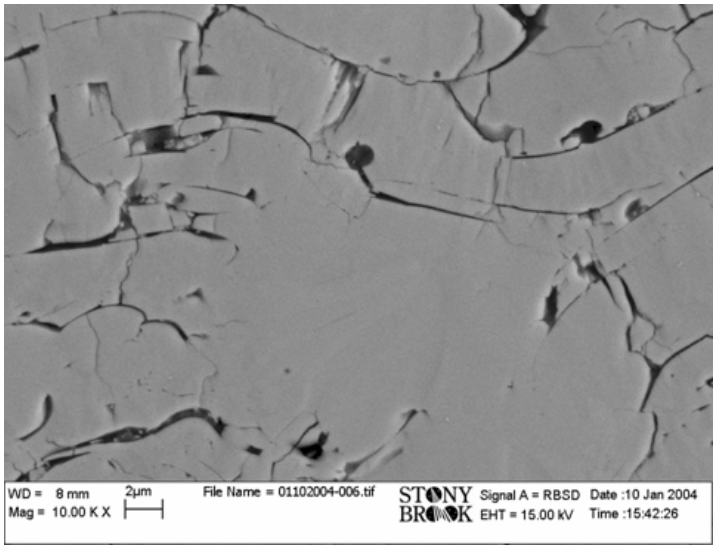

(a)

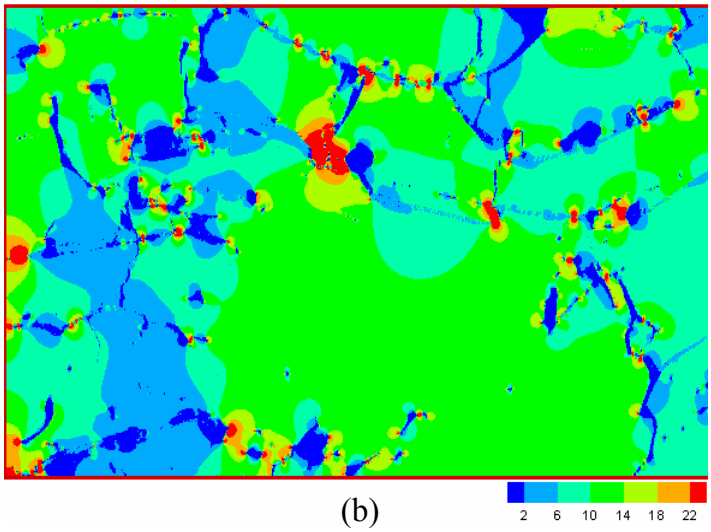

(b)

Figure 3-2. Heat flux counter: (a) Original SEM image of YSZ coating, (b) Vertical heat flux counter. Blue and red represent the lowest and highest heat fluxes respectively.

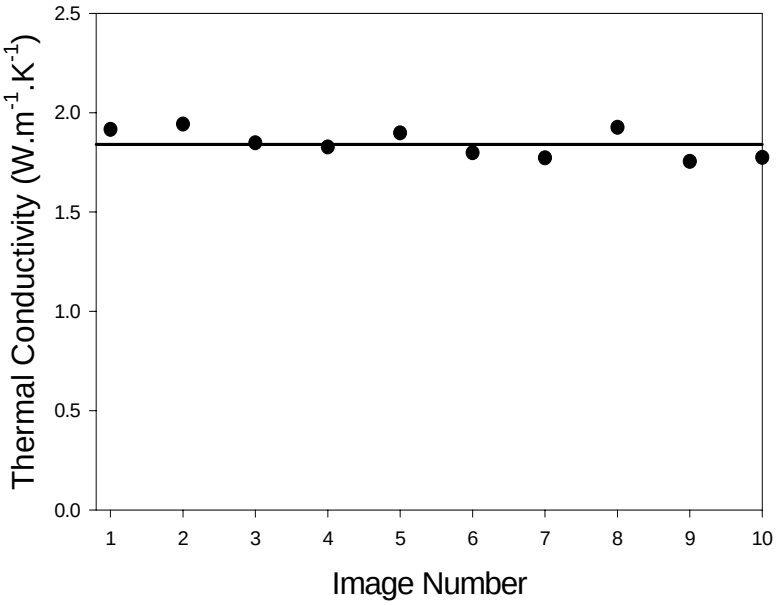

Figure 3-3. Results from several images taken from distinct locations for the same thermal sprayed YSZ coating.

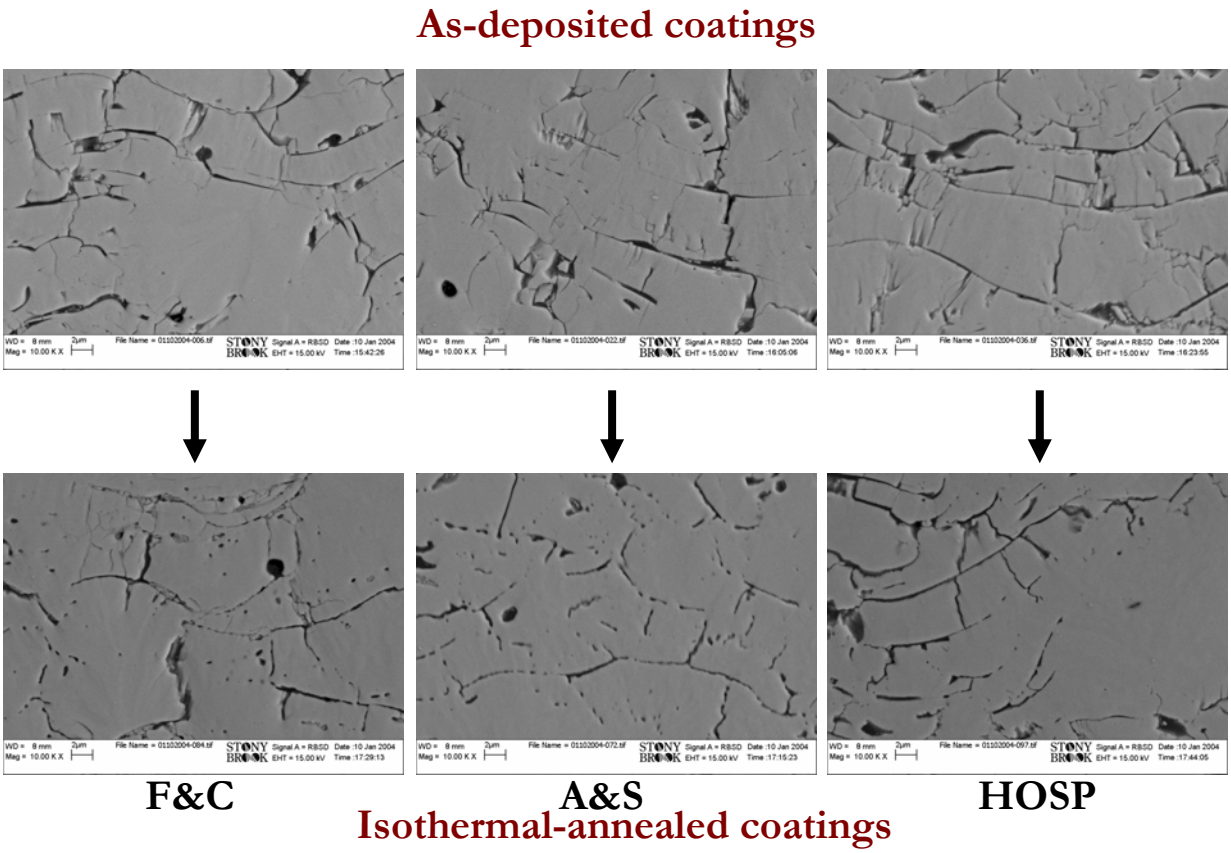

Figure 3-4. SEM image YSZ coatings before and after annealing.

Table 3-1. Thermal conductivity of YSZ coatings (Bulk value=2.5 W/m.K).

	Through-Thickness Thermal Conductivity (W/m.K)			In-plane Thermal Conductivity (W/m.K)		
	Experiment	FEA	Difference	Experiment	FEA	Difference
HOSP As-sprayed	1.10±0.09	1.32±0.13	20%	0.84±0.07	1.60±0.16	90%
HOSP Annealed	1.30±0.10	1.42±0.14	9%	1.10±0.09	1.63±0.16	48%
F&C As-sprayed	1.23±0.10	1.56±0.16	27%	1.49±0.12	1.78±0.18	19%
F&C Annealed	1.85±0.15	1.78±0.18	-4%	1.65±0.13	1.90±0.19	15%
A&S As-sprayed	1.12±0.09	1.75±0.18	56%	N/A	1.46±0.15	N/A
A&S Annealed	1.43±0.11	1.77±0.18	24%	N/A	1.90±0.20	N/A

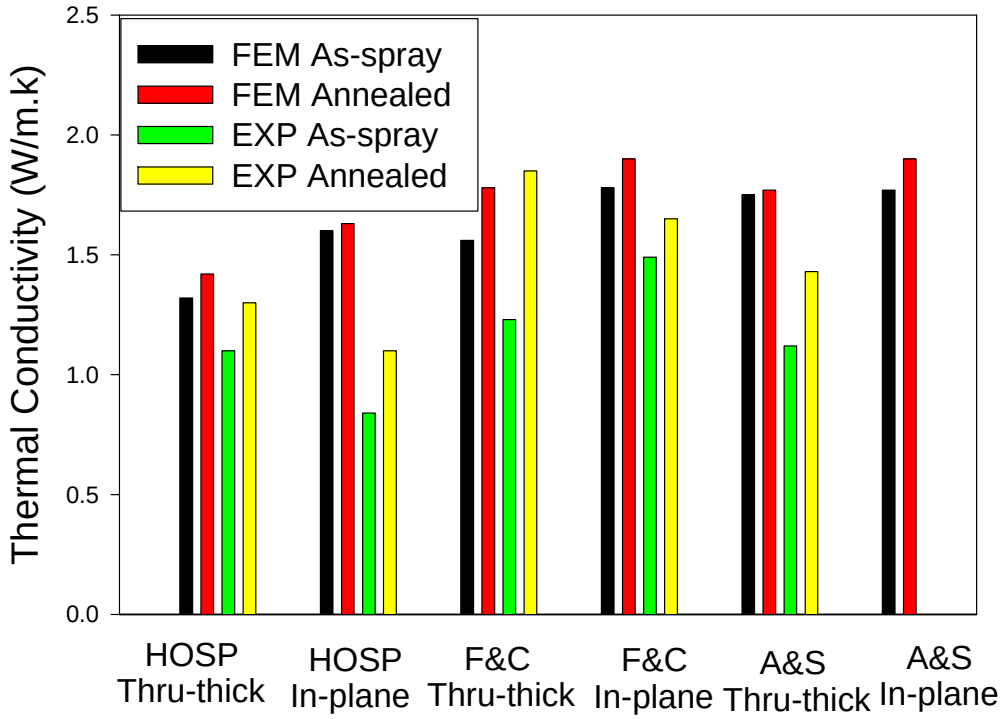

Figure 3-5. Modeling and experiment results for YSZ coatings thermal conductivity before and after annealing for both through thickness direction and in-Plane direction.

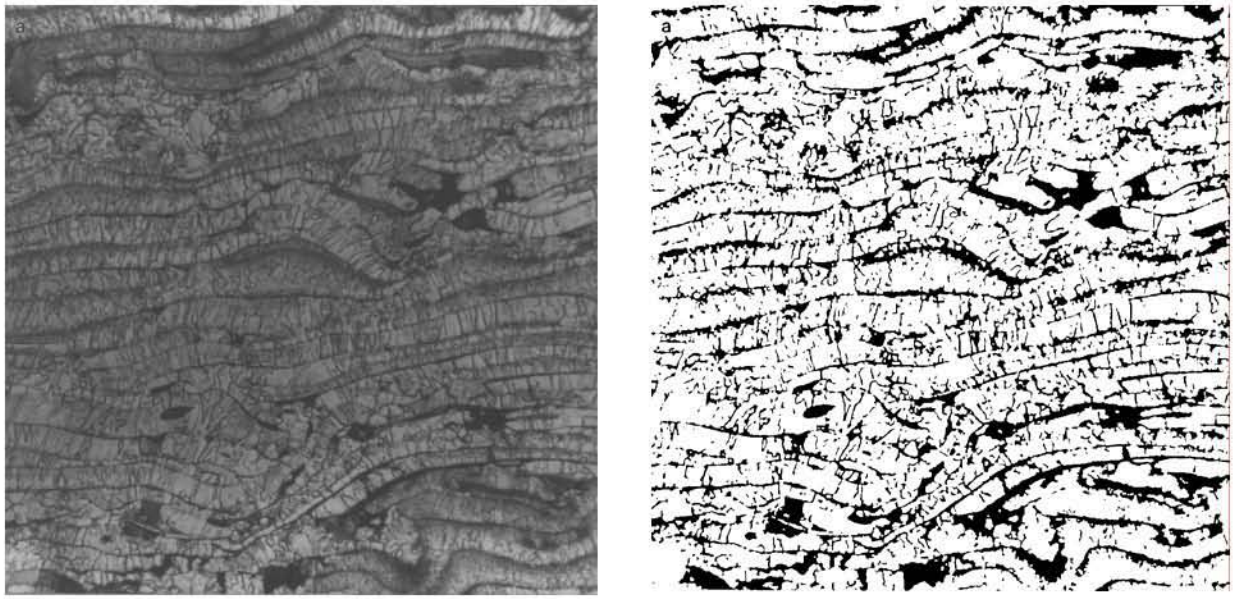

Figure 3-6. Gray-Scale and binary images for Mo coating.

Table 3-2. Thermal conductivity of Mo coating (Bulk value=142 W/m.K).

Through-Thickness Thermal Conductivity (W/m.K)			In-plane Thermal Conductivity (W/m.K)		
Experiment	FEA	Difference	Experiment	FEA	Difference
15.0±0.8	10.0±2.0	-33%	40.3±3.2	31.0±6.2	-23%

Table 3-3. Thermal conductivity of Ni-5wt%Al coatings (Bulk value=80 W/m.k)

	Through-Thickness Thermal Conductivity (W/m.K)			In-plane Thermal Conductivity (W/m.K)		
	Experiment	FEA	Difference	Experiment	FEA	Difference
TWA	17.0±0.9	10.1±2.0	-40.5%	N/A	29.5±5.9	N/A
HVOF	22.2±1.1	51.4±10.3	132%	N/A	54.7±11.0	N/A
APS	10.7±0.5	7.5±1.5	-30%	N/A	15.3±3.1	N/A

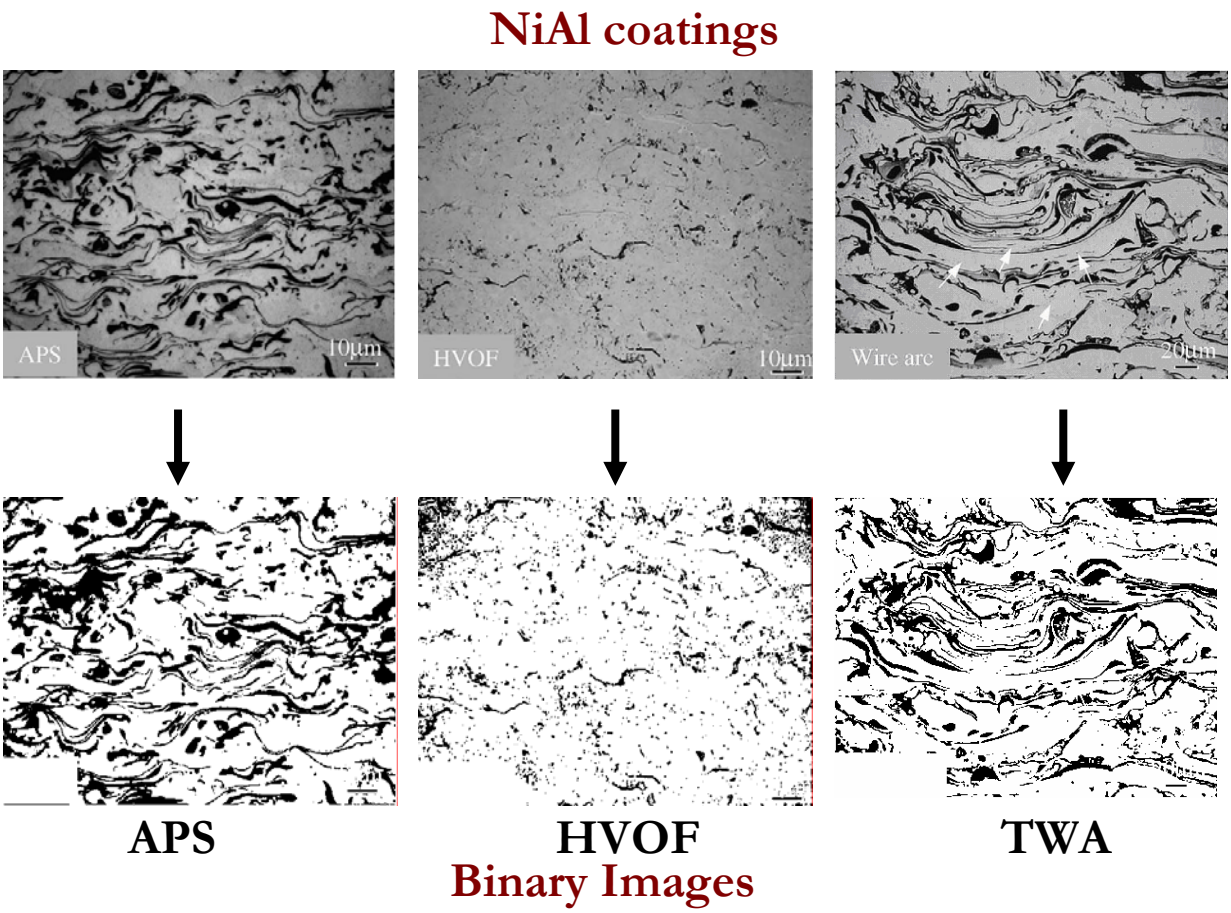

Figure 3-7. Gray-scale and B/W images for Ni-5wt.%Al coatings.

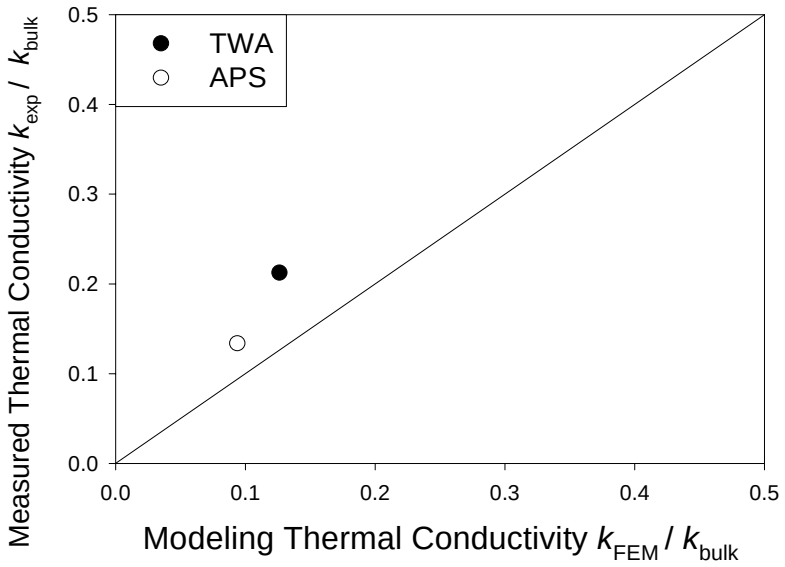

(a)

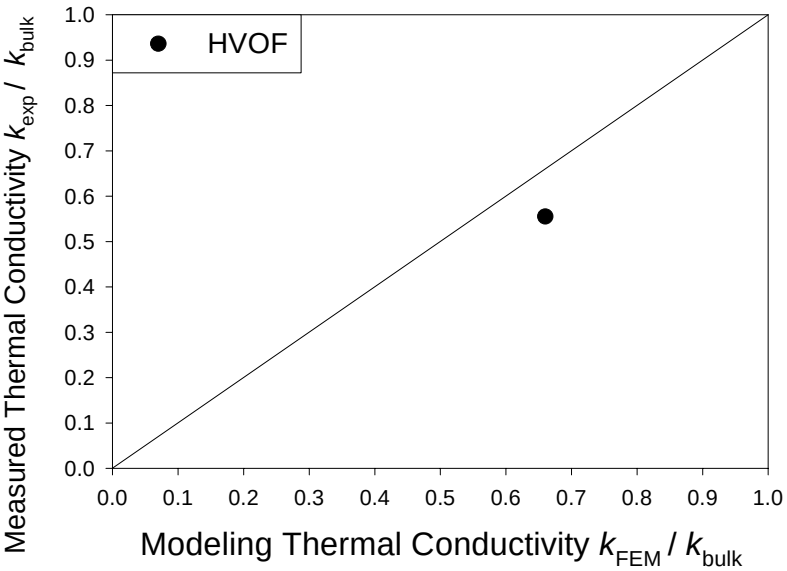

(b)

Figure 3-8. Modeling and experiment results for thermal conductivity of Ni-5wt.%Al coatings in through-thickness direction only. (a) for TWA and APS coatings, thermal conductivity for bulk material 80 W/m·k; (b) for HOVF coating, thermal conductivity for bulk material 40 W/m·k.

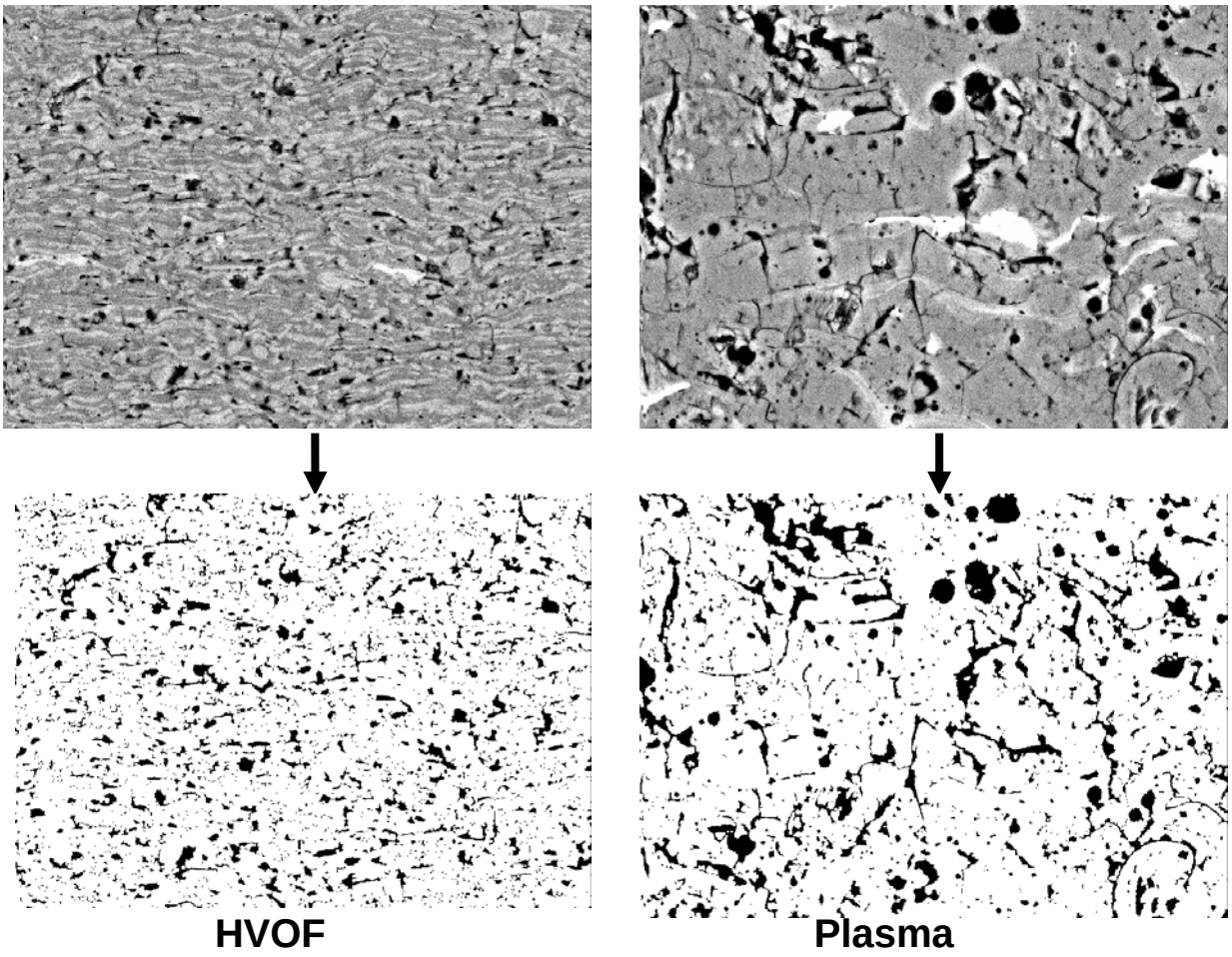

Figure 3-9. Gray-scale and B/W images for alumina coatings.

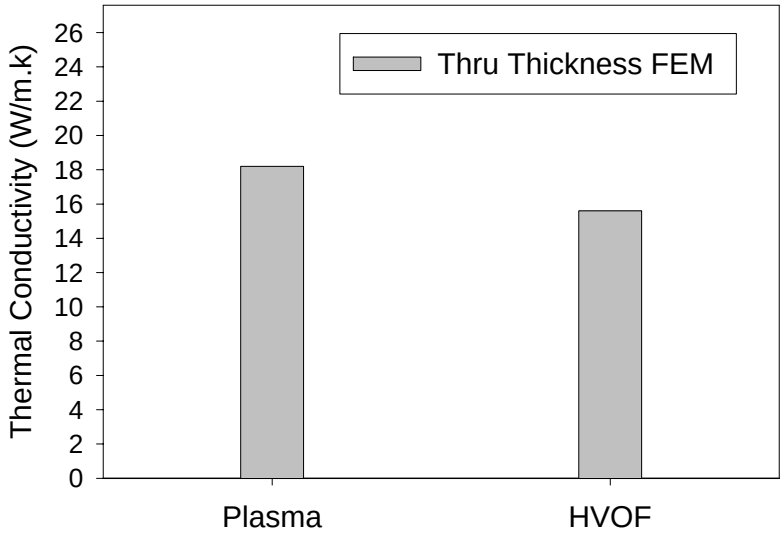

Figure 3-10. Alumina coating thermal conductivity

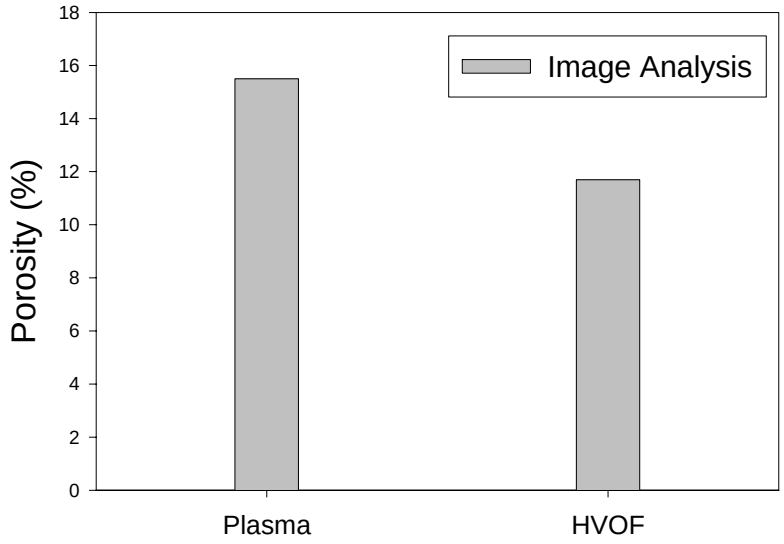

Figure 3-11. Alumina coating porosity by image analysis

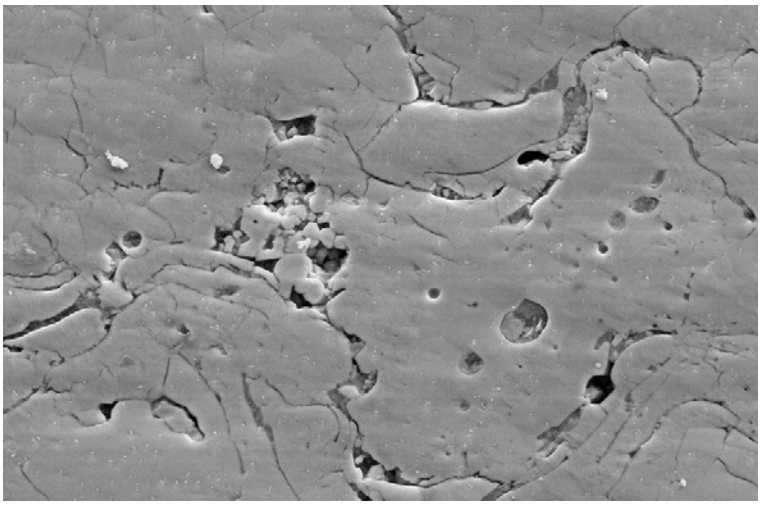

(a)

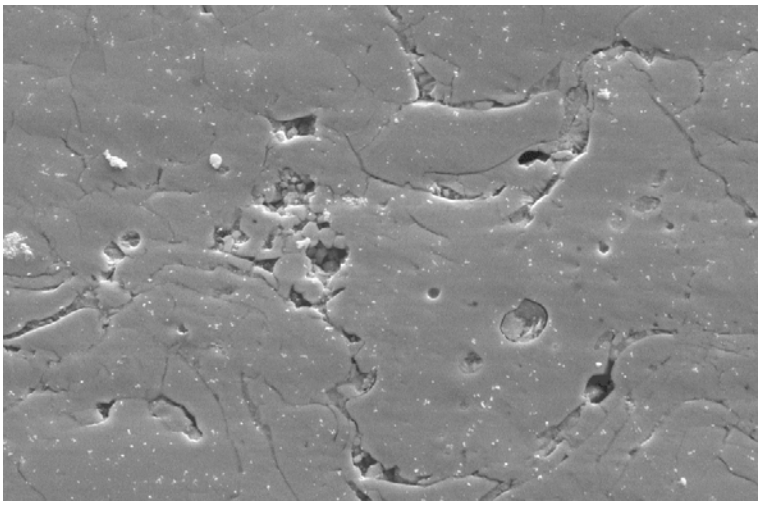

(b)

Figure 3-12. SEM images for a YSZ coating for the same location. (a) As-sprayed YSZ Coating at room temperature, (10b) After heat treatment at 1000 ^{o}C.

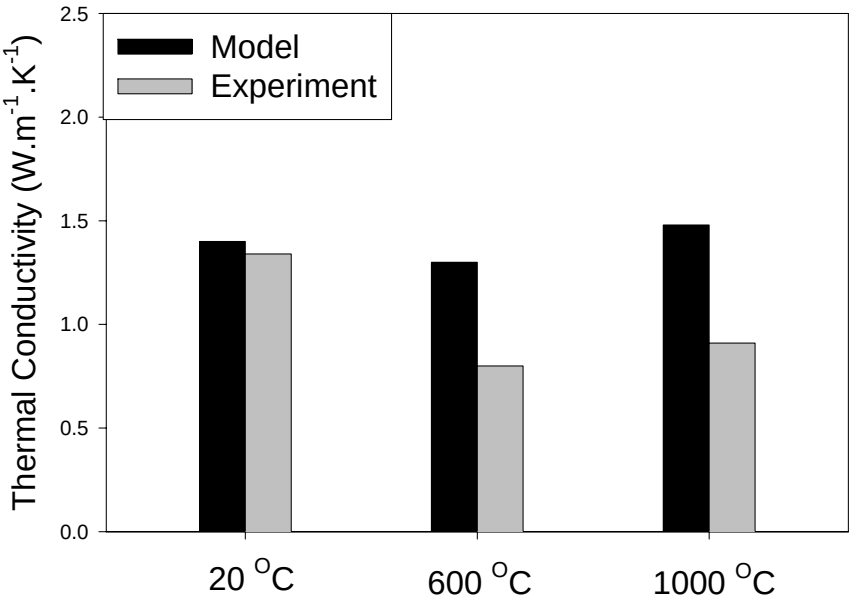

Figure 3-13. Ambient and high temperature thermal conductivity modeling and experimental results for YSZ coatings.

Chapter Four

Experimental Issues on Thermal Property Measurements

To study the microstructure-property relationship and to compare model predictions to actual coating property, experimental measurements of thermal diffusivity, specific heat and thermal conductivity at ambient and high temperatures are performed at Center for Thermal Spray Research and Oak Ridge National Laboratory.

4.1. Thermal Diffusivity Measurement by Flash Method

4.1.1. ASTM standard E1461

ASTM standard E1461 is the 'Standard Test Method for Thermal Diffusivity of Solids by the Flash Mthod'. It can be summarized as the following: 'A small, thin, disc specimen mounted horizontally or vertically is subjected to a high-intensity short duration thermal pulse.' The energy of the pulse is absorbed on the front surface of a

specimen and the resulting rear face temperature rise is measured. The ambient temperature of the specimen is controlled by a furnace or cryostat. Thermal diffusivity values are calculated from the specimen thickness and the time required for the rear face temperature rise to reach certain percentages of its maximum value. This test method is described in detail in a number of publications and review articles and has been standardized in Test Method C 714 in a moresimple form for carbons and graphites.

The pulse raises the temperature of the specimen only a few degrees above its initial ambient value. However, initially all of the energy is deposited on the front surface and this temperature may rise many degrees. If this should damage the specimen, a layer of a material with known properties (thermal diffusivity, specific heat and density) and measured thickness can be attached to the front sruface and results on the composite specimen analyzed using a two-layer method. This requires that the specific heat and density of the specimen also be known.

The essential features of the apparatus are shown in figure 4-1. These are the flash source, sample holder and envieronmental system, temperature response detector and data collection and analysis components.

4.1.2. Ambient Temperature Laser Flash Instrument

Ambient temperature thermal conductivity measurements were made using by a *Holometrix microflash* Laser Flash apparatus manufactured by *Netzsch Instruments Inc.*, which operates according to ASTM standard E1461. To measure thermal conductivity,

the Holometrix instrument uses a high-power short-pulse laser to heat the bottom surface of a thin specimen. The heat transferred through the specimen results in a temperature rise at the top surface that is measured by an infrared detector. Analysis of the bottom-surface temperature time-varying history allows the determination of thermal diffusivity. Specific heat can be measured with the laser flash method by comparing the temperature rise of the sample to the temperature rise of a reference sample of known specific heat tested under the same test conditions. This temperature rise is recorded during the diffusivity measurement, so the specific heat can be calculated from the same data. The apparent density of the sample was obtained by measuring dimensions and weight. The thermal conductivity is calculated from thermal diffusivity, specific heat, and density.

The Holometrix instrument can measure both through-thickness and in-plane direction thermal conductivity for free-standing coatings. For though-thickness measurement, the shape of the coating specimen is a thin disk with diameter of 12.7 mm and thickness of 0.3-2 mm. During the measurement, the bottom-surface of the sample is uniformly irradiated by the laser pulse and the temperature-time is recorded for the central point on the other side. For an in-plane measurement, a squared-shaped sample (25.4 mm × 25.4 mm) is required and the laser pulse only irradiates the central region of the bottom surface. The temperature is recorded on the backside of the film using an infrared detector, and the measured temperature history can then be used to estimate thermal diffusivity and conductivity.

Using the experimental setups discussed above, ambient thermal conductivity are obtained of thermal sprayed ZrO_2-8wt%Y_2O_3, molybdenum, alumina and Ni-5wt.%Al coatings and the results were previously shown in Chapter two, which were found to be in good agreement with the predicted data.

4.1.3. Ambient Temperature Thermal Diffusivity Test Repeatability

The standard deviation of this technique with Holometrix instrument has been characterized by Chi et al.. The standard deviation of thermal conductivity measurement for the same coating is 8%. In this work, the standard deviation for through-thickness thermal conductivity measurement is typically 8%, which is the value used for all measurement in this work.

4.1.4. High Temperature Laser Flash Facilities

High temperature thermal diffusivity measurements are made at Oak Ridge National Laboratory, in an argon atmosphere using a *Flashline FL-5000* laser flash instrument manufactured by *Anter Corporation*. The multiple furnace laser flash thermal diffusivity system is equipped with a moveable Nd:Glass laser unit, two IR detectors and four furnaces for precise measurements of thermal diffusivity over the temperature rage from -150^{o}C to 2500^{o}C. All furnaces can operate in vacuum and inert gas; the environmental effects furnace also supports oxidizing and reducing environments. To increase testing speed the graphite and aluminum furnaces are both equipped with six sample carousels. The multiple station and concurrent testing concepts have been proven successful for

materials characterization by Wang at el. The schematic of the temperature dependent thermal diffusivity testing system are shown in figure 4-2.

4.1.5. High Temperature Thermal Diffusivity Test Repeatability

To investigate repeatability of the thermal diffusivity test, during thermal diffusivity measurement, the system temperature was maintained at 1000^{o}C for 80 minutes during the second round heating process. The coating thermal diffusivity was measured 9 times in 80 minutes (10 minutes time interval). The results are shown in figure 4-3, figure 4-4, figure 4-5 and figure 4-6.

4.2. Specific Heat Measurement

High temperature specific heat measurements were made on a Netzsch scanning calorimeter (model STA 449C, up to 1600 ^{o}C). The specific heat of an unknown sample can be calculated by differentiating the heat capacity of sample and a standard sample, for example, sapphire with known specific heat. The raw DSC data is shown in figure 4-7, and the calculated YSZ Specific Heat results are shown in figure 4-8.

4.3. Density Measurement

The apparent density of the sample was obtained by measuring dimensions and weight. The thermal conductivity was calculated from thermal diffusivity, specific heat, and density. The density of sample slightly changes (less than 2%) after annealing.

4.4. Thermal Conductivity Measurement

Given the data of thermal diffusivity, specific heat and apparent density, the thermal conductivity of YSZ coatings can be calculated by the equation below:

$$k = \alpha \cdot \rho \cdot c_p$$

where α , ρ and c_p are the thermal diffusivity, density and specific heat, respectively.

4.5. Validation and Correction for Flash Method on TBCs

4.5.1. Heterogeneity Effects

Flash method is evaluated by finite element analysis to investigate the error for this method on heterogeneous materials. Two analysis domains are analyzed, which have different heterogeneity. The structure of each domain is shown in figure 4-9, and size distribution of the pores and cracks inside the domain is shown in figure 4-10. Standard

Deviation on the size distribution is 167, while the second is 1286, which means the first domain has lower heterogeneity than the second one. The calculated error for domain one and domain two are 1% and 10% comparing with the steady-state method, on which the effective thermal conductivity is defined.

According to the above results, material with higher heterogeneity will result in higher error when using the standard flash method. The domain one is an actual micrograph of a thermal spray coating. The microstructure of thermal spray coating is complicated. However, since the micro- and nano-size pores, cracks and fine interfaces are randomly and uniformly distributed throughout the microstructure, the overall heterogeneity of a thermal spray coating is low enough to satisfy the flash method requirements. The conclusion is it is ok to use standard flash method for thermal spray coating. But for other materials with high heterogeneity, for example, with the similar structure as the domain number two above, standard laser flash needs corrections.

Further study is required to investigate the topology effect on the flash method. It is believed that the size distribution of objects, orientation of objects and the thermal conductivity ratio of the involved materials are the key parameters. From this point, a metal coating will have higher error than that of ceramic coating. A three-dimensional model will help to enhance this study.

4.5.2. Radiation Effects

For the standard flash method, the specimen is coated with graphite to satify black body assumption. By doing this, the emissivity of the specimen is closed to 1, which needed to fully absorb the laser energy and to make accurate temperature measurement for the rear surface. However, if the specimen is transparent near the peak wavelength of the radiation at a certain temperature, the two graphite surfaces can 'see' each other, so the net heat transfer between the two parallel surfaces will be significant, especially at high temperatures, if the temperature difference between the two surfaces is large.

In the flash method, once the laser pulse reaches the top surface, the temperature jump on it can be huge, for example, 50^{o}C jump above the environment (e.g. 1200^{o}C). Two tests are performed on a bulk YSZ specimen and a YSZ coating, respectively, and the testing temperatures are 1085^{o}C and 1191^{o}C, respectively. The temperature-time history curves are recorded and shown in figure 4-11. It can be seen that in figure 4-11a, since the bulk YSZ is semi-transparent (transmittance about 70-80%) to the radiation at 1085^{o}C, there is a huge initial temperature rise on the rear surface, and this rise will cause significant error for the final diffusivity result, which is calculated according to the half-time. In the other case, for the YSZ coatings, there is still bulk YSZ material inside, however, there are a lot of defects, including pores, cracks and interfaces, which will provide significant photon scattering to the radiation and make the overall system opaque to the radiation. This is indicated in figure 4-11b, the coating case has almost negligible initial jump compared with the bulk case. Again, this study proves that the error caused

by radiation effects in general thermal spray coatings (thickness larger than 500 microns) is minor.

4.6. Results and Discussion

4.6.1. Short-term Annealing: Three-Round Test

Two coating systems made from two different YSZ powder morphologies, HOSP and F&C, were investigated. For each coating system, an as-sprayed sample and a short-term (10 hours) annealed sample were prepared for thermal diffusivity test. The annealing condition is 10 hours at 1200^{o}C.

The thermal diffusivity experiment was performed in the following procedures:

1) Room temperature (RT) thermal diffusivity test.
2) 1st round heating, 100-500^{o}C thermal diffusivity test and then cooled down to RT.
3) 1st round heating, 650-1400^{o}C thermal diffusivity test. Note: Phase change during annealing above 1200^{o}C for YSZ coatings will cause significant phase change, which will dramatically increase the thermal conductivity of the bulk YSZ material and consequently increase the coating conductivity
4) 1st round cooling, 1400-600^{o}C thermal diffusivity test and then cooled down to RT.
5) Room temperature (RT) thermal diffusivity test.

6) 2nd round heating, 650-1400°C thermal diffusivity test, then cooled down to RT.

Note:

Procedure 7) and 8) are only for HOSP and HOSP Annealed samples

7) Room temperature (RT) thermal diffusivity test

8) 3rd round heating, 100-500°C thermal diffusivity test, then cooled down to RT

9) 3rd round heating, 650-1400°C thermal diffusivity test.

The thermal diffusivity results are shown in figure 4-12, figure 4-13, figure 4-14 and figure 4-15, and the corresponding calculated thermal conductivity results are shown in figure 4-16, figure. 4-17, figure 4-18 and figure 4-19.

From the data of thermal conductivity during the three rounds of test, the annealing effect can be seen. For the annealed samples, the data curves of the three round tests are near. However, for as-sprayed samples the difference of the three test curves is big. This is because the high temperature measurement can be considered as a kind of heat treatment. The annealed samples are already pre heat treated. So the additional heat treatment of annealed samples is not as obvious as that of as-sprayed samples.

4.6.2. Long-term Annealing: Two-Round Test

One as-sprayed F&C coating and one corresponding long-term annealed coating were tested. The annealing condition is 170 hours at 1200°C.

The thermal diffusivity experiment was performed in the following procedures:

1) Room temperature (RT) thermal diffusivity test.

2) 1st round heating, 100-500°C thermal diffusivity test and then cooled down to RT.

3) 1st round heating, 650-1200°C thermal diffusivity test. Note: The increase in thermal conductivity during annealing at 1200°C is mainly due to the topological microstructure change, i.e. the pores and cracks network change, but not the phase change.

4) 2nd round heating, 100-500°C thermal diffusivity test and then cooled down to RT.

5) 2nd round heating, 650-1200°C thermal diffusivity test.

The thermal diffusivity results are shown in figure 4-20 and figure 4-21, and the corresponding calculated thermal conductivity results are shown in figure 4-22 and figure 4-23.

From the data of thermal conductivity during the two rounds of test, similar trend is found. But since the annealing temperature is 1200°C, and the measuring temperature is no more than 1200°C, the measuring segment has almost no effect on the annealed sample, while the effect on the as-sprayed sample is as significant as before.

4.7. Concluding Remarks

In this work, high-temperature thermal property measurements are only made to YSZ coating. YSZ is known to undergo a variety of changes at long-term (100s of hours) exposure to elevated temperatures, including the significant result that its thermal conductivity varies at different temperatures and will increase after long-term heat treatment.

Moreover, the error of the standard flash method is evaluated in the case of heterogeneity effects and radiation effects. It turned out, the flash method has small error when measuring the diffusivity of thermal spray coatings.

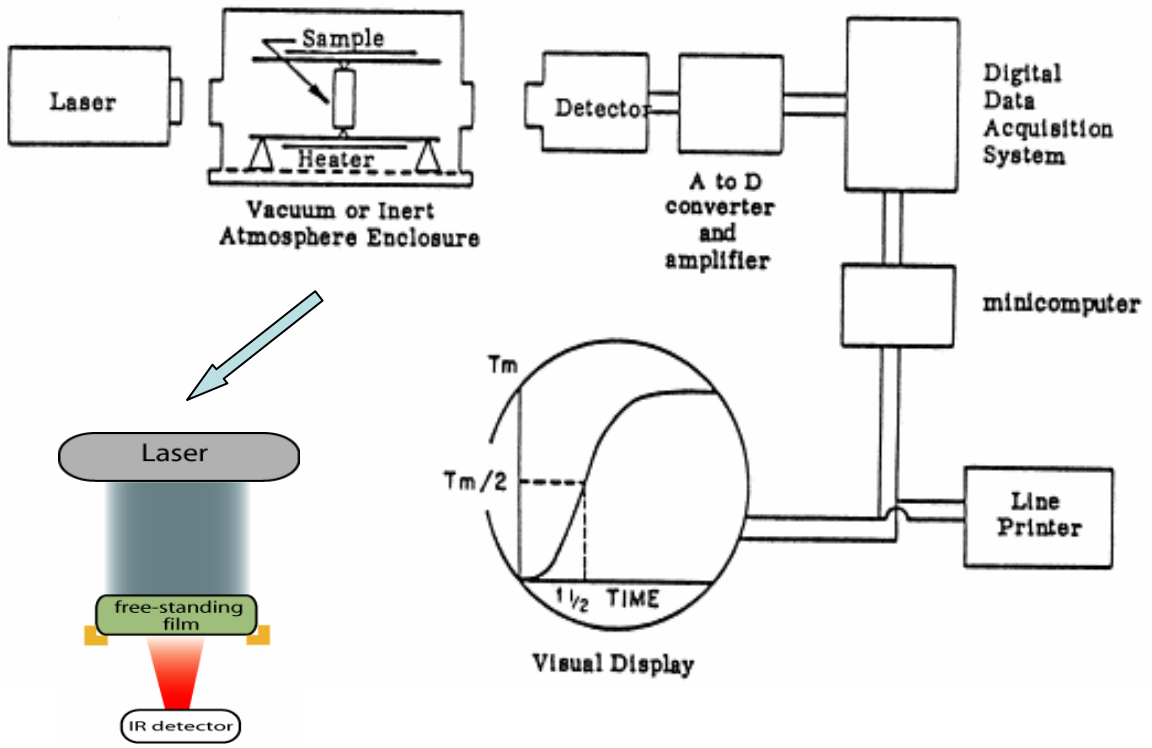

Figure 4-1. General flash diffusivity apparatus schematic (Courtesy: ASTM Standard E1461).

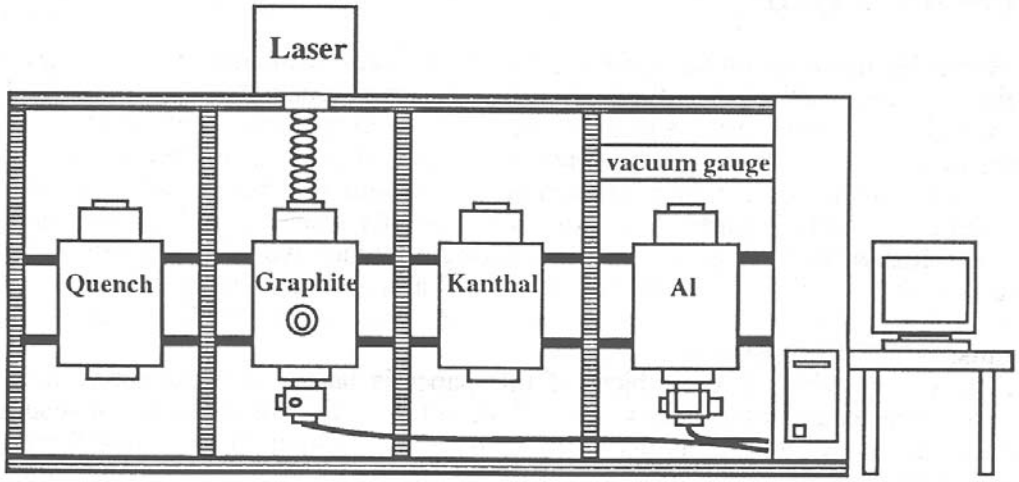

Figure 4-2. The schematic of the temperature dependent thermal diffusivity testing system at the High Temperature Material Laboratory, Oak Ridge National Laboratory. (Image courtesy: H. Wang et al., Multiple Station Thermal Diffusivity Instrument).

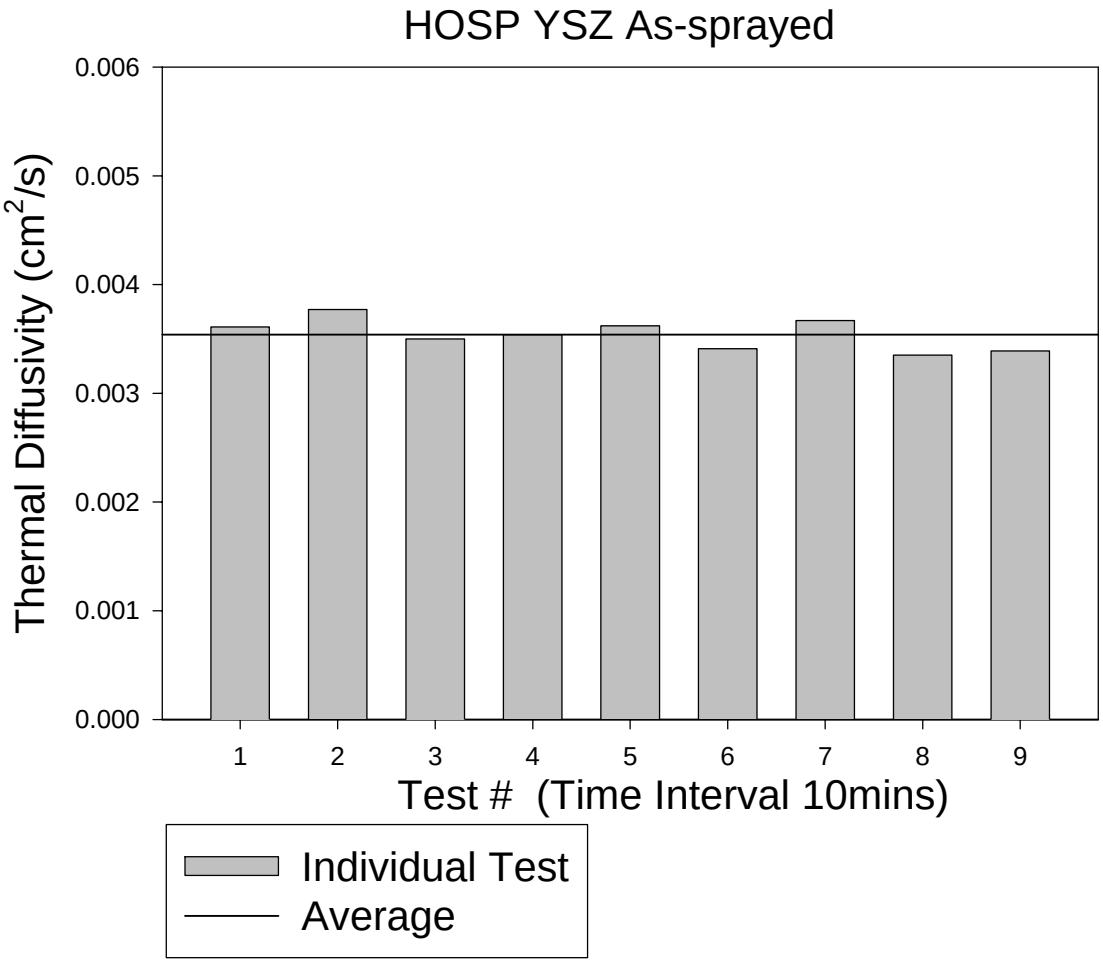

Figure 4-3. Repeatability test for thermal diffusivity: HOSP YSZ, as-sprayed.

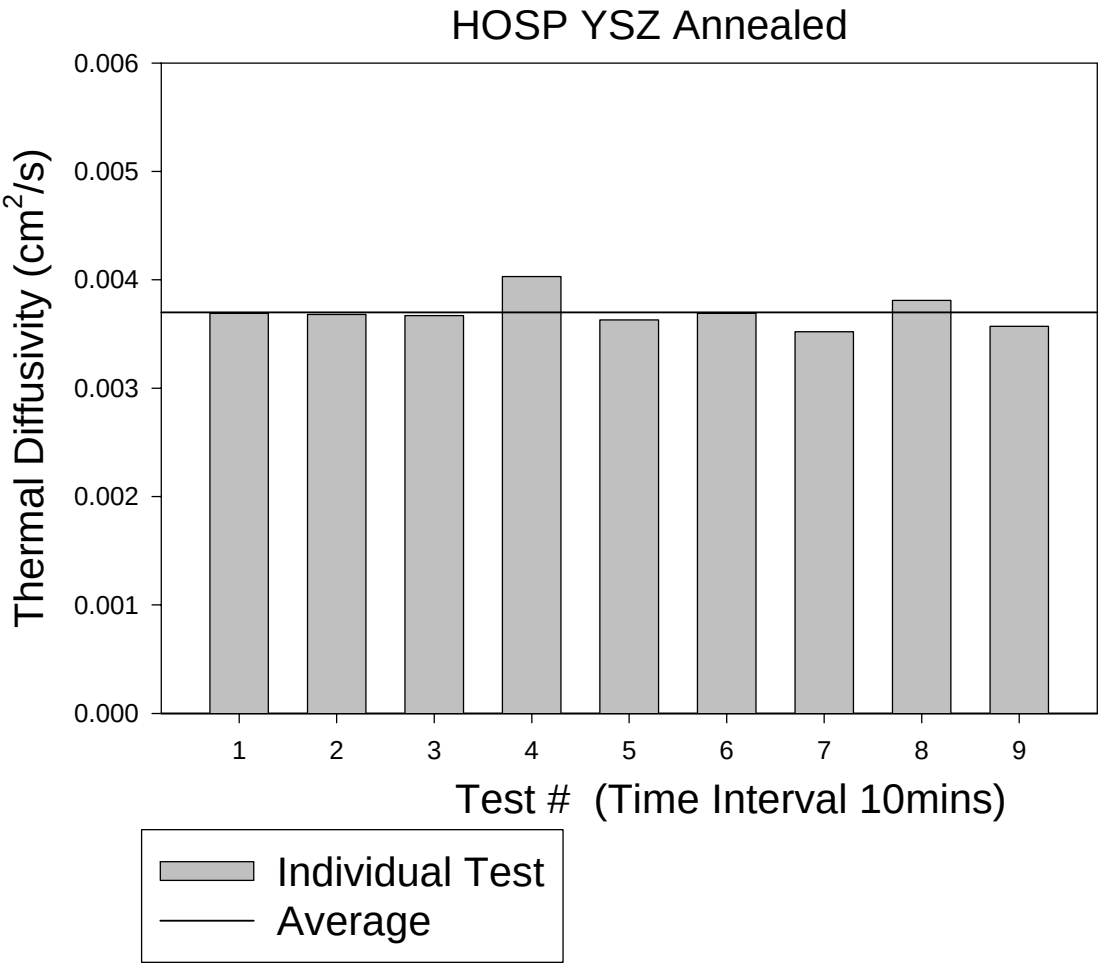

Figure 4-4. Repeatability test for thermal diffusivity: HOSP YSZ, annealed.

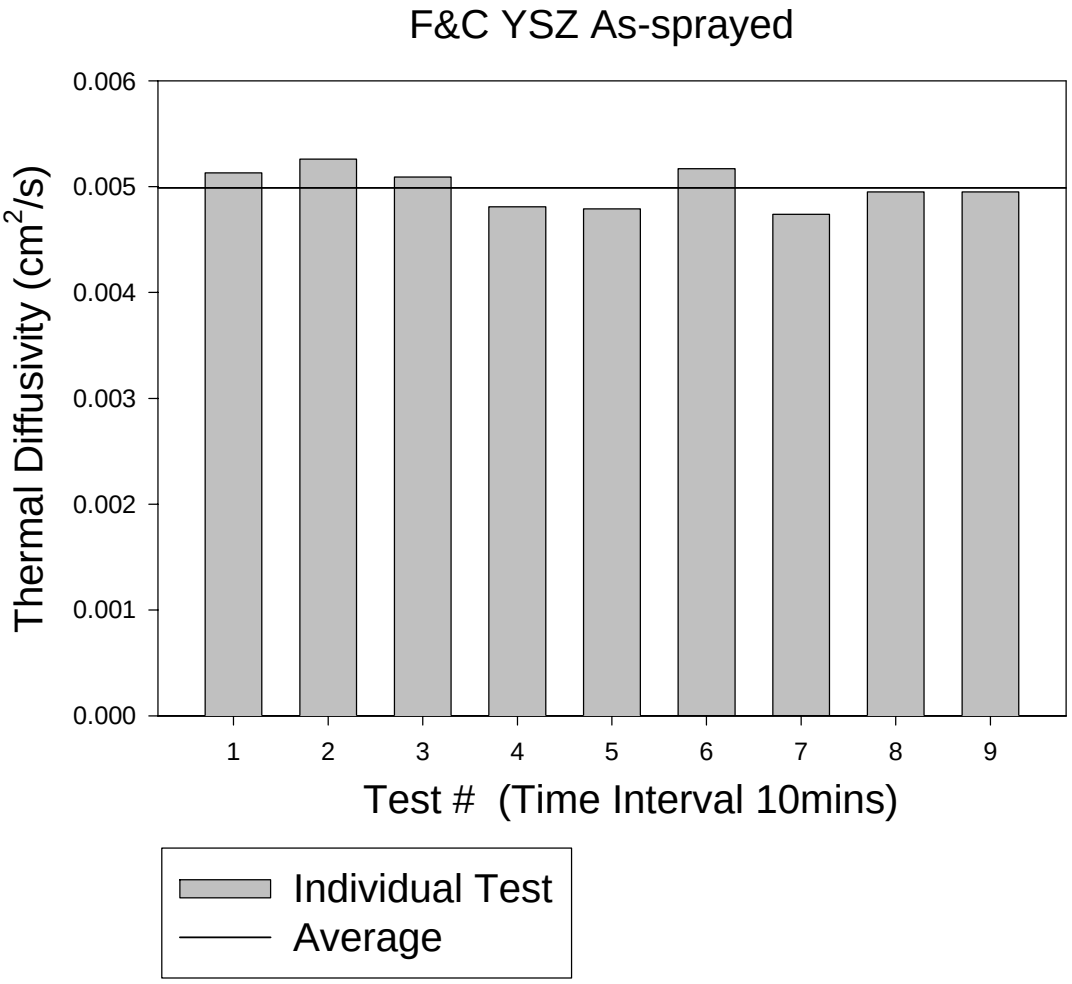

Figure 4-5. Repeatability test for thermal diffusivity: F&C YSZ, as-sprayed.

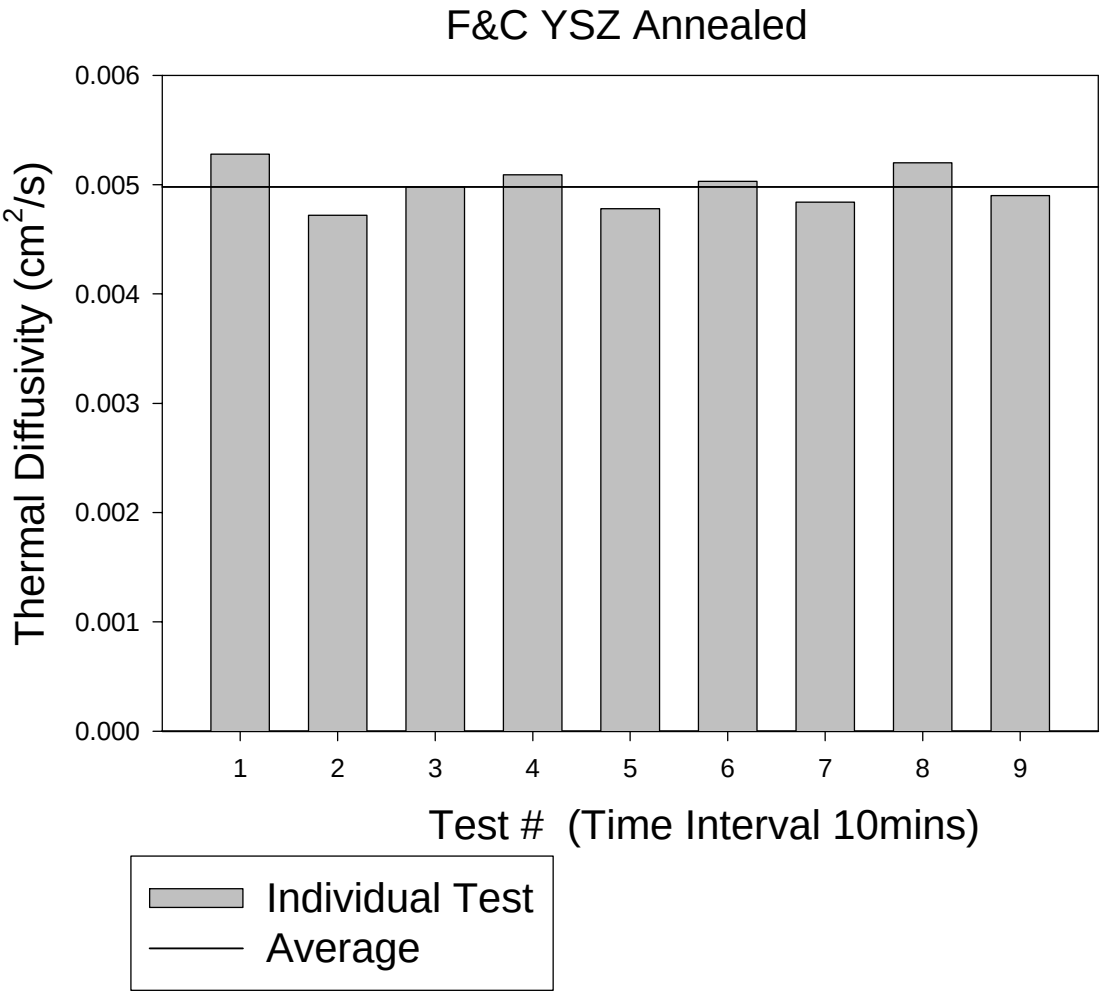

Figure 4-6. Repeatability test for thermal diffusivity: F&C YSZ, annealed.

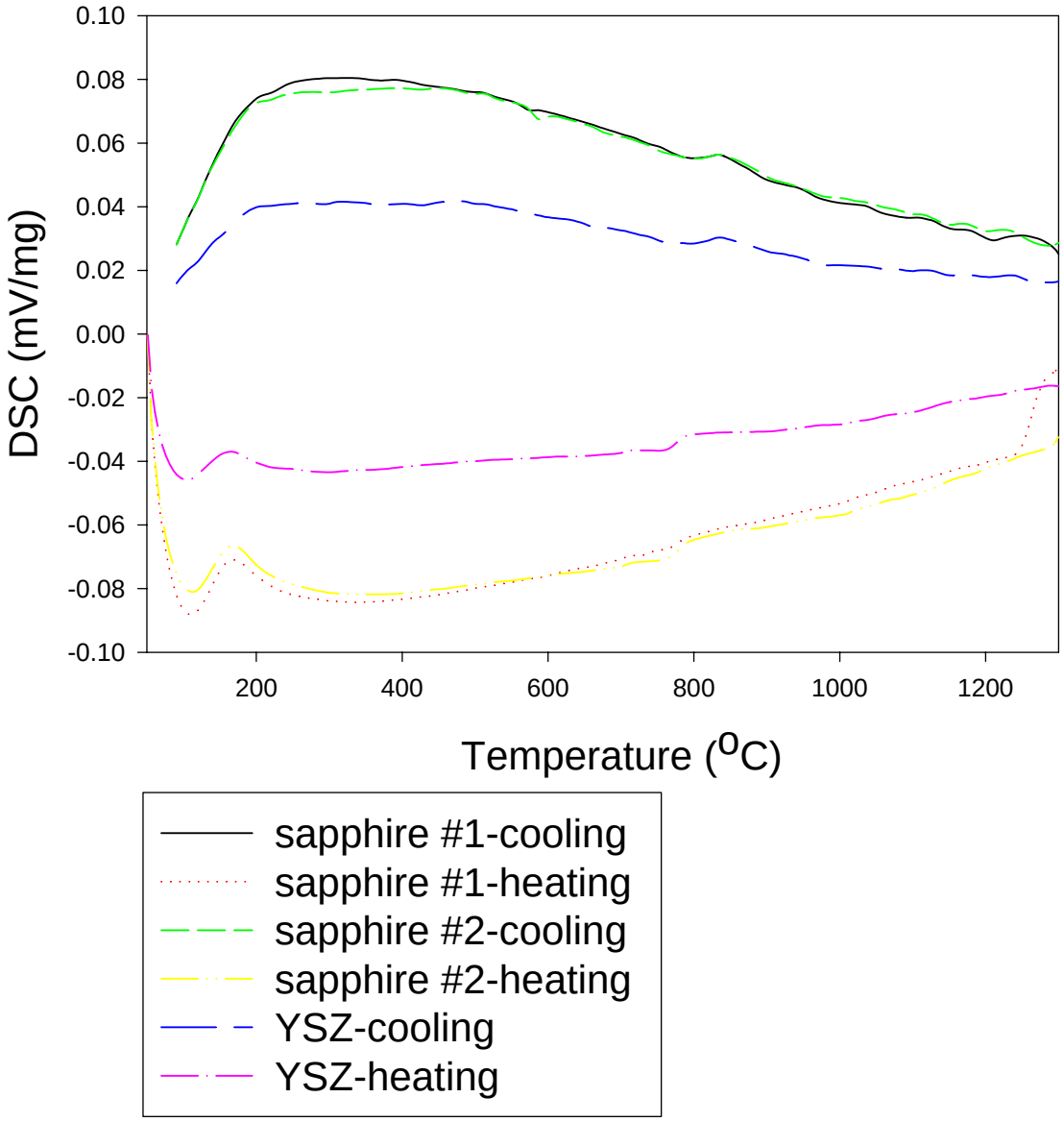

Figure 4-7. Raw DSC Data.

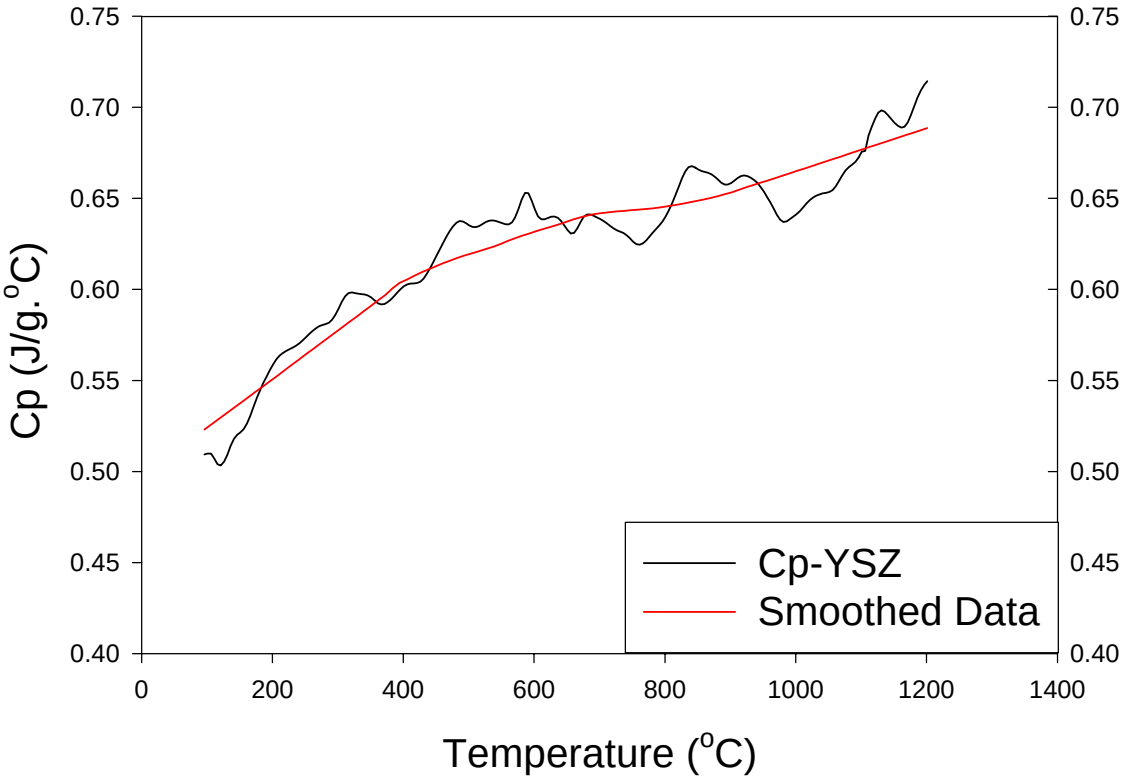

Figure 4-8. A calculated specific heat (Cp) curve for YSZ coating.

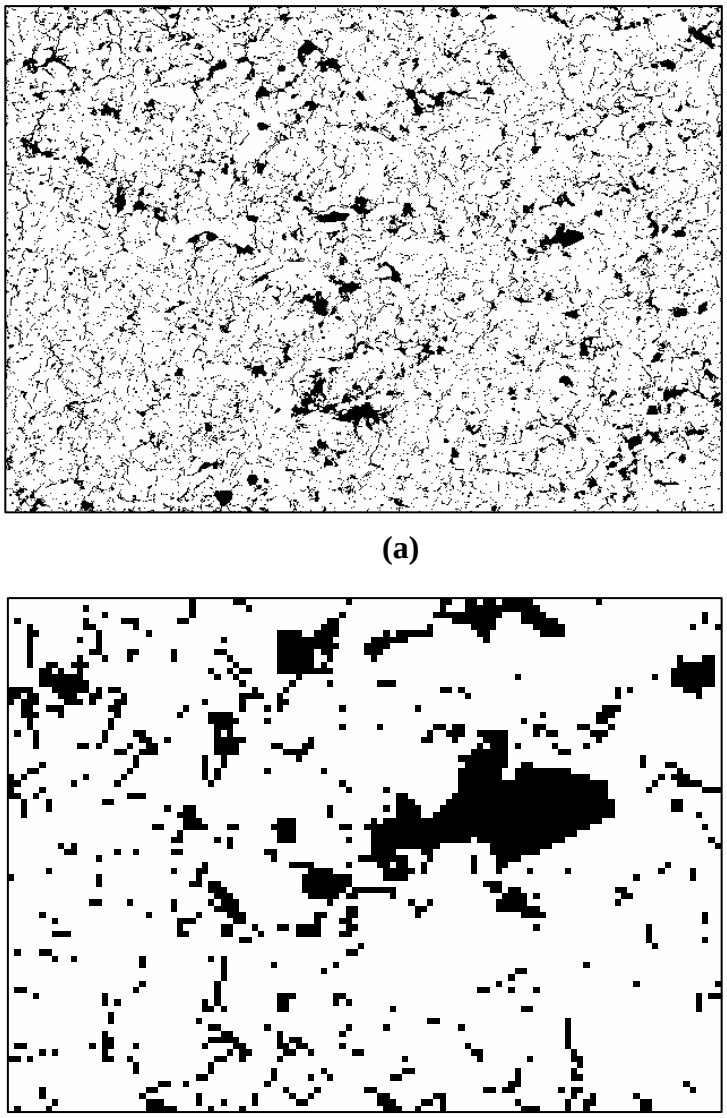

Figure 4-9. Structure domain for finite element analysis on the flash method, (a) low homogeneity, (b) high homogeneity.

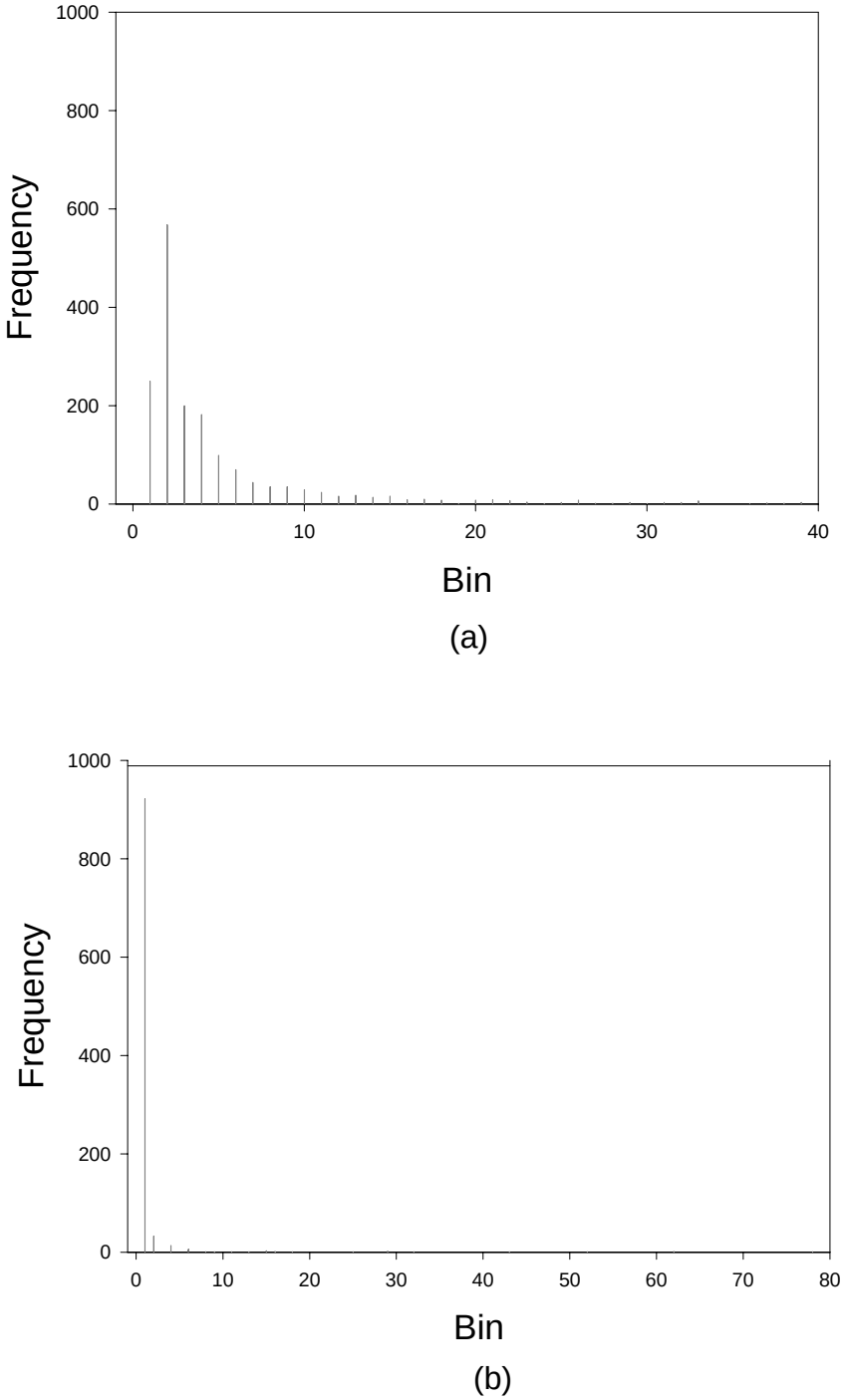

Figure 4-10. Size distributions. (a) for domain in figure 4-9a, (b) for domain in figure 4-9b.

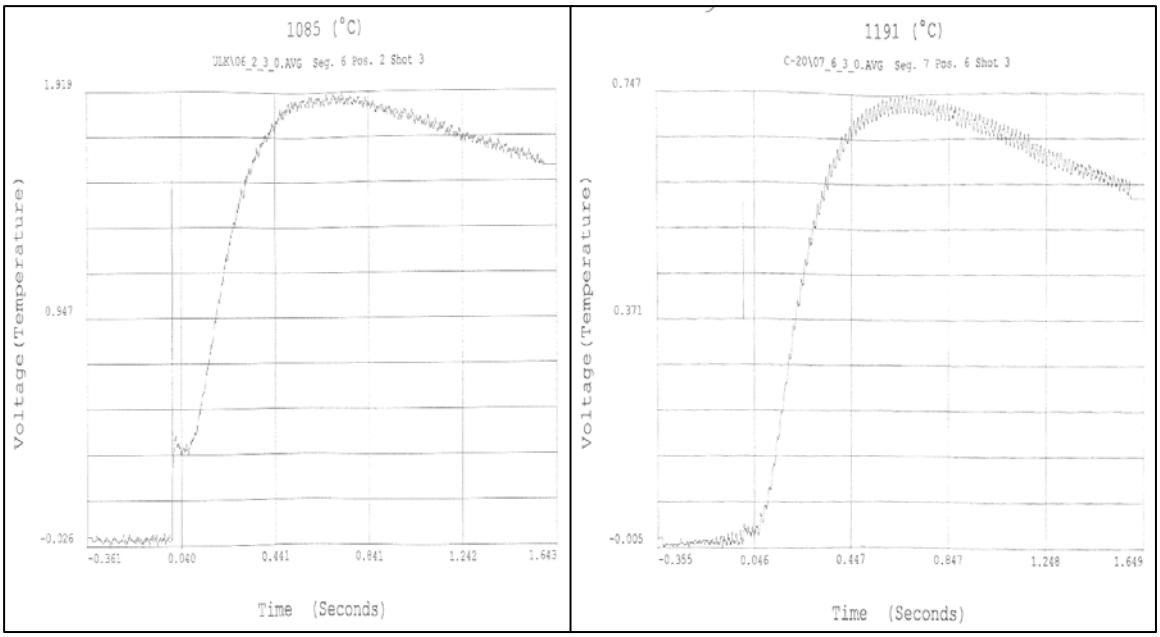

(a) Bulk YSZ: Semi-transparent (b) YSZ Coating: Opaque

Figure 4-11. Temperature-time history curves. (a) for bulk YSZ, (b) YSZ coating.

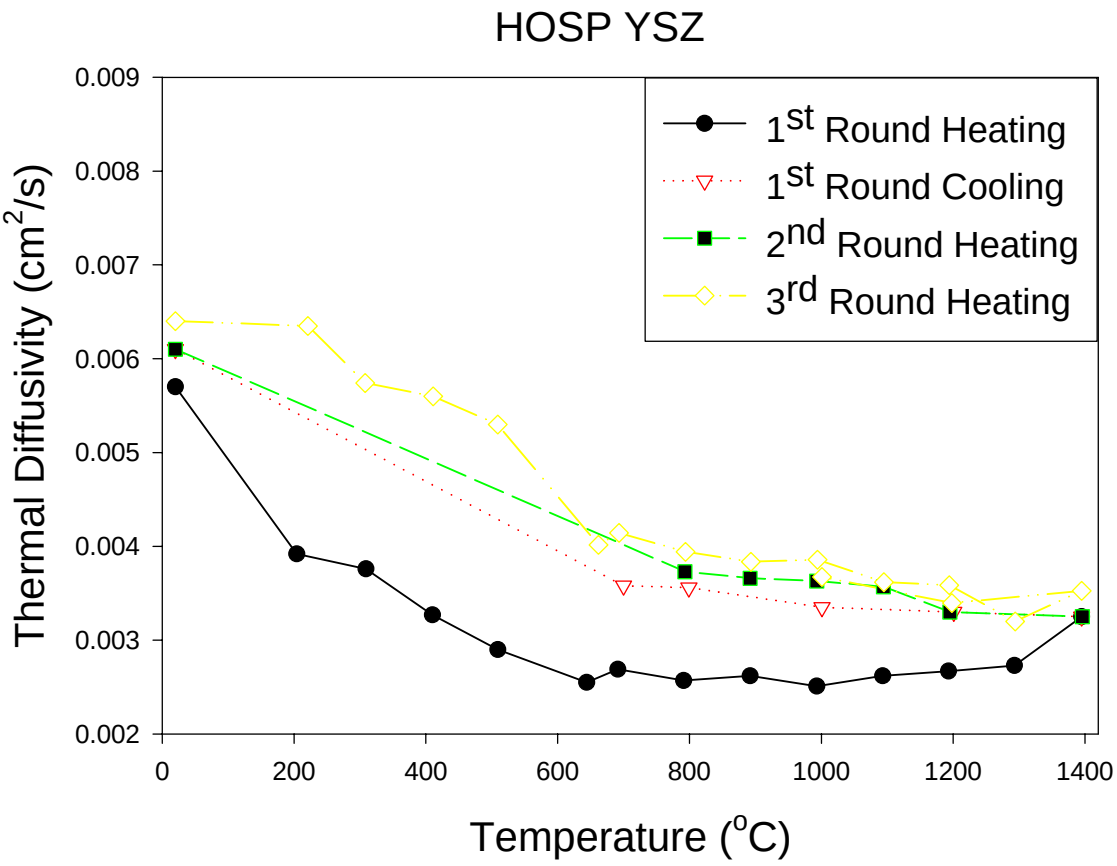

Figure 4-12. As-sprayed HOSP YSZ coating thermal diffusivity.

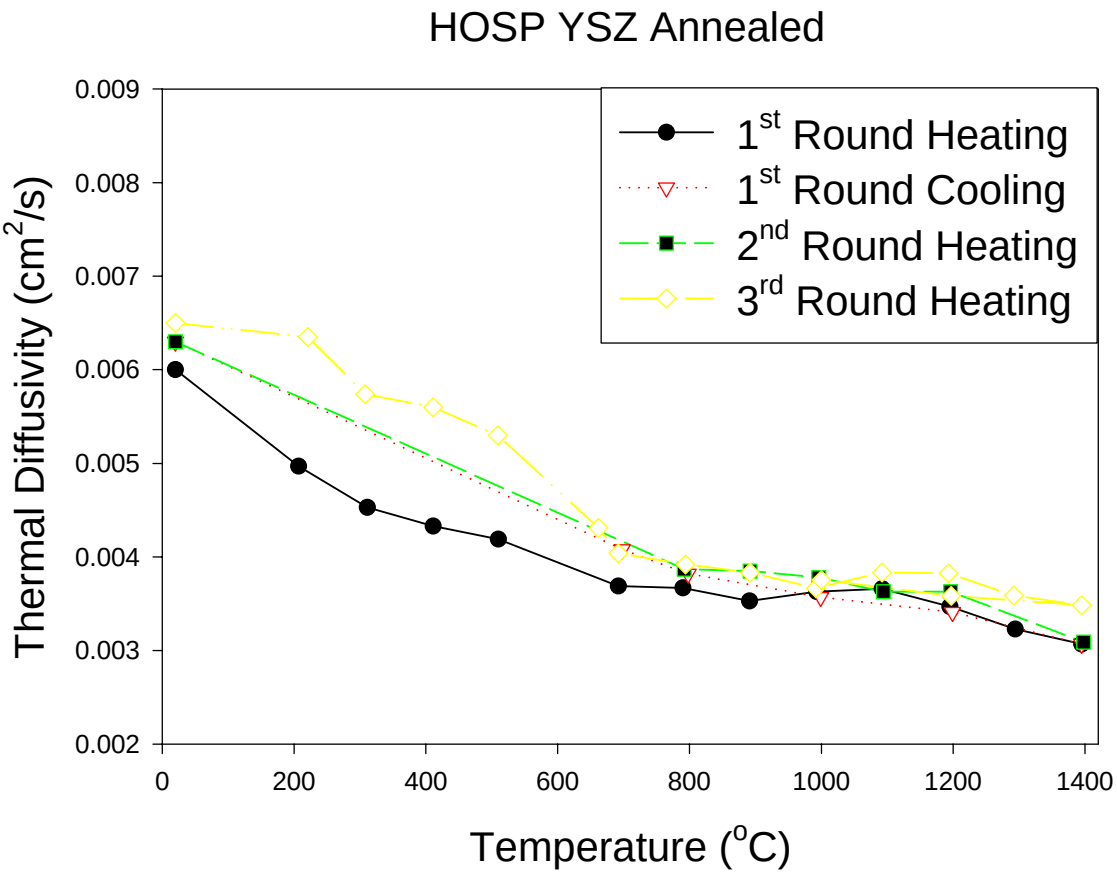

Figure 4-13. Short-term annealed (10 hours at 1200°C) HOSP YSZ coating thermal diffusivity.

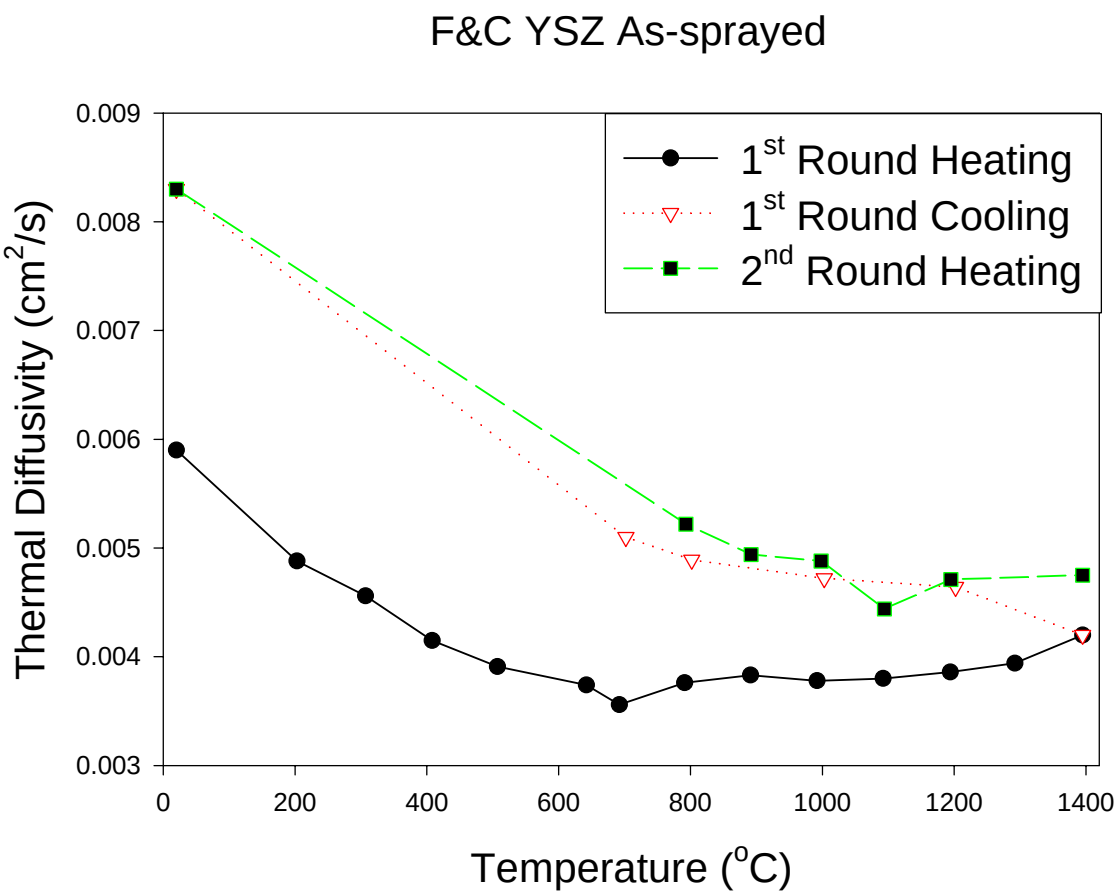

Figure 4-14. As-sprayed F&C YSZ coating thermal diffusivity.

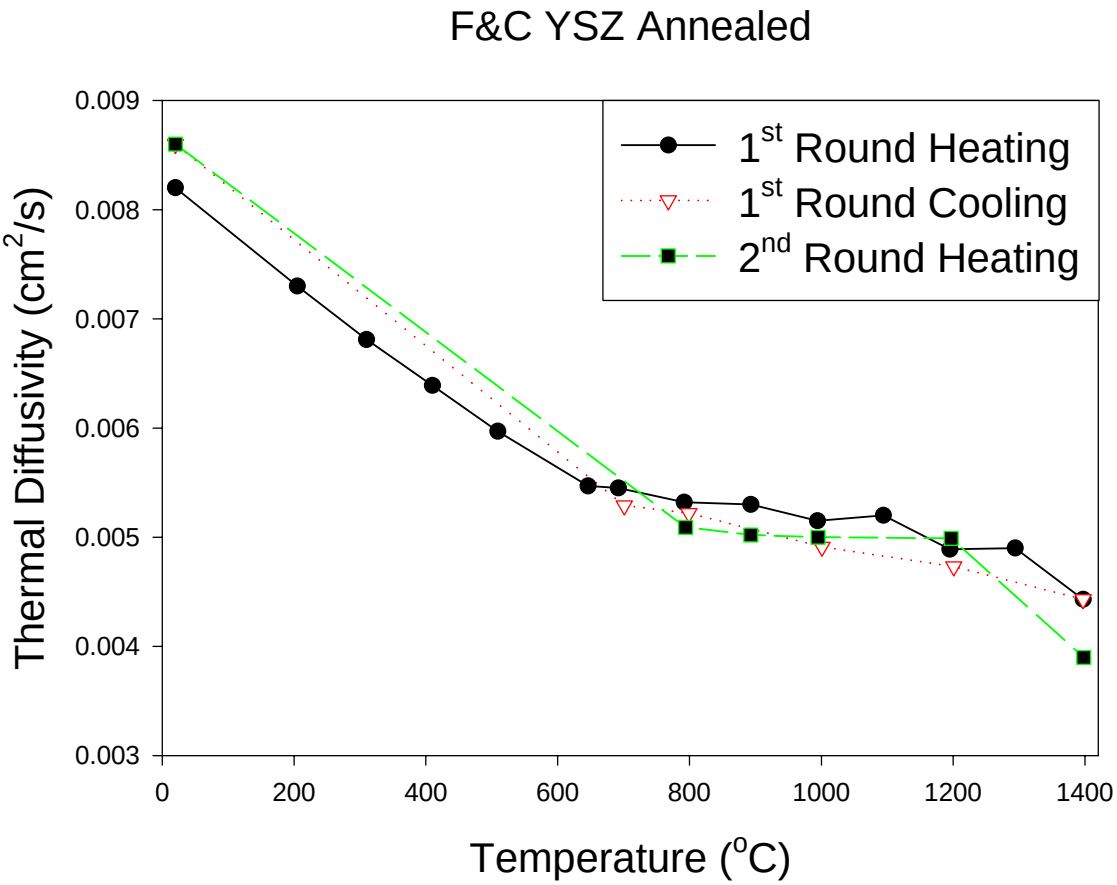

Figure 4-15. Short-term annealed (10 hours at 1200°C) F&C YSZ coating thermal diffusivity

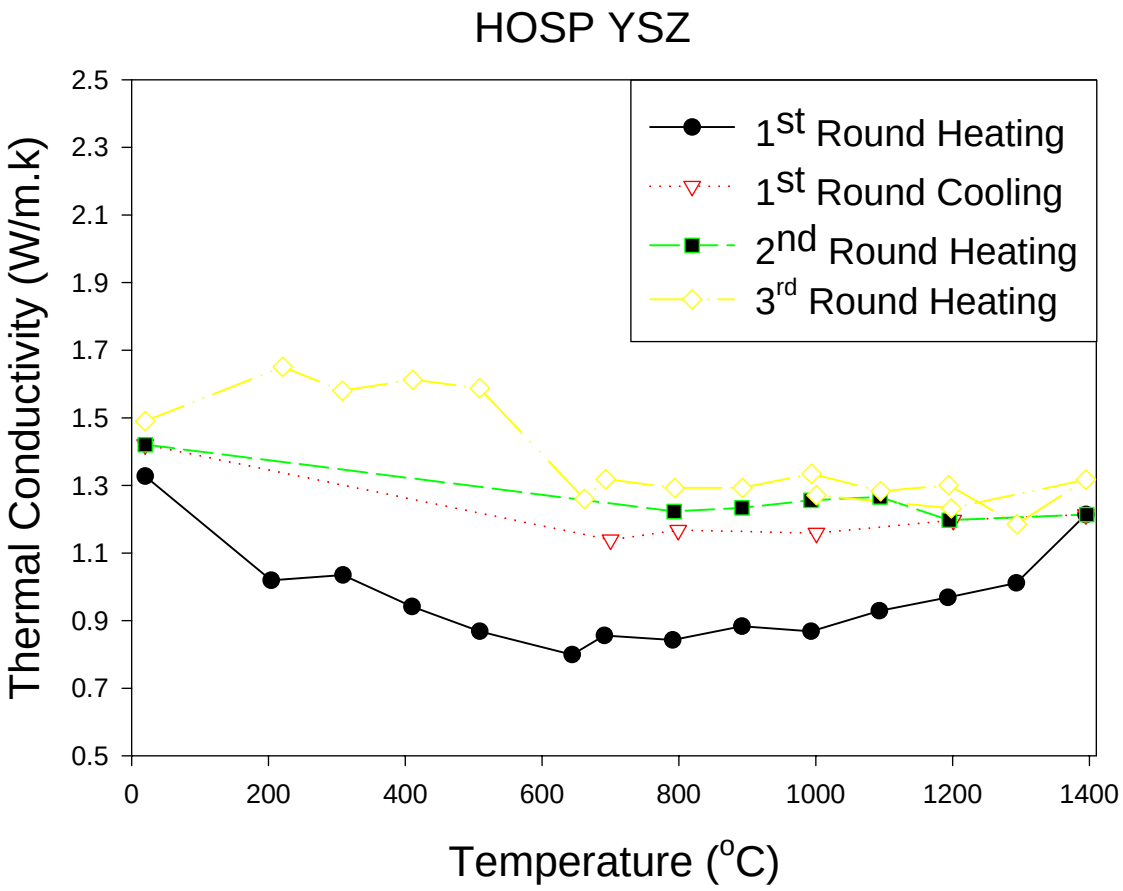

Figure 4-16. As-sprayed HOSP YSZ coating thermal conductivity.

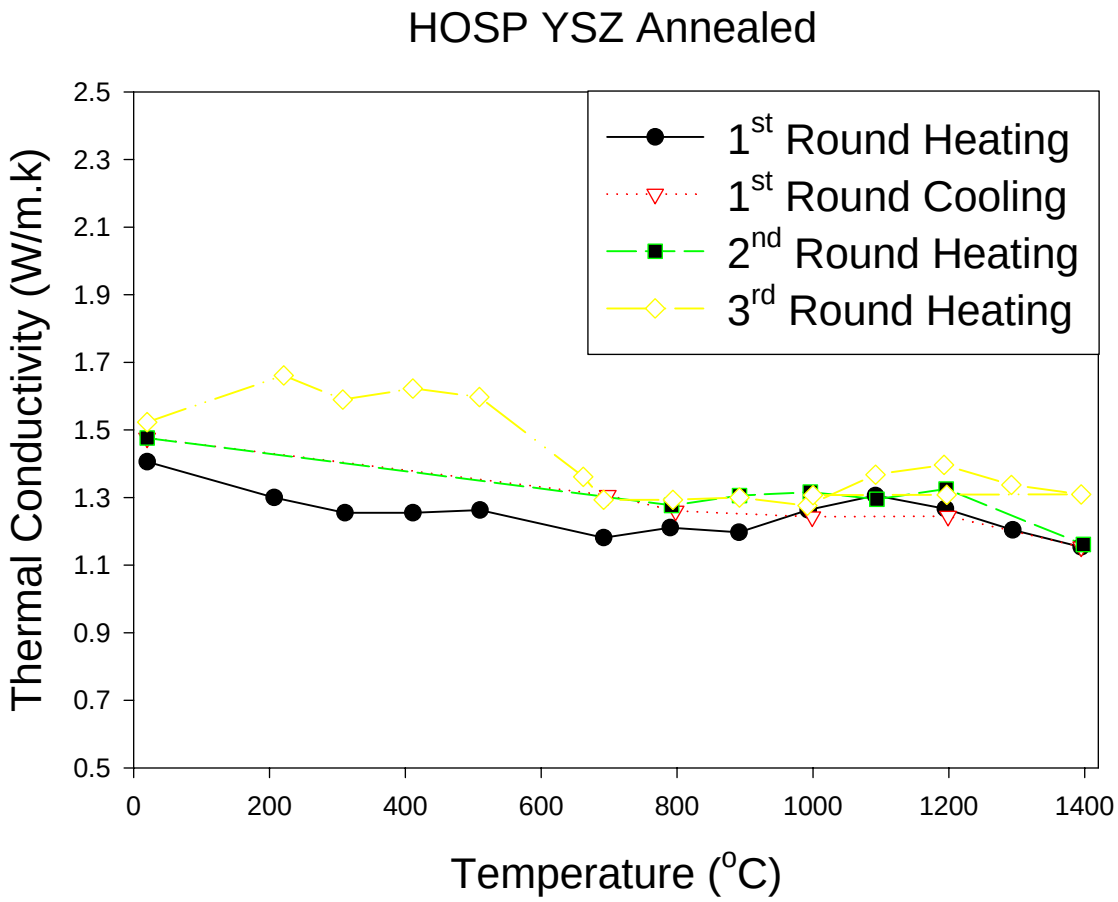

Figure 4-17. Short-term annealed (10 hours at 1200°C) HOSP YSZ coating thermal conductivity.

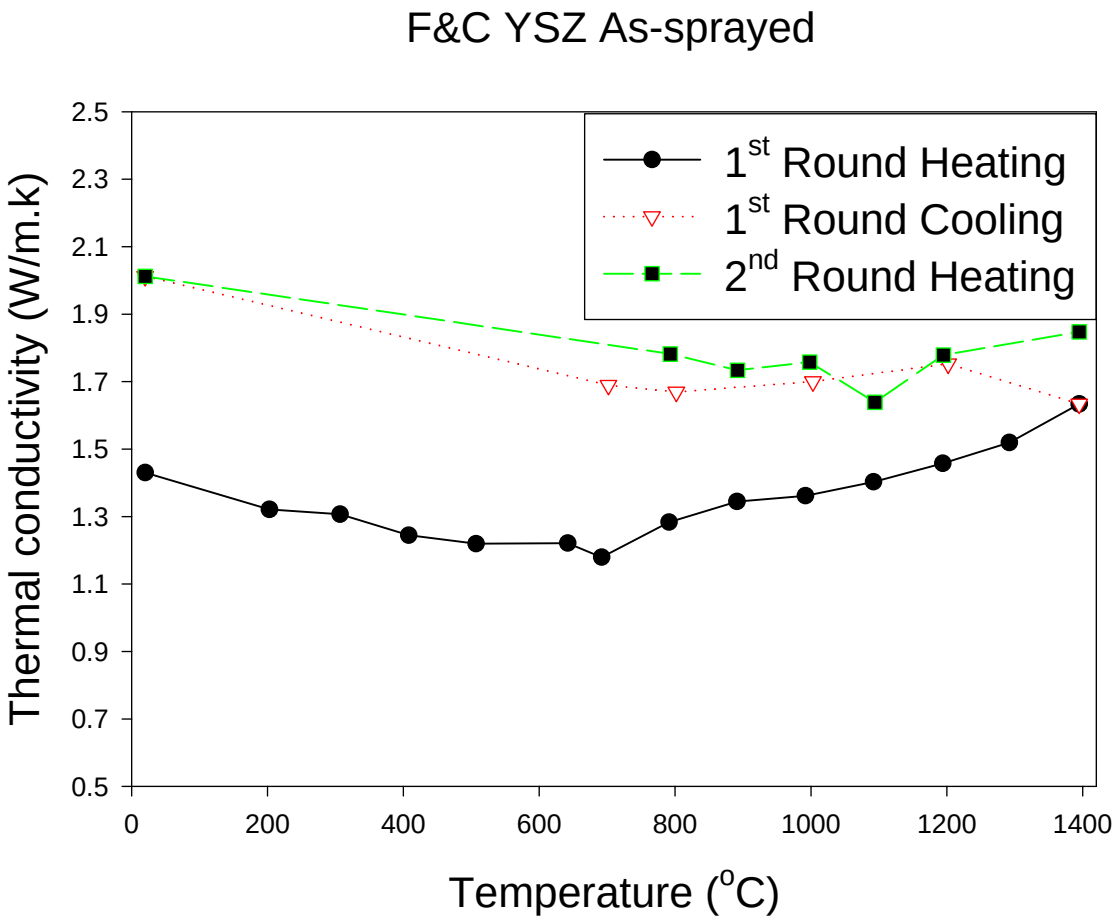

Figure 4-18. As-sprayed F&C YSZ coating thermal conductivity.

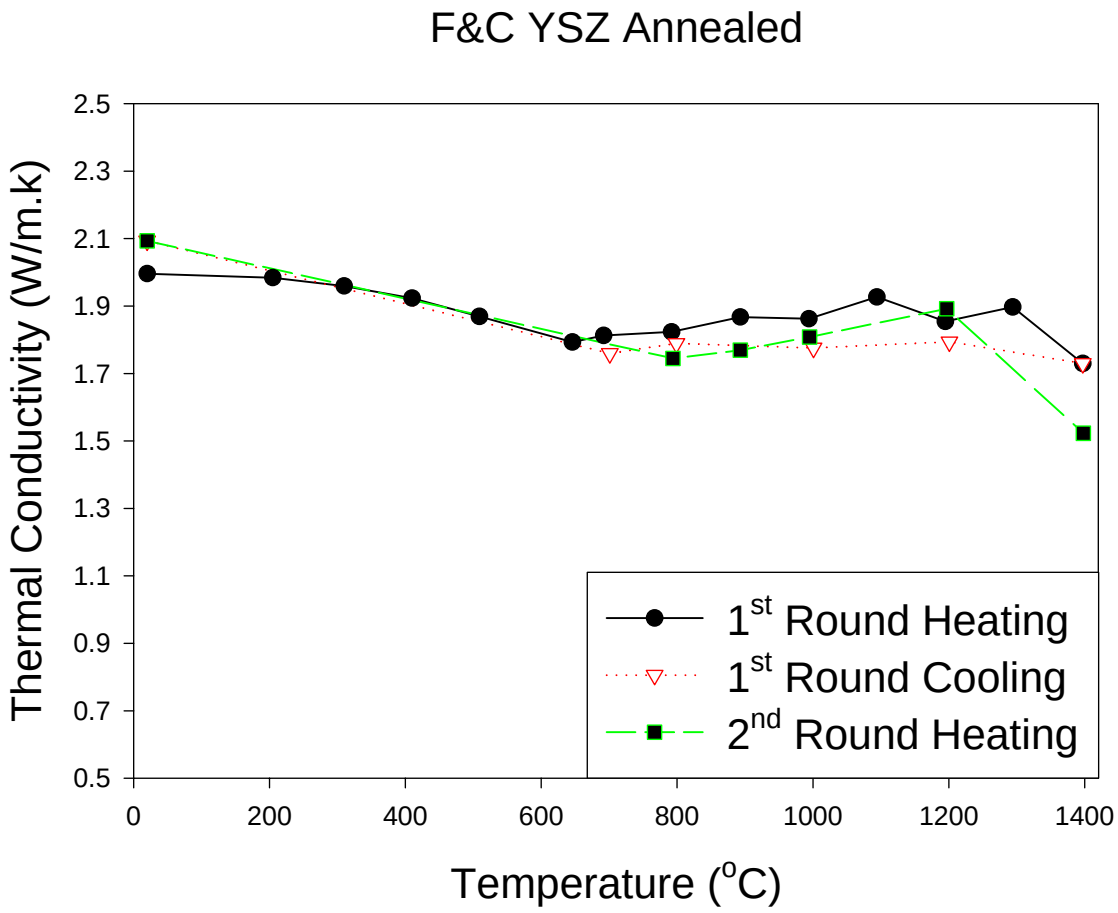

Figure 4-19. Short-term annealed (10 hours at 1200°C) F&C YSZ coating thermal conductivity.

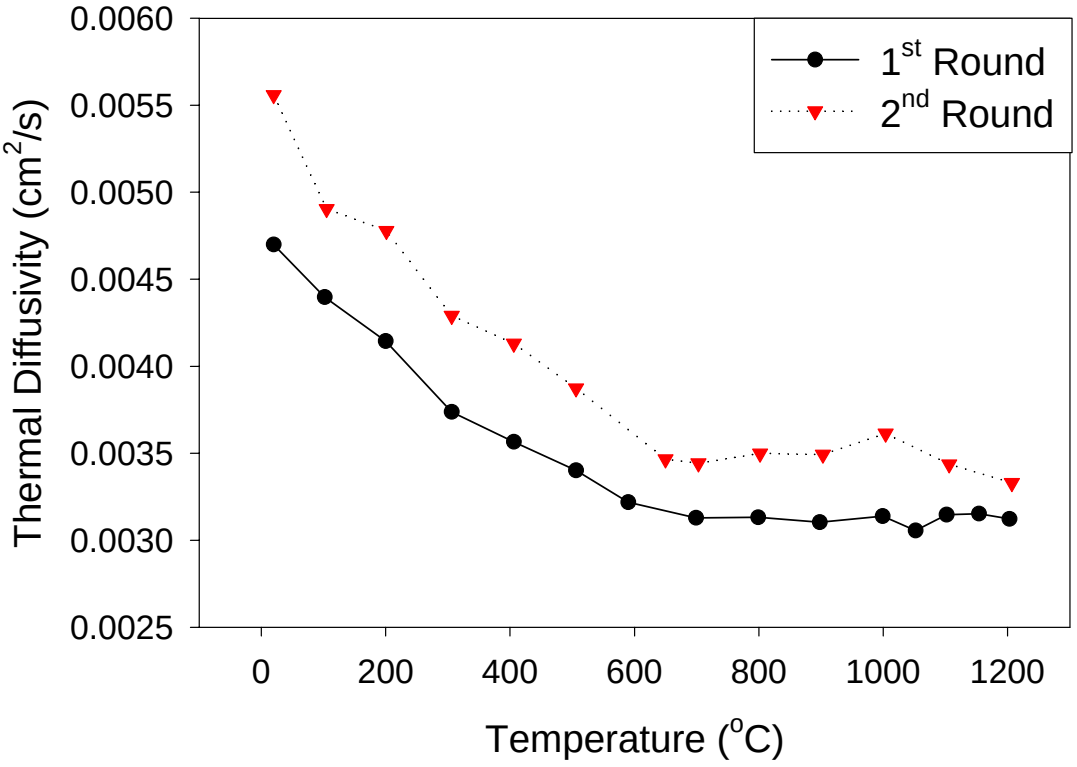

Figure 4-20. As-sprayed F&C YSZ coating thermal diffusivity.

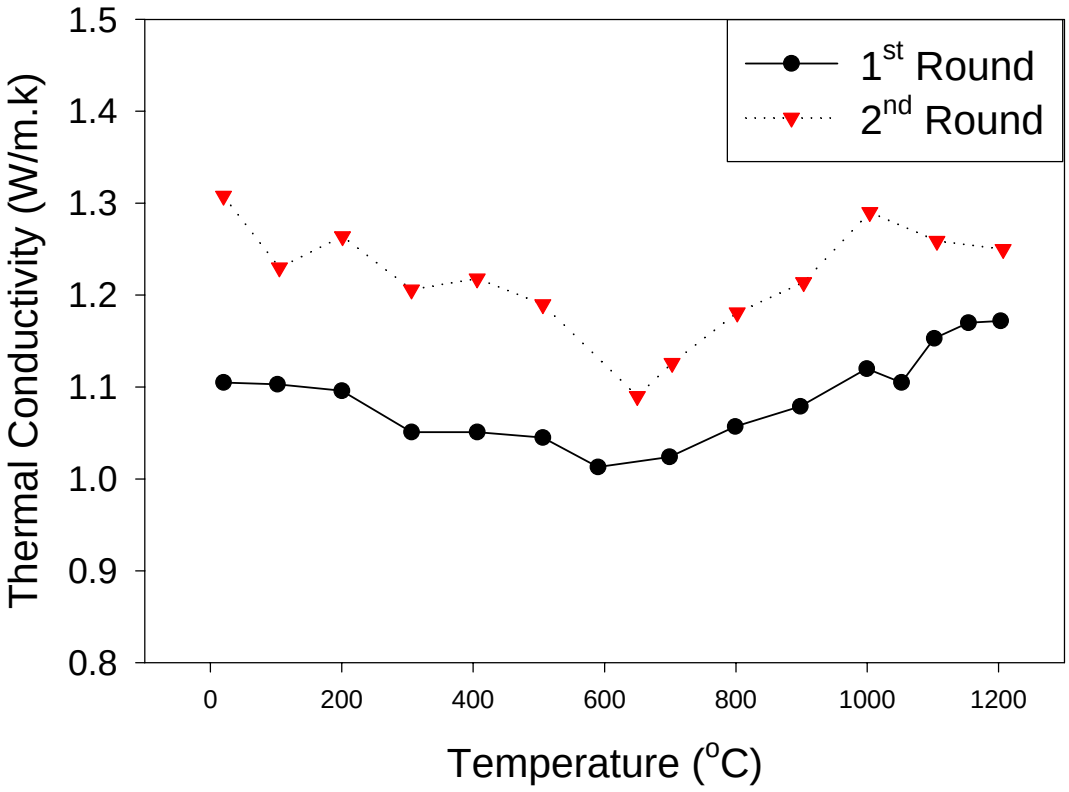

Figure 4-21. As-sprayed F&C YSZ coating thermal conductivity.

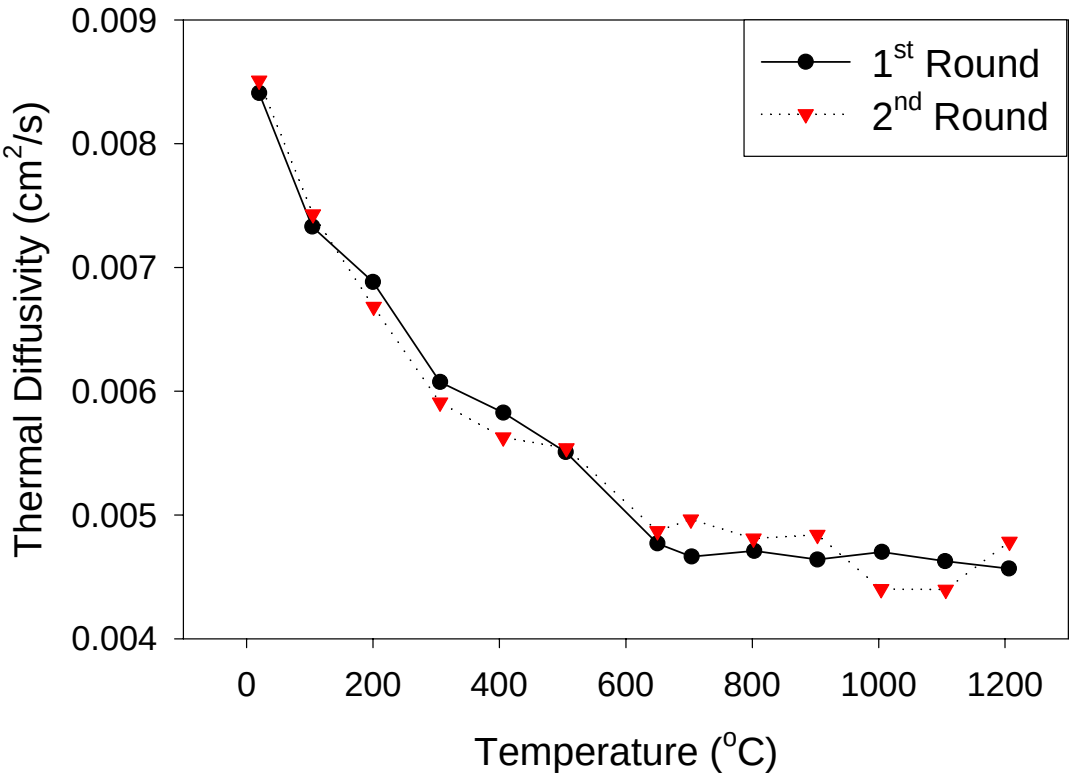

Figure 4-22. Long-term annealed (170 hours at 1200°C) F&C YSZ coating thermal diffusivity.

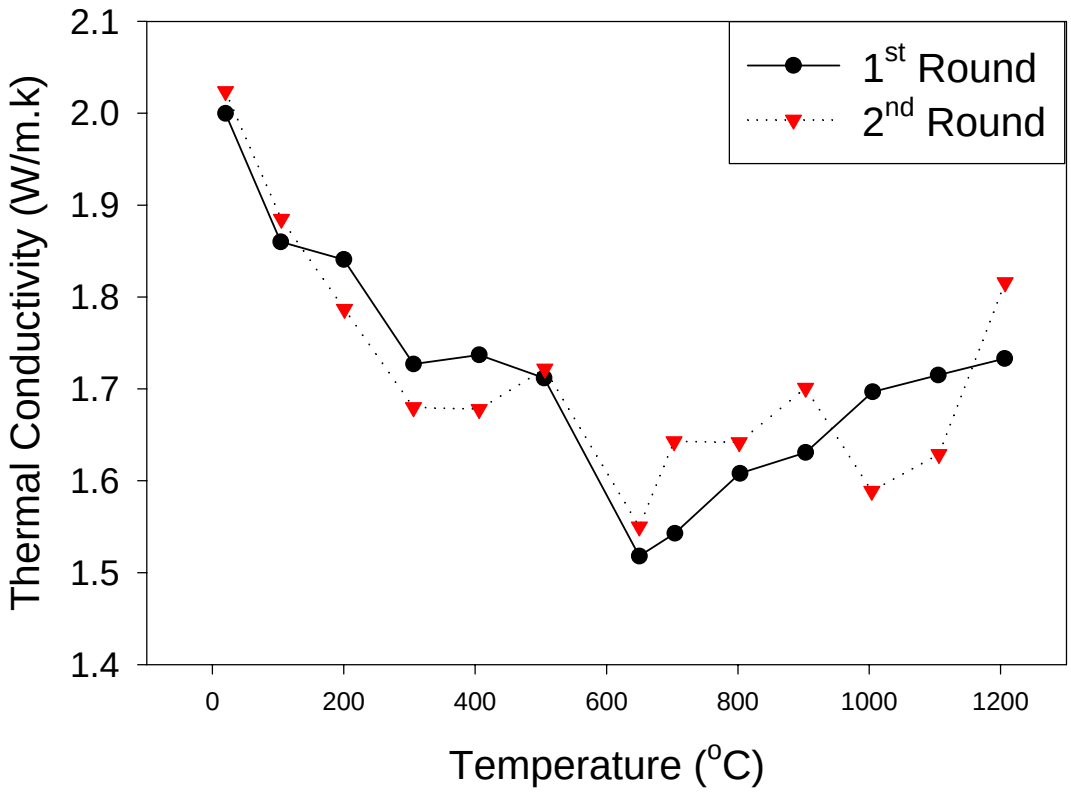

Figure 4-23. Long-term annealed (170 hours at 1200°C) F&C YSZ coating thermal conductivity.

Chapter Five

Thermal Design for Thermal Barrier Coating Systems

In this chapter, recent works are represented on thermal design and microstructure analysis for YSZ thermal barrier coating systems. Figure 5-1 shows the typical heat flux and temperature distribution in a real thermal barrier coating system. The YSZ thermal barrier coating experiences high thermal gradient when the component is in service in a gas turbine engine. To investigate this gradient, YSZ coating are annealed for 225 hours at 1200, 1150, 1100, 1050 ^{o}C, respectively, and the thermal conductivity measurements are performed for the coating before and after annealing. Significant microstructure and thermal property gradient are found. Figure 5-2 shows the microstructure images for F&C YSZ coatings after long-term annealing at different temperatures.

Dongming Zhu et al. used the laser steady-state heat flux technique to investigated the thermal conductivity change kinetics for TBC's. The surface temperatures of the ceramic coatings were maintained at approximately at 990 °C, 1100 °C and 1320 °C, respectively.

The total test time was up to 33 hours for a single test. Tsipas et al. also studied TBC with bond coat and substrate on property change during annealing, such as dimensional change by Dilatometry, phase change by XRD, stress state trough a model.

It has advantage to have bond coats and substrates attached to TBC's. The constrained TBC's may have different sintering behavior than free standings (typically less sintering). However, the temperature drop at the TBC's during his measurements is about 200^{o}C. It is similar to the real case, however, the radiation is too strong, so the measured k is not the intrinsic property for the coating any more. It is called 'steady-state', but not exactly. The conductivity of the TBC is always changing during sintering. It will be very hard to maintain a certain temperature at any surface.

5.1 Effect of Starting Microstructure

Six samples set sprayed with six different control parameters are analyzed. The detail information of the samples is listed in Table 5-1. The as-sprayed coatings are annealed for various time duration at 1200, 1150, 1100, 1050^{o}C, respectively. The normalized thermal conductivity k^* is shown in figure 5-3, figure 5-4, figure 5-5, figure 5-6, figure 5-7 and figure 5-8. The normalized thermal conductivity will be a function of annealing temperature (T) and annealing time (t), and is defined as the following:

$$k^*(T,t) = \frac{k}{k_{as}}$$

where k_{as} is the thermal conductivity of as-sprayed thermal sprayed coatings, and k is the corresponding thermal conductivity for the annealed thermal spray coatings.

Phase change during annealing of plasma-sprayed YSZ has been studied by others. It is believed that the increase in thermal conductivity during annealing below 1200^{o}C is mainly due to topological microstructure change, i.e. the pores and cracks network change, but not the phase change.

5.2 Larson-Miller Parameter

H.E. Eaton et al. used Larson-Miller parameter to equate time, temperature, with change in thermal conductivity for fully stabilized zirconia. Dongming Zhu and Dinwiddie et al. also applied Larson-Miller parameter to TBC thermal conductivity.

Larson-Miller parameter (LMP) was first introduced in 1952 by Larson and Miller to describe the time-temperature relationship for rupture and creep stresses. Larson-Miller parameter is only an empirical fit of the data to time and temperature exposure with no implicit behavioral mechanisms considered.

The Larson-Miller Parameter can be expressed as

$$LMP = T(\ln t + C) \tag{5-1}$$

where T is the annealing temperature and t the annealing time. The value of constant C is 20 in this work. The natural logarithm of the normalized thermal conductivity has a linear relationship with the Larson-Miller parameter (*LMP*):

$$\ln(k^*) = b_0 + b_1 \cdot LMP \tag{5-2}$$

Where b_0 and b_1 are constants. This relationship is drawn in figure 5-9 for all coatings mentioned above. From figure 5-9, it can be seen that the five F&C coatings are close to each other in the $\ln k^* - LMP$ figure, while the HOSP coating is separated from the F&C coatings even the HOSP coating has a similar porosity with the F&C coatings.

5.3 Larson-Miller Parameter at High Temperatures

One sample is selected to perform temperature dependent thermal conductivity measurement for annealing temperatures 1050, 1100, 1150 and 1200^{o}C, respectively. At each temperature, samples at different annealing time is done for the high temperature thermal conductivity tests, and the annealing time levels are 10 hours, 50 hours, 110 hours and 170 hours respectively. The results are shown in figure 5-10. The high temperature Larson-Miller parameter is shown in figure 5-11.

5.4 Concluding Remarks

The the analysis above allows full understanding of the thermal transport property of the thermal barrier coatings at different status with any given history, from which, the overall thermal behavior of the TBC system can be evaluated and predicted. As an

example, with the samples listed above, the coating thermal conductivity at any arbitrary annealing time and annealing temperature can be predicted. Figure 5-12 shows the prediction data for ambient $k*$ annealed at 1100°C for 4000hours, based on the $\ln k^* - LMP$ relationship, for all six coatings. Again, the F&C coatings and the HOSP coating are at different tracks because of their different microstructure features.

Table 5-1. Sample list

No.	Material	Powder	Control Parameter	Run number	Porosity
1	YSZ	F&C	Standard	R349	13.8 %
2	YSZ	F&C	Spray angle	R359	12.9 %
3	YSZ	F&C	Pass rate	R565	12.6 %
4	YSZ	F&C	Spray distance	R358	11.3 %
5	YSZ	F&C	Standard	FC	14.3 %
6	YSZ	HOSP	Standard	HOSP	14.0 %

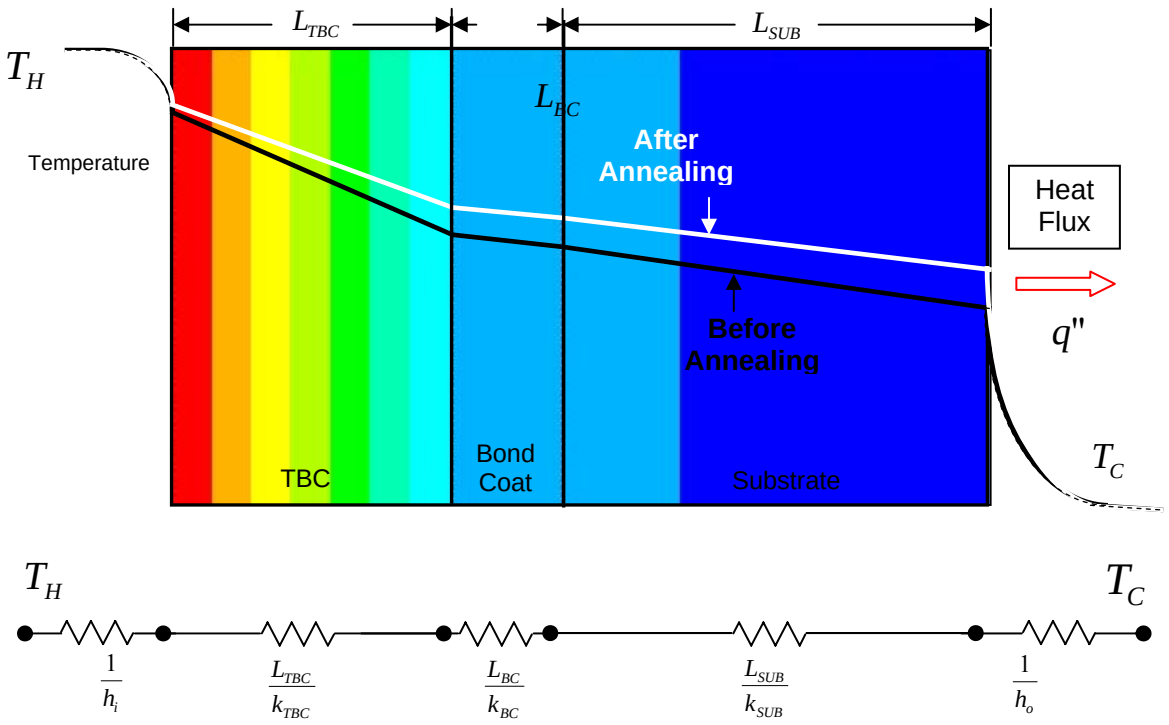

Figure 5-1: Typical heat flux and temperature distribution in a thermal barrier coating system.

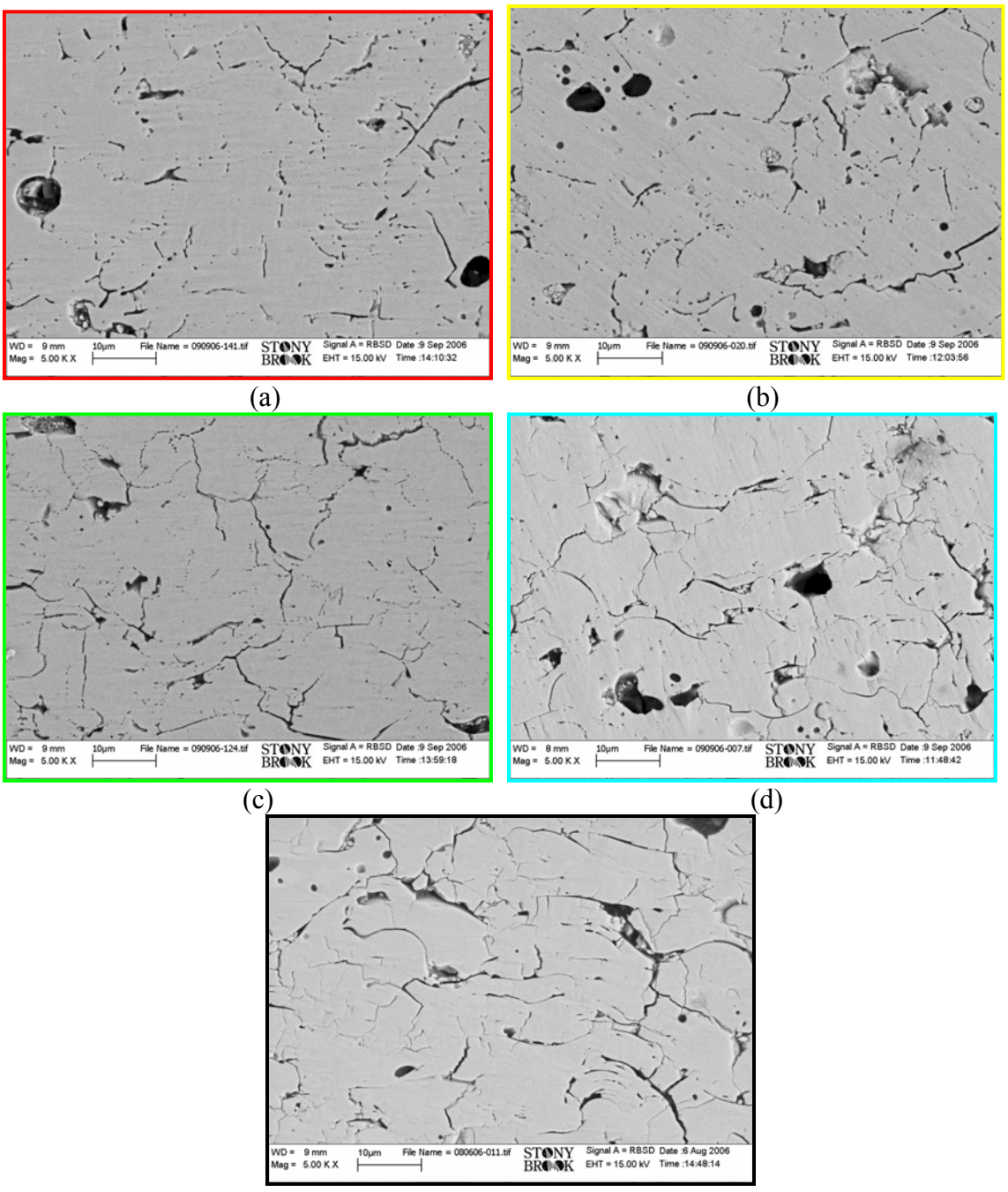

Figure 5-2. Microstructure images for YSZ coatings after different annealing. (a) 1200°C-225 hours, (b) 1250°C-225hours, (c) 1100°C-225hours, (d) 1050°C-225hours, (e) as-sprayed.

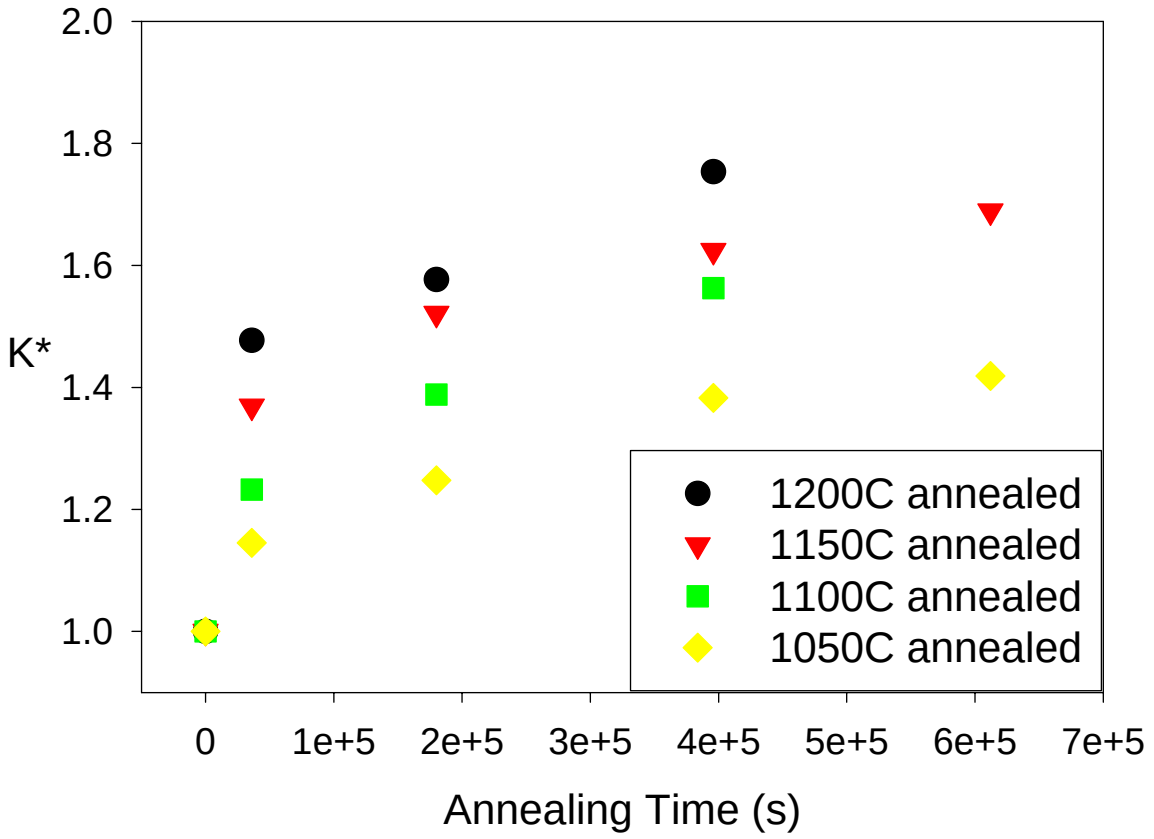

Figure 5-3. Sample No.1. R349: Thermal conductivity increase for F&C YSZ coatings annealed for 225 hours at 1200, 1150, 1100, 1050°C, respectively.

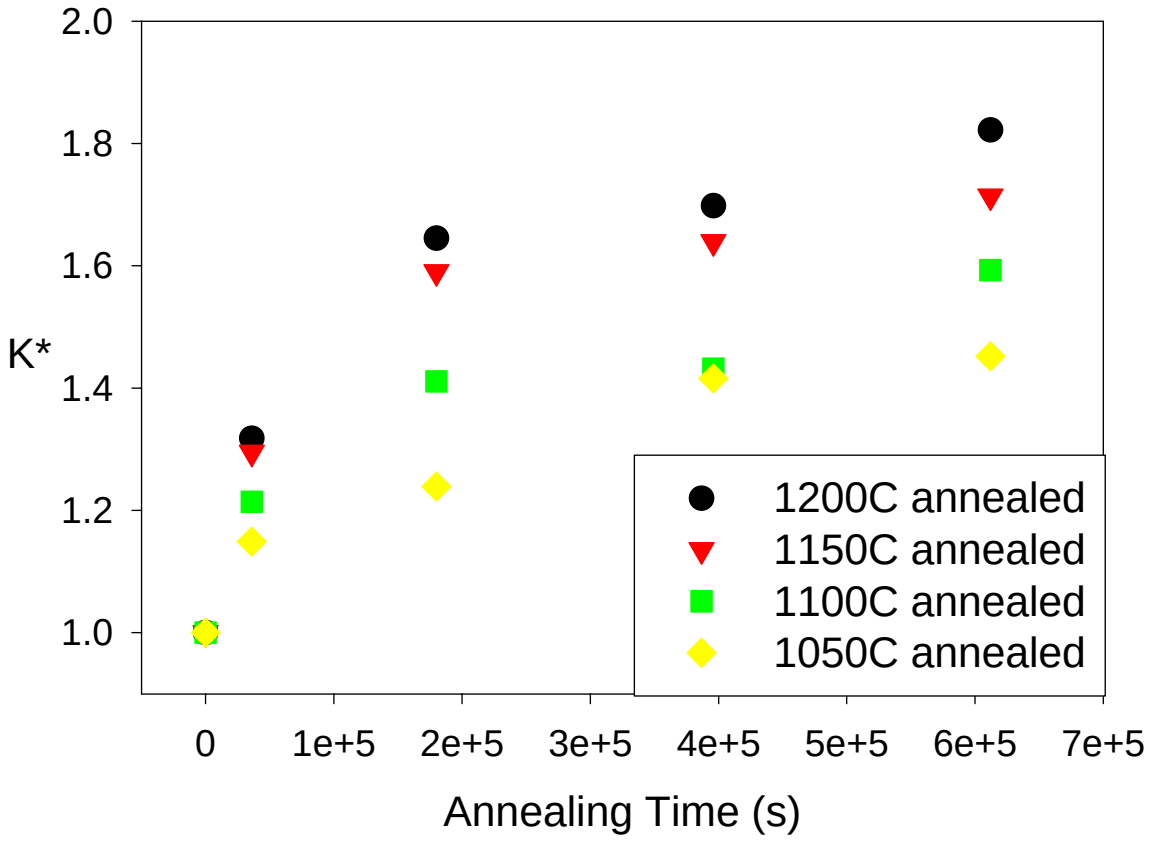

Figure 5-4. Sample No. 2. R359: Thermal conductivity increase for F&C YSZ coatings annealed for 225 hours at 1200, 1150, 1100, 1050°C, respectively.

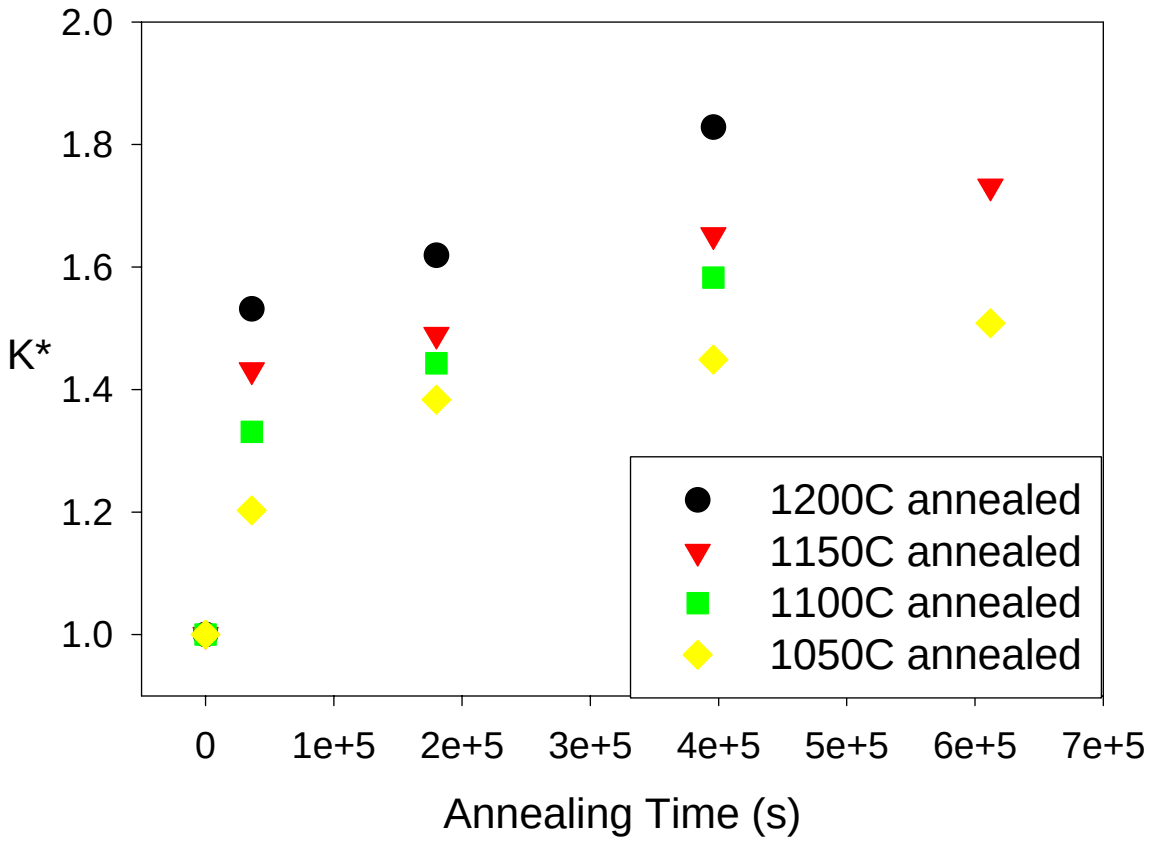

Figure 5-5. Sample No. 3. R565: Thermal conductivity increase for F&C YSZ coatings annealed for 225 hours at 1200, 1150, 1100, 1050°C, respectively.

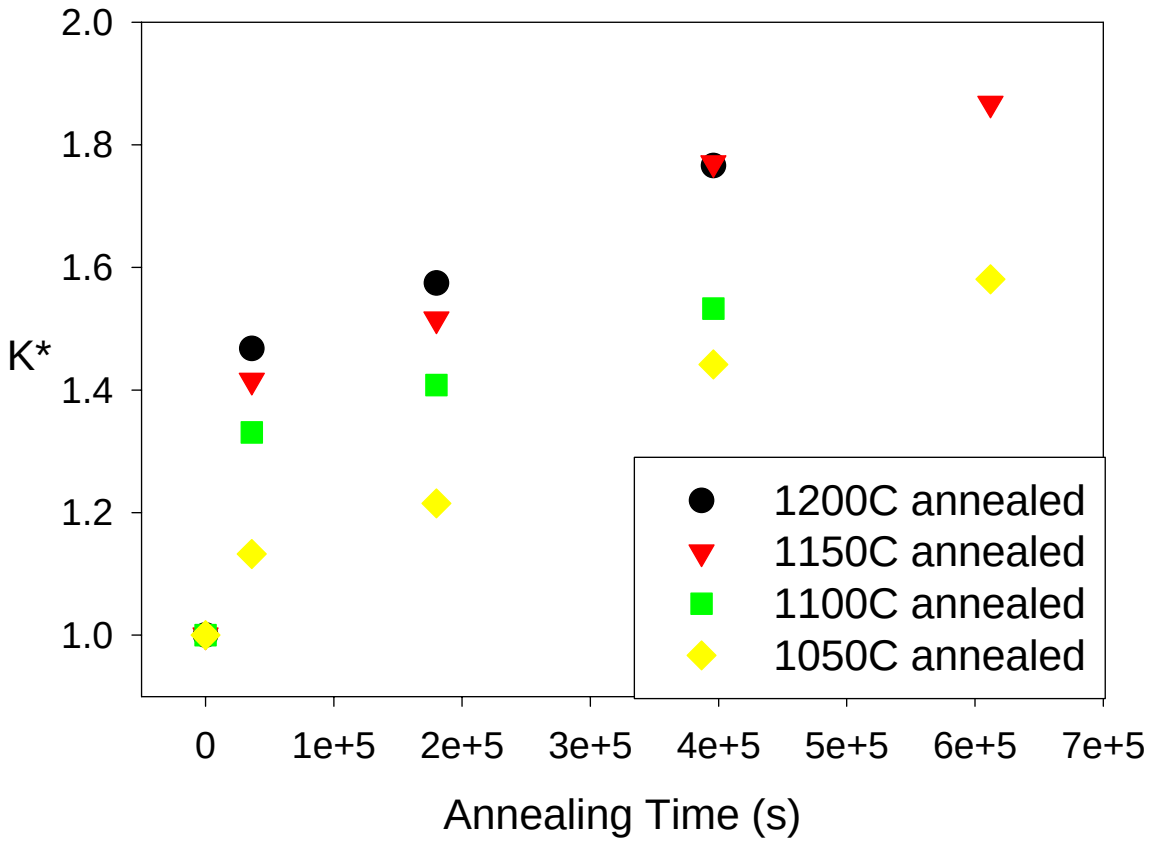

Figure 5-6. Sample No. 4. R358: Thermal conductivity increase for F&C YSZ coatings annealed for 225 hours at 1200, 1150, 1100, 1050°C, respectively.

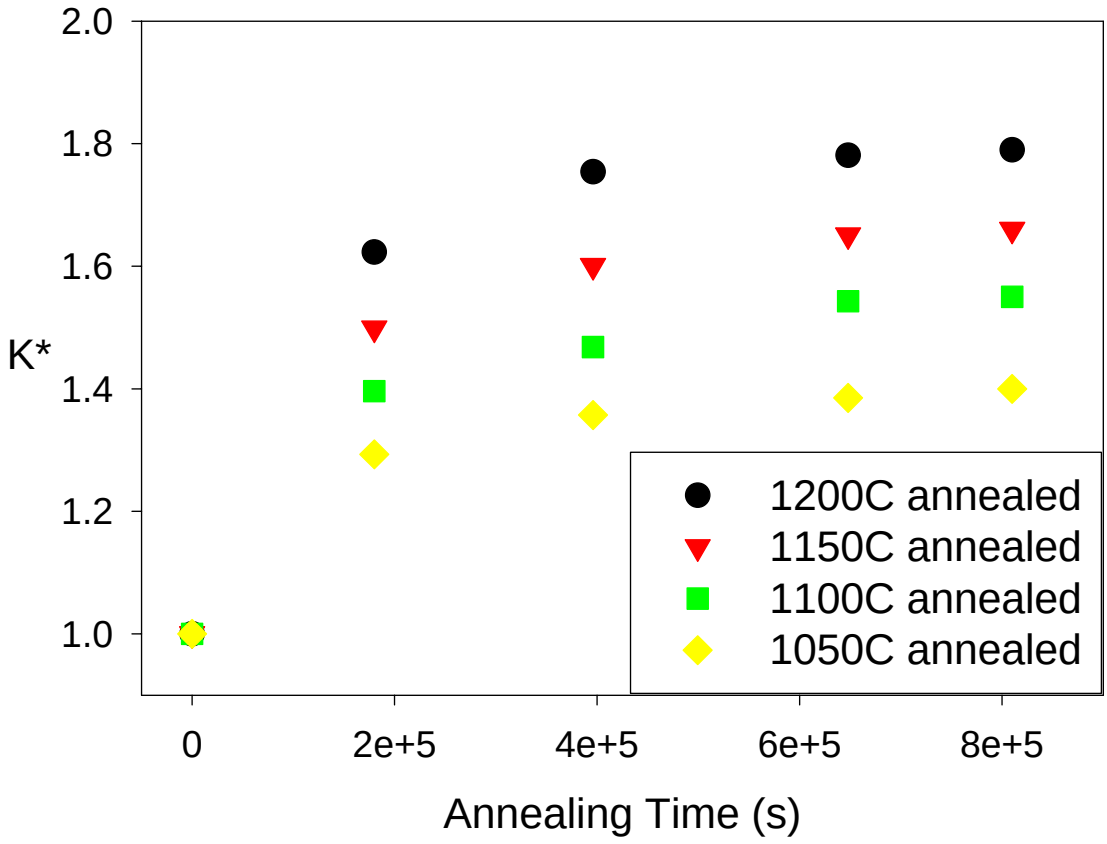

Figure 5-7. Sample No.5. FC: Thermal conductivity increase for F&C YSZ coatings annealed for 225 hours at 1200, 1150, 1100, 1050°C, respectively.

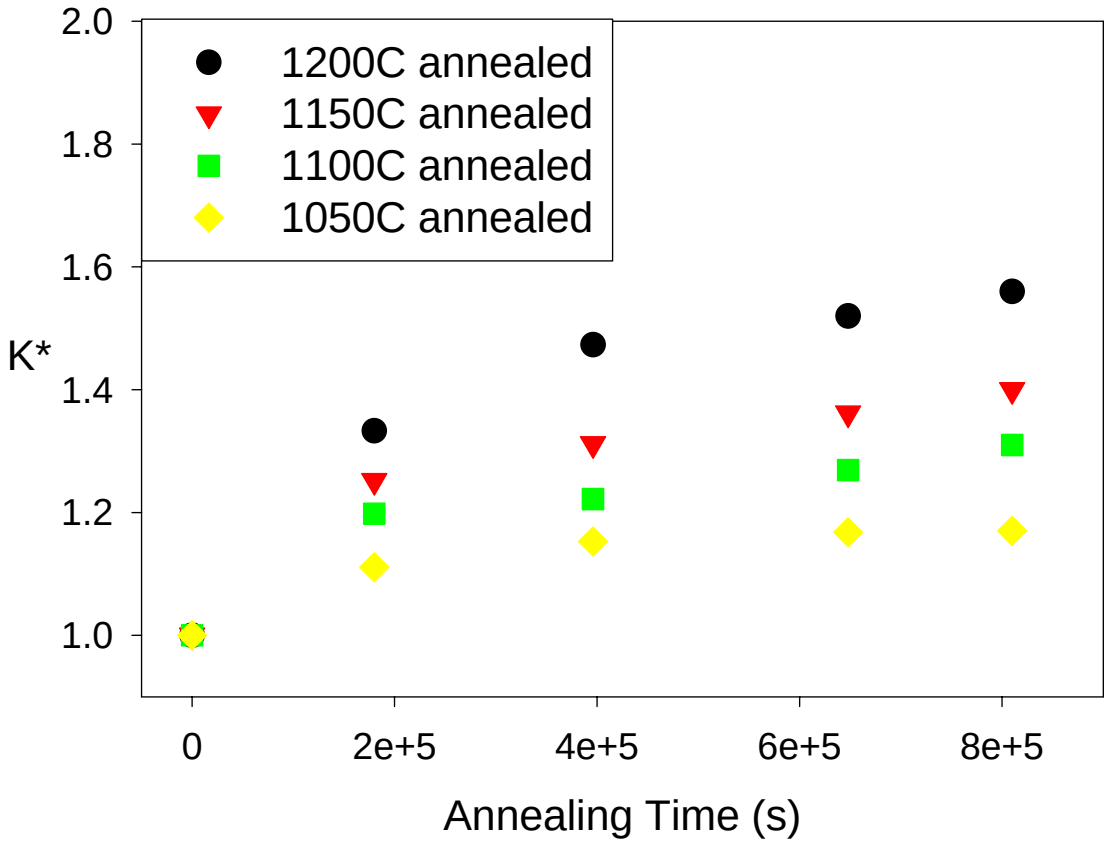

Figure 5-8. Sample No. 6. HOSP: Thermal conductivity increase for F&C YSZ coatings annealed for 225 hours at 1200, 1150, 1100, 1050^{o}C, respectively.

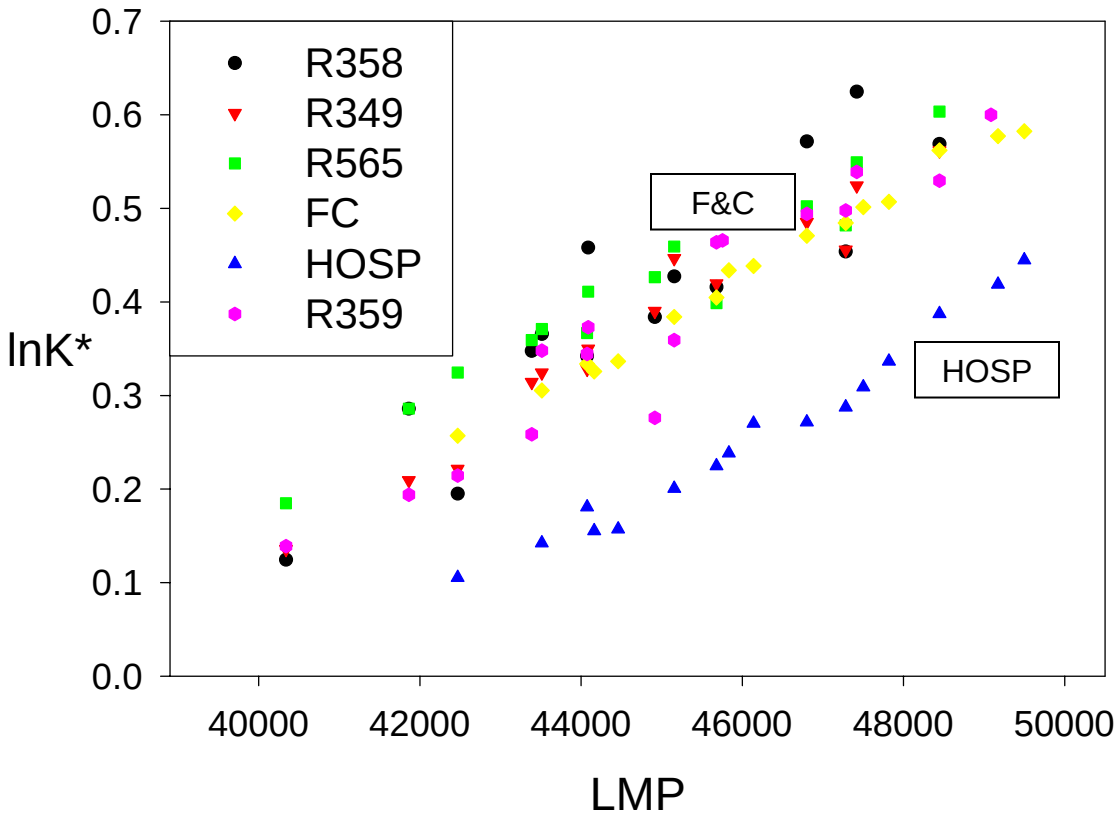

Figure 5-9. Lnk and Larson-Miller relationship for various samples at ambient temperature*

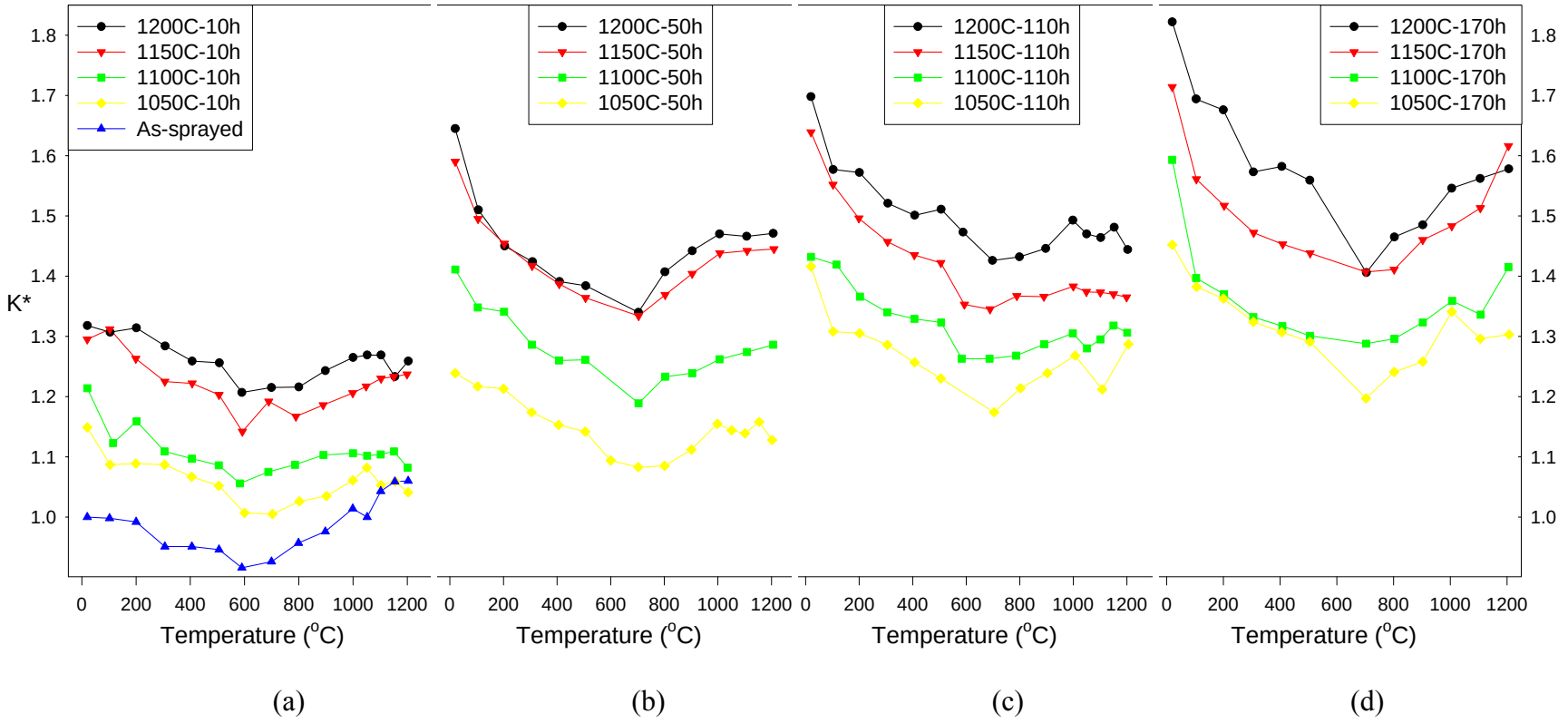

Figure 5-10. Temperature dependent thermal conductivity (normalized) of thermal sprayed YSZ coatings annealed at 1050, 1100, 1150 and 1200°C, respectively. The difference of figure (a), (b), (c) and (d) is the exposure time duration at elevated temperatures: (a) 10 hours, (b) 50 hours, (c) 110 hours, and (d) 170 hours.

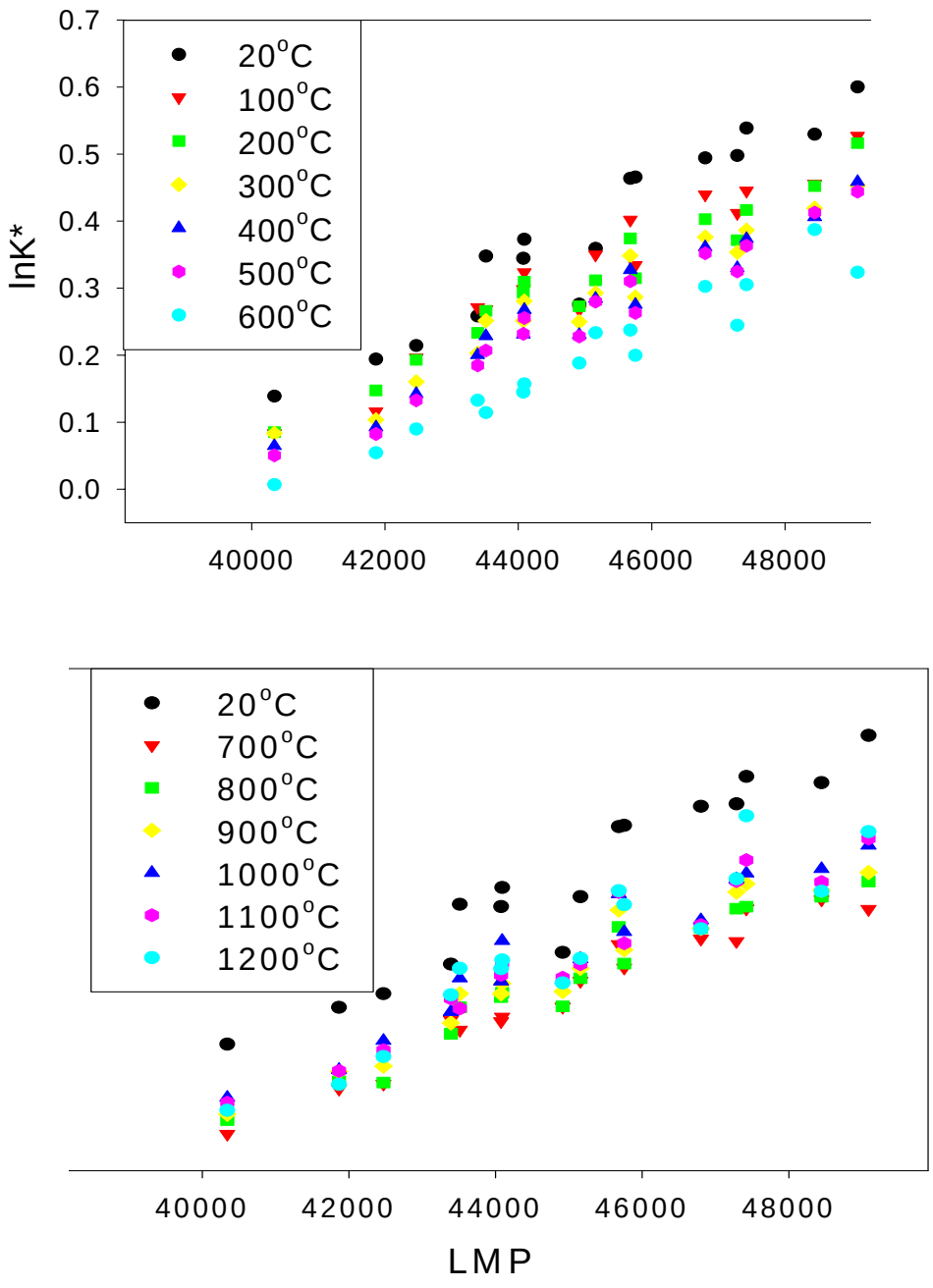

Figure 5-11. Lnk and Larson-Miller relationship for various samples at high temperature*

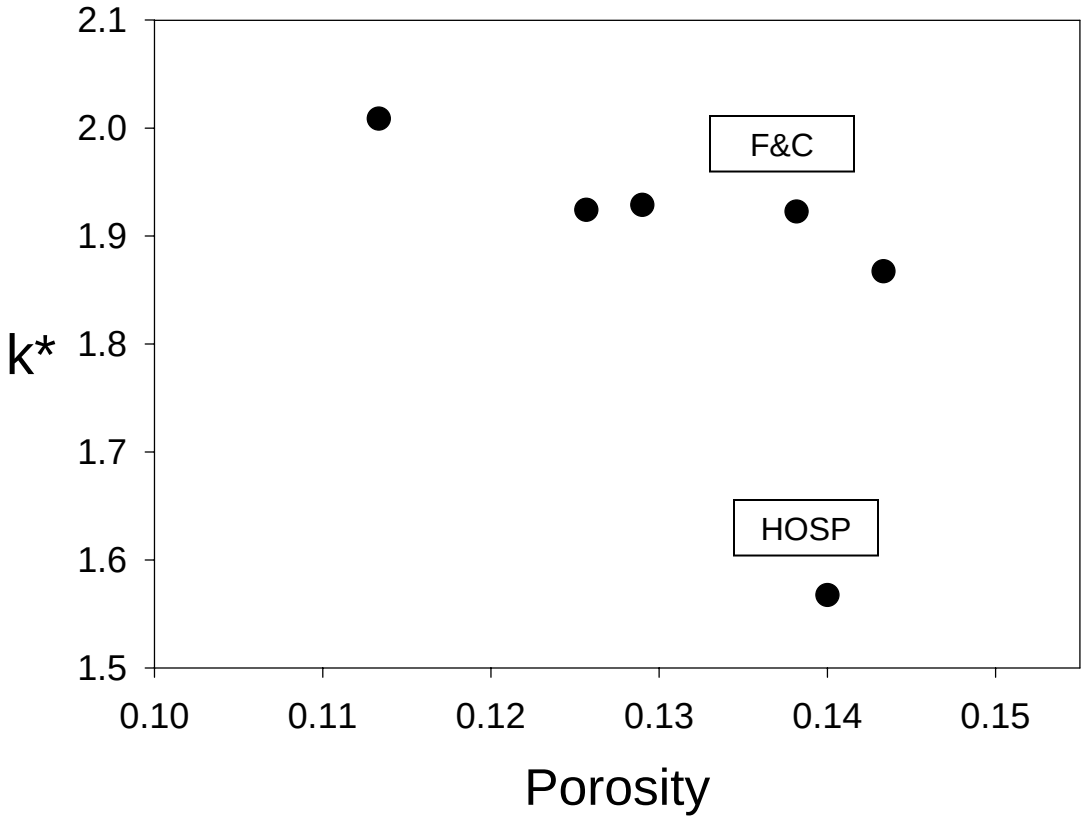

Figure 5-12. *Prediction: k* annealed 4000 hours at 1100^{o}C*

Chapter Six

Conclusions and Future Directions

Thermal design plays critical roles in thermal spray coating systems, and the best way to assess the properties is directly to characterize the coating microstructure. In this dissertation, image analysis is developed to address the detailed microstructure features in a scientific way. Finite element analysis then is built based on the image analysis outcomes, binary images, to simulate the thermal property in both steady-state and transient methods. The steady-state method is from the definition of the effective thermal conductivity, which is the most accurate theoretically; however, it is very hard to practically perform measurements with steady-state method, especially in the thickness range of thermal spray coatings (around 1mm). Transient methods continuously dominate the thermal property measurement techniques. In simulation part, transient method provides vision into the fundamental study of the experimental techniques, but the most convenient way is the steady-state method. In this dissertation, steady-state finite element analysis is widely applied into various thermal spray coating systems, and the results are found to be in good agreement with experimental values, obtained using the flash method.

Moreover, experimental issues are addressed on the measurement of coating thermal properties. The flash method is found to encounter problems for thermal diffusivity determination for heterogeneous materials. Result shows that for highly heterogeneous materials, there are significant errors for standard flash methods on effective thermal conductivity; however, the errors for thermal spray coatings are negligible. This is because the in this complicate microstructure, defects are uniformly distributed into the whole system and decrease the heterogeneity. This work is used to validate and to correct the standard flash method.

Based-on the above techniques developed above, the thermal management and thermal design of TBC systems is address. A variety of anneal coating in various annealing conditions is measured, and the output data is processed by Larson-Miller parameter method. With the high temperature property enhancement, the overall long-term thermal performance can be predicted.

In this dissertation, Chapter one is the overview and introduction to the dissertation. Chapter two, microstructure-based image analysis technique is developed to investigate the microstructure characteristics of general thermal sprayed coatings, such as porosity, pores and cracks orientation and distribution, oxidation, etc. Chapter three, a combined image analysis and finite element analysis modeling approach is developed to assess thermal conductivity from SEM images of the coating microstructure, in both steady-state and transient ways. Chapter four, experimental techniques are introduced for thermal property measurement at ambient and high temperatures. The research work will focus

on the validation and correction of the standard laser flash method. Chapter five, thermal barrier coating systems is analyzed to reveal the dynamic changes in thermal conductivity as a function of annealing time and temperature at both ambient and high temperatures. The overall thermal behavior of the TBC system can be simulated and predicted.

The future work of this study leads to broad directions, including: (1) improvement on the current model with missing mechanisms, (2) Wiedemann-Franz Law in Thermal Spray Coatings, (3) 3-D imaging, (4) Resonant Ultrasound Spectroscopic, etc.

References

Brindley WJ. Properties of plasma-sprayed bond coats. Journal of Thermal Spray Technology 1997;6:85.

Herman H, Sampath S, McCune R. Thermal spray: Current status and future trends. Mrs Bulletin 2000;25:17.

McPherson R. A Model for the Thermal-Conductivity of Plasma-Sprayed Ceramic Coatings. Thin Solid Films 1984;112:89.

Sampath S, Jiang XY, Matejicek J, Leger, A. C., Vardelle, A. Substrate temperature effects on splat formation, microstructure development and properties of plasma sprayed coatings Part I: Case study for partially stabilized zirconia. Materials Science and Engineering a-Structural Materials Properties Microstructure and Processing 1999;272:181.

Cernuschi F, Ahmaniemi S, Vuoristo P, Mantyla, T. Modelling of thermal conductivity of porous materials: application to thick thermal barrier coatings. Journal of the European Ceramic Society 2004;24:2657.

Sevostianov I, Kachanov M. Modeling of the anisotropic elastic properties of plasma-sprayed coatings in relation to their microstructure. Acta Materialia 2000;48:1361.

Wang Z, Kulkarni A, Deshpande S, Nakamura, T., Herman, H. Effects of pores and interfaces on effective properties of plasma sprayed zirconia coatings. Acta Materialia 2003;51:5319.

Deshpande S, Kulkarni A, Sampath S, Herman, H. Application of image analysis for characterization of porosity in thermal spray coatings and correlation with small angle neutron scattering. Surface & Coatings Technology 2004;187:6.

Kulkarni A, Wang Z, Nakamura T, Sampath, S., Goland, A., Herman, H., Allen, J., Ilavsky, J., Long, G., Frahm, J., Steinbrech, R. W. Comprehensive microstructural characterization and predictive property modeling of plasma-sprayed zirconia coatings. Acta Materialia 2003;51:2457.

Lavigne O, Renollet Y, Poulain M, Rio, C., Moretto,P., Brännvall, P., Wigren, J. Microstructural characterisation of plasma sprayed thermal barrier coatings by quantitative image analysis. Quantitative microscopy of high temperature materials conference– Sheffield, UK, 1999.

Poulain M, Dorvaux JM, Lavigne O, Mévrel, R. , Renollet, Y. , Rio, C. Computation of thermal conductivity of porous materials applications to plasma sprayed TBCs. Turbomat 2002 International Symposium on Advanced Thermal Barrier Coatings and Titanium Aluminides for Gas Turbines 2002;June, 17-19 2002, Germany.

Pawlowski L, Fauchais P. Thermal Transport-Properties of Thermally Sprayed Coatings. International Materials Reviews 1992;37:271.

Marple BR, Lima RS. Process Temperature/Velocity-Hardness-Wear relationships for high-velocity oxyfuel sprayed nanostructured and conventional Cermet coatings. Journal of Thermal Spray Technology 2005;14:67.

Taylor RE. Thermal conductivity determinations of thermal barrier coatings. Materials Science and Engineering a-Structural Materials Properties Microstructure and Processing 1998;245:160.

[15] Klemens PG, Gell M. Thermal conductivity of thermal barrier coatings. Materials Science and Engineering a-Structural Materials Properties Microstructure and Processing 1998;245:143.

Raghavan S, Wang H, Dinwiddie RB, Porter, W. D., Mayo, M. J. The effect of grain size, porosity and yttria content on the thermal conductivity of nanocrystalline zirconia. Scripta Materialia 1998;39:1119.

Nicholls JR, Lawson KJ, Johnstone A, Rickerby, D. S. Methods to reduce the thermal conductivity of EB-PVD TBCs. Surface & Coatings Technology 2002;151:383.

Wayne SF, Sampath S, Anand V. Wear Mechanisms in Thermally-Sprayed Mo-Based Coatings. Tribology Transactions 1994;37:636.

Sampath S, Jiang XY, Matejicek J, Prchlik, L., Kulkarni, A., Vaidya, A. Role of thermal spray processing method on the microstructure, residual stress and properties of coatings: an integrated study for Ni-5 wt.%Al bond coats. Materials Science and Engineering a-Structural Materials Properties Microstructure and Processing 2004;364:216.

Friis M. A Methodology to Control the Microstructure of Plasma Sprayed Coatings, Doctoral Thesis.

Maxwell-Garnett. J. Colours in metal glasses and in metallic lms. Phil. Trans. R. Soc. Lond. 203, 385-420 1904.

Lide DR. CRC Handbook of Chemistry and Physics 1913-1995, CRC Press. 75th Edition.

http://rsb.info.nih.gov/nih-image/ NIH Image version 1.62. It was developed at the Research Services Branch (RSB) of the National Institute of Mental Health (NIMH), part of the National Institutes of Health (NIH). NIMH, 6001 Executive Boulevard, Rm. 8184, MSC 9663, Bethesda, MD 20892-9663, USA.

Antou G, Montavon G, Hlawka F, Bolot R, Cornet A, Coddet C, Machi F. Thermal and mechanical properties of partially stabilized zirconia coatings manufactured by hybrid plasma spray process. High Temperature Material Processes 2005;9:109.

Louis P, Gokhale AM. Application of Image-Analysis for Characterization of Spatial Arrangements of Features in Microstructure. Metallurgical and Materials Transactions a-Physical Metallurgy and Materials Science 1995;26:1449.

Singh H, Gokhale AM. Visualization of three-dimensional microstructures. Materials Characterization 2005;54:21.

Friis M, Persson C, Wigren J. Influence of particle in-flight characteristics on the microstructure of atmospheric plasma sprayed yttria stabilized ZrO2. Surface & Coatings Technology 2001;141:115.

1461-01 AE. Standard Test Method for Thermal Diffusivity of Solids by the Flash Method, ASTM International.

ASTM. E 1461-01 Standard Test Method for Thermal Diffusivity of Solids by the Flash Method, ASTM International.

Chi W, Sampath S, Wang H. Ambient and High Temperature Thermal Conductivity of Thermal Sprayed Coatings. Proceedings of the 2006 Thermal Spray Conference, May 15-18, 2006, Seattle, Washington, USA 2006.

D. M. Zhu and R. A. Miller, Thermal conductivity and elastic modulus evolution of thermal barrier coatings under high heat flux conditions, Journal of Thermal Spray Technology 9 (2000), no. 2, 175-180.

J. Ilavsky and J. K. Stalick, Phase composition and its changes during annealing of plasma-sprayed ysz, Surface & Coatings Technology 127 (2000), no. 2-3, 120-129.

D. M. Zhu, R. A. Miller, B. A. Nagaraj and R. W. Bruce, Thermal conductivity of eb-pvd thermal barrier coatings evaluated by a steady-state laser heat flow technique, Surface & Coatings Technology 138 (2001), no. 1, 1-8.

S. A. Tsipas, I. O. Golosnoy, R. Damani and T. W. Clyne, The effect of a high thermal gradient on sintering and stiffening in the top coat of a thermal barrier coating system, Journal of Thermal Spray Technology 13 (2004), no. 3, 370-376.

R. W. Trice, Y. J. Su, J. R. Mawdsley, K. T. Faber, A. R. De Arellano-Lopez, H. Wang and W. D. Porter, Effect of heat treatment on phase stability, microstructure, and thermal conductivity of plasma-sprayed ysz, Journal of Materials Science 37 (2002), no. 11, 2359-2365.

H. E. Eaton, J. R. Linsey and R. B. Dinwiddie, The effect of thermal aging on the thermal conductivity of plasma sprayed fully stabilized zirconia, Thermal Conductivity 22, ed. T Tong, Technomic Pub. (1994), 289-300.

F. R. Larson and J. Miller, A time-temperature relationship for rupture and creep stresses, Transactions of the ASME Jul (1952), 765-775.

H. Wang, D. R. B. and P. A. Gaal, Multiple station thermal diffusivity instrument, Thermal Conductivity 23, Eds. K.E. Wilkes, R. B. Dinwiddie and R. S. Graves (1996), 119-127.